学位論文

Disk-type resonant antenna with a laser transducer for monitoring gravitational waves

重力波モニター用レーザートランスデューサー装備ディスクタイプ共振型アンテナ

平成 8年12月

博士（理学）申請

東京大学大学院理学系研究科

物理学専攻

近藤　尚人

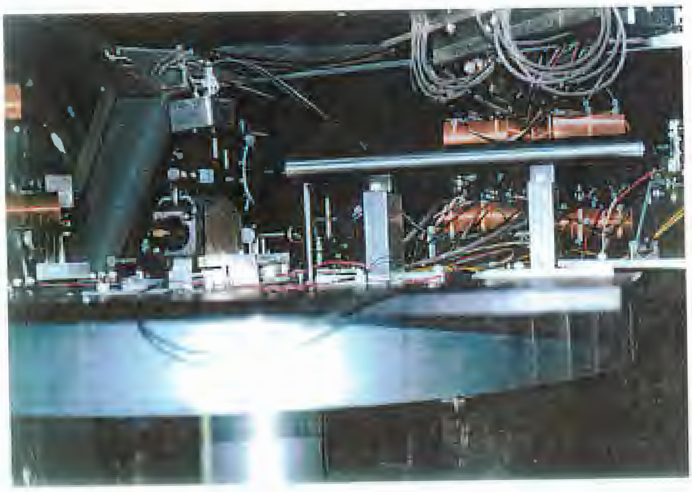

Frequency Stabilization Cavity

Laser Transducer

Disk Antenna

Isolation Stacks

Contents

Chapter 1

Introduction

The detection of gravitational waves, which is also one of the remained subjects of Einstein's theory of general relativity which must be verified [1, 2, 3, 4, 5], is one of exciting fields in physics. Gravitational waves have never been detected directly. However the analysis of experimental data obtained from the observations of binary systems, in particular binary pulsars such as PSR 1913+16 discovered by R.A. Hulse and J.H. Taylor [7], gives a strong evidence that these systems loose energy through gravitational radiation (J.H. Taylor and J.M. Weisberg [6]). A direct observation of gravitational waves will bring us various astronomical and astrophysical information about sources of gravitational waves; supernovas, coalescing compact binary systems, pulsars and the stochastic background of gravitational waves, which are not observable with electromagnetic radiatoin, and also open a new window to understand the universe through gravity.

In general relativity gravitational waves cause a quadrupole strain, "h", in spacetime. Gravitational wave detectors have been designed to utilize this characteristic of gravitational waves. The main techniques in order to search gravitational waves, which have been developed until now and will be used in the future, are resonant mass detectors and laser interferometers.

The laser interferometer has a wide frequency range from tens of Hz to 1 kHz. Several large-scale interferometer projects have been started throughout the world in the hope of establishing "gravitational astronomy" based on the international network of broad-band gravitational wave detectors in the 21th century [8, 9, 10, 11].

On the other hand, the resonant mass detector, whose development is the theme of this thesis, is smaller and simpler than large-scale laser interferometers. Since J. Weber [12] began in 1960s, many institutes have promoted the development of resonant mass detectors and are observing gravitational waves.

The resonant mass detector consists of an resonant mass antenna and a transducer. The antenna is a simple object and consists of an elastic body. During the passage of gravitational waves the antenna resonance gets excited. The resonant mass antenna changes the tidal force of gravitational waves into its mechanical vibration.

The transducer is a device which picks up the antenna's vibrational motions and amplifies them as electric signals. It is required to detect an extremely small change of ampitudes of the antenna's vibrational motions caused by passing gravitational waves. The development of transducers is therefore a very important task of resonant gravitational wave detector groups.

Since the strain amplitude of gravitational waves is very small, gravitational wave detectors require special arrangements. The noise of gravitational wave detectors crucially determines the detection performance. In case of resonant mass detectors the fundamental noise can be classified into two categories, the thermal noise of the antenna and the noise of the transducer which induces a back action to the antenna. J. Weber [12] achieved the strain sensitivity $h \sim 10^{-15}$. His detector consisted of a cylindrical antenna, called a "Weber bar " or a "bar antenna" ever since, and a piezo-electric transducer.

Various types of transducers have been considered ever since: many resonant mass detectors have been developed and are operating now; EXPLORER of the Rome group [13], NAUTILUS at the Frascati INFN Laboratories [14] and AURIGA at the INFN Legnaro Laboratories [15] use a capacitive transducer. ALLEGRO of Louisiana State University(LSU) [16] and the detector of Stanford University [17] employ an inductive transducer, and the detector of University of Western Australia(UWA) [18] is with a RF cavity. These detectors are cooled down to liquid helium temperature to decrease the thermal noise of the antenna and work as cryogenic detecdtors. NAUTILUS and AURIGA are operating at temperature below 100 mK, and attain the sensitivity to the order of 10^{-19} in terms of the strain sensitivity of gravitational waves.

The present sensitivities of resonant mass detectors are limited by noise from the transducer to monitor the vibrational motion of an atenna. In order to overcome this difficulty and realize the low noise transducer, several types of highly sensitive transducers have been developed and used in cryogenic detectors. Most typical ones developed so far are of the multi-mode type, which have two-resonant masses and modes incorporated with low temperature devices such as a SQUID or a superconducting microwave cavity, in order to gain a large displacement amplitude and a wide sensitive bandwidth (see, *e.g.*, Ref. [19]). Although the resonant bandwidth of the antenna itself is very narrow, the bandwidth with a flat and high signal-to-noise ratio can be made wide if the displacement noise and back action force on the antenna of the transducer are made sufficiently small.

In order to pursue the new possibility of the resonant mass detector, an optical transducer, *i.e.*, a laser transducer, which applies the laser interferometer technique to the trasducer, is proposed by J.P. Richard of Maryland University [20]. Since a simple Fabry-Perot optical resonator, *i.e.*, a Fabry-Perot cavity, with a high finesse gives the small change of its bsae-line with a high gain, the Fabry-Perot cavity attached to the resonant mass antenna works as a transducer. Moreover, since the noise of the Fabry-Perot cavity can be reduced in principle to the shot noise level and the laser light as a pumping source can decrease a back action to the antenna smaller than other types of transducer, the laser transducer has a potential realizing a sensitive wideband transducer. It is also a simpler read-out instrument than multi-mode resonant transducers.

Richard's group is developing a resonant transducer equipped with an optical resonator consisted of Fabry-Perot cavity and a low power laser for the purpose of installing in a cryogenic bar antenna, and reported the investigation of the high finnese cavity at low temperature and noise measurements, a back action and an electric noise [21, 22] and test the performance of the resonant transducer at room temperature [23]. Its displacement sensitivity was 1.0×10^{-15} m/$\sqrt{\text{Hz}}$.

In this thesis I report on the development of the resonant mass detector equiped with the Fabry-Perot laser transducer at ICRR, University of Tokyo and estimate the performance of the whole system. I attempt to make clear remaining technical problems to achieve the higher sensitivity of the laser transducer and develop techniques for room temperature long-term operation in the future when the sensitivity achieves the level as those of cryogenic detectors.

I begin by summerizing briefly the necessary physical background about gravitational waves and a general view of gravitational wave detectors in Chapter 2. Chapter 3 reviews the resonant mass detectors: the current detectors, the transducers and the noise of the detectors. Chapter 4 and 5 present a mathematical description of the resonant mass antenna of ICRR and the principle of the laser transducer, respectively. The optical, mechanical, and servo control design of the laser transducer are detailed in Chapter 6. Chapter 7 discusses experimental data of the laser transducer. In Chapter 8, the conclusion, I summarize the results of the development of the laser transducer and the resonant mass detector of ICRR, and discuss the technical problems and the prospect of further improvements.

Chapter 2

Gravitational Waves

2.1 Gravitational Waves in General Relativity

Einstein's general relativity explains the relation between gravity and the curvature of spacetime which is produced by mass, *i.e.*, expresses the geometry of spacetime [1, 2, 3, 4, 5]. The theory predicts that accelerated motions of massive objects such as a supernova and the coalescence of a binary system can produce ripples in the spacetime curvature, known as gravitational waves which propagates in flat spacetime at the speed of light.

The metric tensor contains all of the information about spacetime curvature. The metirc tensor $g_{\mu\nu}$ that contain perturbations from the metric tensor $\eta_{\mu\nu}$ of Minkowski spacetime (*i.e.*, flat spacetime) is written

$$g_{\mu\nu} = \eta_{\mu\nu} + h_{\mu\nu}, \tag{2.1}$$

where $h_{\mu\nu}$ is the extremely small perturbation due to spacetime disturbance. For this metric tensor the Einstein field equation in vacuum can be linearized by assuming suitable gauge transformations:

$$\left(\nabla^2 - \frac{1}{c^2}\frac{\partial^2}{\partial t^2}\right) h_{\mu\nu} = 0. \tag{2.2}$$

Eq.(2.2) is a wave equation, which indicates that the perturbation in Minkowski spacetime propagates at the speed of light; it is called a gravitational wave.

For simplicity, consider plane waves with wavenumber k propagating in the x^3, *i.e.*, z, direction. By imposing the Transverse Traceless gauge (T-T gauge):

$$h^{\alpha}_{\mu\nu,\alpha} = 0, \quad h_{\mu 0} = 0, \quad h_{kj,j} = 0, \quad h_{kk} = 0, \tag{2.3}$$

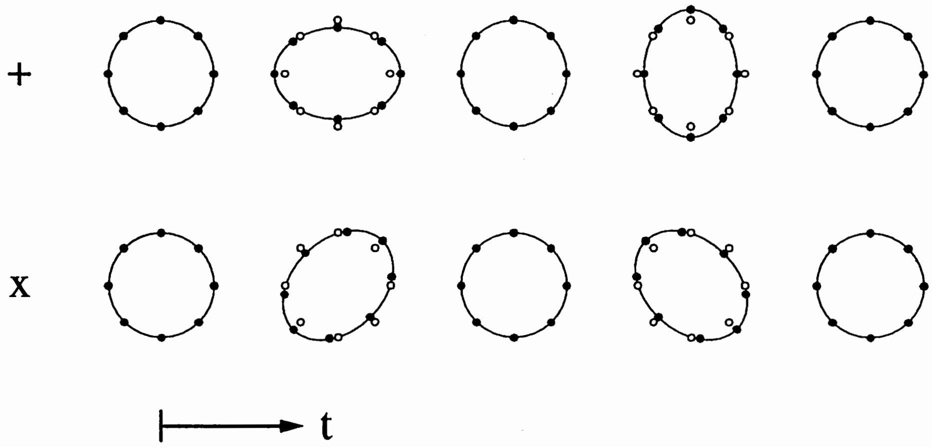

Figure 2.1: Illustration of two polarizations of a gravitational wave

one can obtain $h_{\mu\nu}$,

$$h_{\mu\nu} = \begin{pmatrix} 0 & 0 & 0 & 0 \\ 0 & h_+ & h_\times & 0 \\ 0 & h_\times & -h_+ & 0 \\ 0 & 0 & 0 & 0 \end{pmatrix} \exp\left[ik(-ct+z)\right]. \tag{2.4}$$

This indicates that gravitational waves are transverse waves and have two polarization states: the + mode and the × mode are shown in Fig. 2.1:

$$\begin{pmatrix} 0 & 0 & 0 & 0 \\ 0 & h_+ & 0 & 0 \\ 0 & 0 & -h_+ & 0 \\ 0 & 0 & 0 & 0 \end{pmatrix} \text{and} \begin{pmatrix} 0 & 0 & 0 & 0 \\ 0 & 0 & h_\times & 0 \\ 0 & h_\times & 0 & 0 \\ 0 & 0 & 0 & 0 \end{pmatrix}. \tag{2.5}$$

The quadrupole radiation is the dominant radiation in gravitational waves, because conservation of energy and momentum suppress monopole and dipole radiation.

The strain amplitude of the gravitatinal wave, h, which is estimated by the quadrupole monment of the source, Q, is

$$h \simeq \frac{2G}{c^4}\frac{\ddot{Q}}{r}, \tag{2.6}$$

where G is Newton's gravitational constatnt and r is a distance from a source. Assuming that the mass of the gravitational wave source is M and its velocity is v, then Eq.(2.6) gives

$$h \sim \frac{G}{c^4}\frac{Mv^2}{r}, \tag{2.7}$$

$$\sim \frac{G}{c^4}\frac{E_{\mathrm{kinetic}}}{r}, \tag{2.8}$$

where the kinetic energy E_{kinetic} is the non-spherical component of the source's motions. Eq.(2.8) can be simplified to

$$h \sim 10^{-18}\left(\frac{M}{M_\odot}\right)\left(\frac{10\mathrm{kpc}}{r}\right)\left(\frac{v}{c}\right)^2, \tag{2.9}$$

where $M_\odot$ is the solar mass and 10 kpc is a typical distance of a source from the earth in our galaxy. These estimates show that in order to detect gravitational waves, we must construct a detector sensitive to a strain amplitude level $10^{-17} \sim 10^{-18}$ or better.

2.2 Sources of Gravitational Waves

Non-spherically symmetric acceleration of mass generates gravitational waves. Since the time dependence of the quadrupole moment is the main term, a binary system will certainly radiate. While a perfectly symmetrical collapse of a supernova will not produce gravitational waves, a non-spherically symmetric one will. Various kinds of sources are expected; supernovas, coalescing binary systems, pulsars and stochastic backgrounds. Gravitational waves due to the coalescence of neutron star binaries could be observed by sensitive detectors during the final stages of coalescence. Such waves and those due to supernovas are the main targets for the gravitational wave detection effort. The expected strain amplitude and frequency of the above sources are shown in Table 2.1. There is a good review of sources by K. Thorne [4].

I present typical sources (supernovas and coalescing binary systems) that current astrophysical theory predicts.

2.2.1 Supernova Explosions

Eq.(2.9) indicates that powerful gravitational waves should be received in the following situation: a star is massive, it explodes asymmetrically with a typical velocity $v \sim c$, and its distance from the earth, r, is small. A supernova explosion in our galaxy is one such phenomenon. Supernova explosion is a violent gravitational collapse during the final stage in the life of a massive star ($M \geq 10M_\odot$), which throws off its outer layer dramatically, while the remaining mass forms a neutron star at the center. However, as mentioned above, since a spherically symmetric collapse process never produces a gravitational wave, the star

Sources	Frequency	Amplitude	Event rate	Detection
Coalescing binary neutron stars ($\sim$ 200Mpc)	10Hz $\sim$ 1kHz	10^{-22}	$\sim$ 3 / year	Interferometer and template
Supernovas (in our galaxy)	$\sim$ 1kHz	10^{-18}	$\sim$ 3 / century	Interferometer resonant detector
Supernovas (in Virgo cluster)	$\sim$ 1kHz	10^{-21}	several / year	Interferometer
Black hole formations	$\sim$ 1mHz	10^{-17}	1 / year	Interferometer in space
Pulsars	10Hz $\sim$ 1kHz	10^{-25}	Periodic	Interferomater resonant detector
Cosmic strings	10^{-7}Hz	10^{-15}	Stochastic	Pulsar timing

Table 2.1: Sources of gravitational waves

should have rotational angular momentum, which will drive a non-spherically symmetric collapse. If the angular momentum of a star close to collapse could be observed, one could estimate the expected strain amplitude. Unfortunately, we don't have a method to observe it directly, and furthermore, observations of the rotational periods of neutron stars, from which can be derived the angular momentum before the explosions, suggest that the process of gravitational collapse is typically almost spherically symmetric.

A numerical simulation assuming a particular angular momentum gives an estimate of the strain amplitude of axially symmetric supernova explosions [24]. The energy radiated as gravitational waves is found to be

$$\Delta E_{\mathrm{GW}} \leq 10^{-7} M_{\odot} c^2. \tag{2.10}$$

From Eq.(2.9), at the average distance of supernovas ($\sim$ 20 Mpc) this energy corresponds to

$$h \leq 10^{-23}, \tag{2.11}$$

which is too small to be detected. This is because the axial symmetry suppresses the quadrupole moment. Moreover a latest theoretical work reports that gravitational radiations from supernova explosions carry frequency components around 100 Hz mainly, and components near 1 kHz are small amplitudes. This make resonant detectors under great disadvantages because resonant frequencies of most detectors are in the frequency region from about 800 Hz to 2 or 3 kHz.

Considering an extremely optimistic case, however, the angular momentum is much larger, the collapse causes larger axial asymmetry, and the core could form a massive disk that fragments into many small objects, powerful gravitational waves accounting for as much as 1 % of the total released energy could be radiated. The energy of gravitational waves is

$$\Delta E_{\mathrm{GW}} \leq 10^{-2} M_{\odot} c^2, \tag{2.12}$$

and this energy produces a strain amplitude

$$h \leq 10^{-21}, \tag{2.13}$$

which is within the sensitivity of large scale interferometers, and supernova explosions in our galaxy, $r \sim 10$ kpc, might be detectable sources, $h \leq 10^{-18}$ for resonant mass gravitational wave detectors. It is considered that supernova explosins would radiate burst waves which have wide-band frequency components in a short time interval. Resonant mass detectors are made to fit those resonances to near the frequency of burst waves, whose energy is largest. As mentioned above, however, mainly carried frequency components from supernovas are near 100 Hz, resonant mass detectors whose sensitivity are limited at the order of the 10^{-19}, and which are designed to catch higher frequencies near 1 kHz, could not detect burst waves even if their sources are in our Galaxy.

2.2.2 Coalescing Binary Systems

In our universe a lot of binary systems with one compact star (a white dwarf, a neutron star or a black hole) exis, because almost stars are part of binaryt systems. Although such binary systems can radiate gravitational waves, they are very weak and their frequencies are very low, equal to twice the orbital frequency ($\sim 10^{-4}$ Hz). Moreover they are unlikely to coalesce due to the energy loss of gravitational radiation within the age of our universe.

On the other hand, a few binary systems will evolve to have two compact stars which are neutron-neutron, neutron-black hole, and black hole-black hole. The neutron star-neutron star system PSR 1913+16 (5 kpc from the Earth) radiates currently gravitational waves with only the strain amplitude $h \sim 10^{-23}$ on the Earth, but its two neutron stars will coalesce 3×10^8 years from now because of gravitational radiation, and then it radiates at a detectable magnitude ($h \sim 5 \times 10^{-18}$). PSR 2127+11C and PSR 1534+12 are the same type of system as PSR 1913+16 in our galaxy, and will coalesce within 2×10^8 years and 3×10^9 years, respectively: the neutron star-neutron star merger rate was extracted by E.S. Phinney [29], 10^{-6} yr^{-1}.

Gravitational wave forms radiated from binary neutron stars have been calculated [25, 26, 27], and these detailed simulations show that chirp, *i.e.*, a 100 Hz $\sim$ 1 kHz quasi-sinusoidal wave, is radiated during the last stage of the coalescence. The strain amplitude and the rate of change of frequency are

$$h = 10^{-23}\left(\frac{M_T}{M_\odot}\right)^{\frac{2}{3}}\left(\frac{\mu}{M_\odot}\right)\left(\frac{f}{100\text{Hz}}\right)^{\frac{2}{3}}\left(\frac{100\text{Mpc}}{r}\right), \tag{2.14}$$

and

$$\dot{f} = 13\left(\frac{M_T}{M_\odot}\right)^{\frac{2}{3}}\left(\frac{\mu}{M_\odot}\right)\left(\frac{f}{100\text{Hz}}\right)^{\frac{11}{3}}[\text{Hz/s}], \tag{2.15}$$

where M_T is the total mass of a binary, μ is the reduced mass and f is the instantaneous frequency of the gravitational wave.

The expected event rate of coalescences within 200 Mpc is estimated to be about 3 per year [28, 29]. In practice, there are many uncertain factors in the estimation of the event rate. In particular the estimation depends on the existence of only 3 neutron star binaries in our galaxy. However, in spite of the uncertainty of the event rate, since the strain amplitude is confidently expected to be $h \sim 10^{-21}$, the coalescence of neutron star binaries should present detectable targets for gravitaional wave detections. Unfortunately, resonant mass detectors are not available to detect the chirp waves from coalescing binary systems. Because it is very difficult to achieve the sensitivity $h \sim 10^{-21}$ and they are sensitive only at their resonant frequency and can not follow the gravitational wave from the coalescenc of neutron star binary systems, whose frequency evolves until the time of coalescence.

2.3 Principles of Detection

Gravitational waves in flat spacetime can be detected by measuring the small change ζ^μ of the distance between two test masses in free fall.

The geodesic deviation law gives

$$\frac{d^2\zeta^\mu}{d\tau^2} = -c^2 R^\mu{}_{0\nu 0} x_0^\nu, \tag{2.16}$$

where $R^\mu{}_{0\nu 0}$ is the Riemann tensor, x_0^ν is the initial distance between the masses and ζ_0^μ is quite smaller than x_0^μ. In the approximation that the velocity of the test mass is smaller than c and $\zeta^0 = 0$, $\ddot{\zeta}_\mu$ is given by

$$\ddot{\zeta}_\mu \cong \frac{1}{2}\sum_{\nu=1}^{3}\ddot{h}_{\mu\nu}x^\nu. \tag{2.17}$$

Considering a gravitaional wave propagating along z-axis with polarization h_+ and $h_\times$, putting one test mass at the origin of the system and the other at the position (x, y).

Project name	Arm length	Site	(Country)
LIGO	4 km & 2 km 4 km	Hanford (WA) Livingston (LA)	(U.S.A.) (U.S.A.)
VIRGO	3 km	Pisa	(Italy&France)
GEO600	600 m	Hannover	(Germany&Britain)
TAMA300	300 m	Mitaka	(Japan)
AIGO	1 km	??	(Australia)

Table 2.2: Interferometric gravitational wave detectors: List of long-base line projects

Eq.(2.16) becomes

$$\begin{aligned}\ddot{\zeta}_x &= \frac{1}{2}(xh_+ + yh_\times),\\ \ddot{\zeta}_y &= \frac{1}{2}(xh_\times - yh_+),\\ \ddot{\zeta}_z &= 0.\end{aligned}$$

This shows that the effect of gravitational waves cannot be observed with a single test mass. To detect the effect of gravitational waves, we should measure the relative displacement between two test masses in free fall or "tidal" force on material; gravitational waves act on the mass m like an external force $m\ddot{\zeta}_\mu = (m/2)\sum \ddot{h}_{\mu\nu}x^\nu$.

Free falling test masses can be realized only in space. A spacecraft tracking and a space interferometer are gravitational wave detectors in space, have been planned and are being developed. The spacecraft tracking measures irregularities in the time-of-communication residuals of microwave signals from interplanetary probes. The space interferometer is a space-borne implementation of a Michelson interferometer. The LISA project of the Eurpean Space Agency [30] is in progress and will search for extremely low-frequency (mHz) gravitational waves which will never be detectable by ground-based interferometers because of terrestrial disturbances.

On Earth we must support the two test masses against gravity. Ground-based gravitational wave detectors can be classified into two categories, the laser interferometers and the resonant mass detectors.

The laser interferometers have mirrors suspended as pendulums for the test masses, which are independent each other, and are designed to detect diffrential motions caused by gravitational waves between each arm. The seeds of the idea of the interferometers can be found in early papers by Pirani [31], and Gertsenshtein and Pustovoit [32]. It was realized in the early 1970s that the interferometers might have a better chance of detecting gravitational waves, after which various people especially Weiss [33] and Moss [34] promoted the development of a practical interferometer. Since then, much research, for example [35, 36], has established the feasibility of the Fabry-Perot Michelson interferometer, and large scale version projects are in progress in many countries. Table 2.2 shows current interferometer projects.

The resonant mass detectors have the elastically linked two test masses and catch tidal forces produced by gravitatinal waves. We will discuss in details the resonant mass detectors in the next chapter.

Chapter 3

Resonant Mass Detectors

The history of attempts to detect gravitational waves began in the 1960s with the famous experiments of J. Weber [12]. Weber's gravitational wave detector consisted of a resonant mass antenna called a "Weber bar" and a piezo-electric transducer.

Since Weber's pioneering work, continuous studies over 30 years have borne many detectors which attains the sensitivity, the order below 10^{-18}. These detectors could detect a supernova explosion in our galaxy. However the order of 10^{-18} is extracted when sources are optimistic ones. When a supernova explosion is an axially symmetric one, the sensitivity must be less than 10^{-20} from Eq.(2.11) even if the source is in our Galaxy. No cryogenic detector achieves the sensitivity $< 10^{-20}$. Thecnical problems to attain this level are very difficult. Morover there is a theoretical wrok indicating that the resonant frequency of the antenna is too high to catch burst waves from supernova explosions and main frequences of burst waves are from 100 Hz to 200 Hz. In this case, present resonant mass detectors could not detect gravitational waves at all. Many research are needed.

Institute	Antenna	Transducer	Sensitivity
CERN	Al5056, 2.3 t, 2.6 K	Capacitive+dc SQUID	7×10^{-19}
Frascati	Al5056, 2.3 t, 0.1 K	Capacitive+dc SQUID	2×10^{-19}
LSU	Al5056, 2.3 t, 4.2 K	Inductive+dc SQUID	6×10^{-19}
Stanford U.	Al6061, 4.8 t, 4.2 K	Inductive+dc SQUID	6×10^{-19}
UWA	Niobium, 1.5 t, 5.7 K	RF Cavity	7×10^{-19}
KEK(Japan)	Al5056, 1.2 t, 4.2 K	Capacitive+FET	4×10^{-22}

Table 3.1: Current status of resonant mass detectors

In this chapter, I present the principle and a detailed mathematical description of a resonant mass detector: an antenna, a transducer, and the expected sensitivity. There is a good review by K. Throne [4] and Table 3.1 lists present second generation resonant mass detectors.

3.1 A Resonant Mass Antenna

We can often treat that a resonant mass antenna as a system of two or more masses linked by springs, *i.e.*, a harmonic oscillator whose quadrupole moment is excited by the tidal force of a gravitational wave.

But since an actual antenna is an elastic body, it is more accurately considered to be a collection of a large number of harmonic oscillators with separate vibrational motion modes. The response of each normal mode [1] to a gravitational wave can be treated independently as an interaction with a simple harmonic oscillator. The vibrational motion on resonance is amplified by the quality factor of the mode, Q. If the Q is high, a vibration caused by a passing gravitational wave will decay slowly. Thus the resonant mass antenna uses a large mass with some resonant modes of high Q whose vibrational motion is monitored by a transducer.

3.1.1 Different Types of Antennas

The solid body of the antenna was traditionally a cylinder; that is why resonant mass detectors are usually called "bar detectors". However now other shapes are being used: a disk type which ICRR's gravitational wave group has developed, and a sphere or sphere-like object such as a truncated icosahedron, for example GRAIL in The Netherlands or TIGA at Louisiana State University [37, 38, 39]. The antenna is usually made of an aluminum alloy with a high mechanical quality factor and is several meters in length and several tons in weight. ICRR's antenna is made of an aluminum alloy 5052, and is 2 m in diameter, 1.7 t in weight. Occasionally, other materials are used, *e.g.*, quartz, sapphire or niobium. Since the antenna shape and its material determine the frequencies of its normal modes, they must be chosen to make the frequencies of the normal modes which have quadrupole moments about 800 Hz $\sim$ 1 kHz, which is the expected frequency region of gravitational wave bursts.

The first bar detectors were operated at room temperature, but the present generation of bars is operating below liquid-helium temperature. The next generation, which is under construction (NAUTILUS in Frascati [14], AURIGA in INFN Legnaro [15]), will operate at a temperature around 50 mK. Operating at low temperature decreases the antenna's thermal noise, which is a very important factor to limit the sensitivity. Although these cryogenic detectors cannot have the same high sensitivity and wide frequency bandwidth

[1] Of course, there are modes not to be excited by gravitational waves, beause they do not have quadrupole moments.

as large-scale interferometers, they sustain stable operation at cryogenic temperature for more than 1 year, which interferometers have not yet achieved. It is an important fact to stress that gravitational wave detectors are in stable long term operation.

In following Section 3.1.2 and 3.1.3, I present a breif mathematical description of equation of motion of a resonant antenna and reception of gravitational waves. There are good texts which teach a theory of antennas for gravitational radiation [5, 40]

3.1.2 Equation of Motion of a Resonant Mass Antenna

Since a resonant mass antenna consists of a solid elastic body, it obeys the equation of motion

$$\rho \frac{\partial^2 \vec{u}}{\partial t^2} - \mu \Delta \vec{u} - (\lambda + \mu) \mathrm{grad}\, \mathrm{div} \vec{u} = 0, \tag{3.1}$$

where ρ is the density of the mass, λ and μ are Lamé's constants, and $\vec{u}$ is the displacement vector [41]. If a gravitational wave h_{ij} acts on the mass like an external force, then the equation of motion of the antenna is

$$\rho \ddot{u}_i - \mu \Delta u_i - (\lambda + \mu) \frac{\partial^2 u_j}{\partial x_i \partial x_j} = \frac{1}{2} \rho \ddot{h}_{ij} x_j. \tag{3.2}$$

We want to put this in terms of the normal modes of the antenna. Separarting the mode displacement $\vec{u}(t, x)$ into the amplitudes $\xi_n(t)$ and the mode patterns $\vec{w}_n(x)$

$$\vec{u}(t, x) = \sum_n \xi_n(t) \vec{w}_n(x), \tag{3.3}$$

we obtain

$$\rho \omega_n^2 w_{ni} + \mu \Delta w_{ni} + (\lambda + \mu) \frac{\partial^2 w_{nj}}{\partial x_i \partial x_j} = 0. \tag{3.4}$$

The reduced mass μ_n of the nth normal mode is defined so that the kinetic energy T is given by the usual expression in terms of the displacement which the transducer monitors:

$$T = \frac{1}{2} \int \left| \frac{\partial \vec{u}}{\partial t} \right| dV = \frac{1}{2} \sum_n \mu_n \dot{\xi}_n^2(t). \tag{3.5}$$

From Eqs.(3.3) and (3.5), the reduced mass is given by

$$\mu_n = \int \rho \left| \vec{w}_n \right|^2 dV, \tag{3.6}$$

where V is volume and the equation of motion is

$$\rho\ddot{\xi}_n w_{ni} + \rho\omega_n^2 \xi_n w_{ni} = \frac{1}{2}\rho\ddot{h}_{ij}x_j. \tag{3.7}$$

Integrating Eq.(3.7) multiplied by w_{ni} on both sides, we obtain

$$\mu_n\ddot{\xi}_n + \mu\omega_n^2\xi_n = \frac{1}{2}\int \rho\ddot{h}_{ij}x_j w_{ni} dV = \frac{1}{4}\ddot{h}_{ij}q_{nij}, \tag{3.8}$$

where the integral is over the entire volume of the antenna. Since the wavelengths of typical gravitational waves are much larger than the scale of the antenna, we can assume that $\ddot{h}_{ij}$ is approximately constant. Allowing for the internal friction of the elastic body, the equation of motion of the antenna is that of a harmonic oscillator excited by an external force, and with a damping term, *i.e.*,

$$\mu_n\left(\ddot{\xi}_n(t) + \frac{\omega_n}{Q_n}\dot{\xi}_n(t) + \omega_n^2\xi_n(t)\right) = \frac{1}{4}\ddot{h}_{ij}q_{nij}, \tag{3.9}$$

where ω_n is the resonant frequency of nth normal mode, Q_n is the quality factor of the mode, and q_{nij} is the quadrupole moment[2], which is an important factor giving the connection between a gravitational wave and the antenna:

$$q_{nij} = \partial_{\vec{w}_n}\mathrm{Q}_{ij} = \int \rho(w_{ni}x_j + w_{nj}x_i - \frac{2}{3}\delta_{ij}w_{nk}x_k)dV \tag{3.10}$$

3.1.3 Gravitational Wave Energy absorbed in the Antenna

A gravitational wave acts on a resonant mass antenna like an external force. In the case of a burst wave, which occurs within a short period, we can approximate the effect by a purely impulsive force. We can also neglect the damping of the vibrational motion. From Eq.(3.8), ξ is expected to be

$$\xi = \frac{1}{4\mu\omega}\int_{-\infty}^{t} \sin\omega\,(t-s)\,\ddot{h}_{ij}q_{ij}ds. \tag{3.11}$$

The antenna's kinetic energy is given by

$$\begin{aligned} E &= \frac{1}{2}\mu\omega^2\xi^2 \\ &= \frac{1}{32\mu}\left(\int_{-\infty}^{t} \sin\omega\,(t-s)\,\ddot{h}_{ij}q_{ij}ds\right)^2. \end{aligned} \tag{3.12}$$

[2]The mass quadrupole moment of the antenna mass, $\mathrm{Q}_{ij} = \int \rho(x_i x_j - \frac{1}{3}\delta_{ij}x_k x_k)dV$.

It is convenient to write h_{ij}'s space components in terms of two polarizations, the + mode and the $\times$ mode, as

$$h_{ij} = h_+ \mathrm{e}^+ + h_\times \mathrm{e}^\times, \tag{3.13}$$

where

$$\mathrm{e}^+ = \begin{pmatrix} 1 & 0 & 0 \\ 0 & -1 & 0 \\ 0 & 0 & 0 \end{pmatrix}, \tag{3.14}$$

and

$$\mathrm{e}^\times = \begin{pmatrix} 0 & 1 & 0 \\ 1 & 0 & 0 \\ 0 & 0 & 0 \end{pmatrix}. \tag{3.15}$$

In case of a general gravitational wave, since its polarization does not agree with that of the quadrupole mode of the antenna, one must evaluate degree of coupling between the polarization of the gravitational wave and the quadrupole mode pattern of the antenna to calculate the energy absorbed by the antenna.

When a gravitational wave propagating in a certain direction hits the antenna, the antenna is left with an absorbed energy

$$E = \frac{1}{32\mu}\left[\left\{q_{ij}\mathrm{e}^+_{ij}\int_{-\infty}^{t} \ddot{h}_+ \sin\omega\,(t-s)\,ds\right\}^2 + \left\{q_{ij}\mathrm{e}^\times_{ij}\int_{-\infty}^{t} \ddot{h}_\times \sin\omega\,(t-s)\,ds\right\}^2\right]. \tag{3.16}$$

where e^+_{ij} and $\mathrm{e}^\times_{ij}$ are obtained by the rotation of e^+ and $\mathrm{e}^\times$ for the propagating direction (see Fig. 3.1):

$$\mathrm{e}^+_{ij} = R^{-1}(\theta,\phi)\mathrm{e}^+ R(\theta,\phi), \tag{3.17}$$
$$\mathrm{e}^\times_{ij} = R^{-1}(\theta,\phi)\mathrm{e}^\times R(\theta,\phi), \tag{3.18}$$

where

$$R(\theta,\phi) = Y(\theta)Z(\phi), \tag{3.19}$$
$$Y(\theta) = \begin{pmatrix} \cos\theta & 0 & \sin\theta \\ 0 & 1 & 0 \\ -\sin\theta & 0 & \cos\theta \end{pmatrix}, \tag{3.20}$$
$$Z(\phi) = \begin{pmatrix} \cos\phi & \sin\phi & 0 \\ -\sin\phi & \cos\phi & 0 \\ 0 & 0 & 1 \end{pmatrix}. \tag{3.21}$$

The angle dependent component in Eq.(3.16) can be separated out of the integral, and we define the directional pattern of the antenna on the polarizations of the gravitational wave, f^p, as

$$\int \left\{f^+(\theta,\phi) + f^\times(\theta,\phi)\right\} d\Omega = 4\pi, \tag{3.22}$$

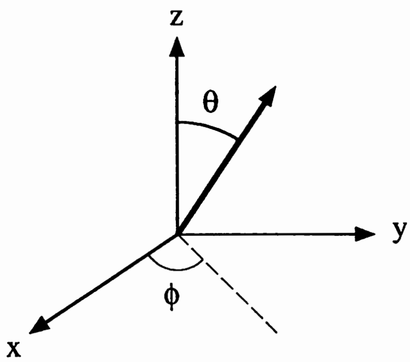

Figure 3.1: The definition of θ and ϕ: the vector denotes the propagating direction of a gravitational wave. It is assumed that x and y direction correspond to the quadrupole + mode of the antenna.

and obtain

$$f^p(\theta,\phi) = \sum_{i,j} \frac{5\left(q_{ij}e^p_{ij}\right)^2}{4q^2_{ij}}. \tag{3.23}$$

The pattern $f^p(\theta,\phi)$ $(p = +, \times)$ is a function which indicates degree of coupling between gravitational waves and the antenna. Finally, the gravitational wave energy absorbed by the antenna is given by

$$E = \frac{\pi G}{10c^3} M\omega^2 A_G f^p(\theta,\phi) F^p(\nu), \tag{3.24}$$

where M is the mass of the antenna, A_G is the effective area of the antenna, and $F^P(\nu)$ is the energy spectrum of the gravitational wave per unit area:

$$M = \int \rho dxdydz, \tag{3.25}$$

$$A_G = \frac{2\sum_{ij}\left(q_{ij}\right)^2}{M\mu}, \tag{3.26}$$

$$F^p(\nu) = \frac{c^3\omega^2}{8\pi G}\left|\int_{-\infty}^{\infty} h_p e^{i\omega t} dt\right|^2. \tag{3.27}$$

In the case of a sinusoidal wave whose frequency agrees with the resonant frequency of the antenna, the right side of Eq.(3.9) is written

$$\frac{1}{4}\omega^2 h_{ij} q_{ij} e^{i\omega t}, \tag{3.28}$$

and we obtain

$$|\xi| = \frac{Q}{4\mu} h_{ij} q_{ij}. \tag{3.29}$$

The gravitational wave energy captured by the antenna is given by

$$\begin{aligned} E &= \frac{1}{2}\mu\omega^2\xi^2 \\ &= \frac{Q^2\omega^2 \left(h_{ij}q_{ij}\right)^2}{32\mu} \\ &= \frac{2\pi G}{5c^3} M Q^2 A_G f^p S^p, \end{aligned} \tag{3.30}$$

where S^p is the energy flux of the gravitational wave in the p polarization:

$$S^p = \frac{c^3\omega^2}{32\pi G} \left|h_p\right|^2. \tag{3.31}$$

Eq.(3.24) and Eq.(3.30) indicate that a larger MA_G increases the gravitational wave energy absorbed by the antenna.

3.2 Types of Transducers

A resonant mass detector is equipped with a transducer that monitors the complex amplitudes of one or more of modes of the antenna's vibrational motion, especially those likely to be excited by a gravitational wave. The principle of all transducers is to store electromagnetic energy in a very small volume, usually a narrow gap, one of the walls of which is part of the antenna. The motion of the wall due to the antenna's vibrational motion induces a modulation of the energy, which is detected and amplified as an electrical signal. Therefore transducers are important in determining the sensitivity to gravitational waves.

Fig. 3.2 shows several kinds of transducers.

Fig. 3.2(a) shows an electro-static or capacitive transducer, which is a passive type of transducer. A capacitor is created between the side of the antenna and a fixed plate, and a DC bias voltage is applied. The antenna's vibrational motion causes small changes of the capacitance, and in turn voltage. The voltage change at the input port of the amplifier, $v(x)$, is given by

$$v(x) = \frac{V_0}{C_0}\frac{dC(x)}{dx}x \approx E_0 x, \tag{3.32}$$

where x is the displacement of the antenna wall, V_0 is the bias voltage, $C_0 \equiv C(0)$, and E_0 is the electric field amplitude of the capacitor.

Fig. 3.2(b) shows an inductive transducer, another type of passive transducer, which comprises a superconducting coil and a SQUID. A change in the distance between the side

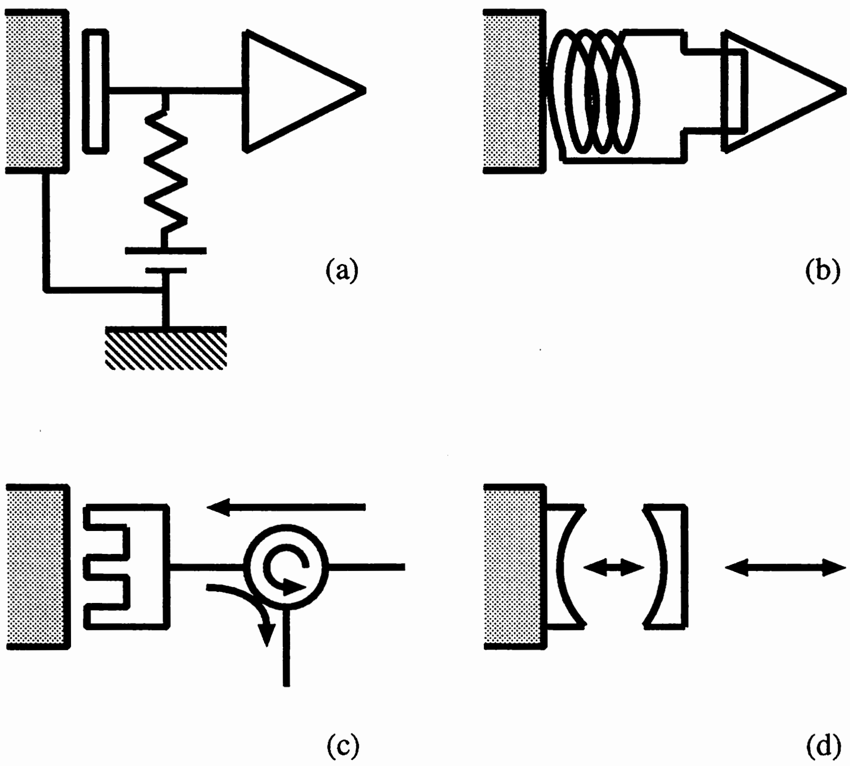

Figure 3.2: Transducers

of the antenna and the coil brings about a change of the inductance of the coil, and in turn an induced current in the coil. The SQUID amplifies this current change. The change of the current, $i(x)$, is given by

$$i(x) = \frac{I_0}{L_0}\frac{dL(x)}{dx}x, \tag{3.33}$$

where I_0 is the bias current, and $L_0 \equiv L(0)$ is the inductance at zero displacement.

Also, there are active types called parametric transducers. Fig. 3.2(c) shows a transducer which uses microwaves in a superconducting cavity. Fig. 3.2(d) is a laser transducer consisting of a Fabry-Perot optical cavity. The groups of G.E. Moss [42], M. Weksler [43], and others have developed various kinds of transducers using laser interferometers. These transducers have the advantage of low loss and low back action to the antenna because they use external pumping sources. Because the pumping source of the laser transducer is a laser, *i.e.*, photons, it can amplify the antenna's vibrational motion to a high gain.

Laser Transducer

J.P. Richard proposed a detector which combines a cryogenic antenna, a multi-mode transducer*i.e.*, a resonant transducer (discussed below), and a Fabry-Perot optical resonator with a high finesse [20]. He measured the finesse at low temperature of the Fabry-Perot cavity, it was 19000 at 4.2 K [21], the displacement sensitivity at room temperature of a rigid FP cavity, which comprised fixed, high quality mirrors with a finesse of 83000, 5.6×10^{-17} m/$\sqrt{\text{Hz}}$, and calculated the sensitivity at cryogenic temperature of the bar antenna instrumented above FP cavity, $h = 6.8 \times 10^{-21}$ at 0.03 K [22]. Richard's group tested the performance of the resonant transducer at room temperature [23]. They uses a low power (1 mW) He-Ne laser to prevent a power dissipation at low temperature. Its sensitivty was 1.0×10^{-15} m/$\sqrt{\text{Hz}}$. When their resonant transducer is installed in the cryogenic bar antenna, assuming mechanical quality factors of 3×10^{6}, they will achieve to sensitivity of 10^{-19} in displacement at 4.2 K.

A Resonant Transducer

Present resonant mass detectors, without exception, incorporate some form of 'resonant' transducer (see Fig. 3.3) which achieves a breakthrough in increasing the sensitivity of detectors. Such a transducer increases the β value, which is the ratio of the signal energy at the input of the electric amplifier to the total signal energy in the system [45]. It consists of a secondary resonator attached to the wall of the antenna, which has a mechanical resonance near the frequency of the antenna. It follows that the vibrational motion induced on the antenna is forwarded by the transducer to the input of the electric amplifier with an amplification of $\sqrt{m_a/m_t}$, where m_t is the equivalent mass of the transducer vibration mode and m_a is the reduced mass of the first longitudinal vibration mode of the bar antenna. Moreover this technique can expand the observation bandwidth for gravitational waves, due to the two normal modes of the antenna-transducer double harmonic oscillator system [44].

3.3 Sensitivity of Resonant Mass Detectors

There are many different noise sources that must be considered to calculate the sensitivity of gravitational wave detectors: the seismic noise of the detector site, the thermal noise of the detector itself, the noise of the signal monitoring system, and many others. The seismic noise is filtered by seismic isolation, *e.g.*, isolation stacks, suspensions. The other noise sources can be reduced by improvements in technology. It is not too much to say that a struggle against noise sources is all of the R&D efforts of gravitational wave detectors.

In the case of resonant mass detectors, the noise source which determines the sensitivity as a gravitational wave detector is indeed the noise of transducer. There is the thermal

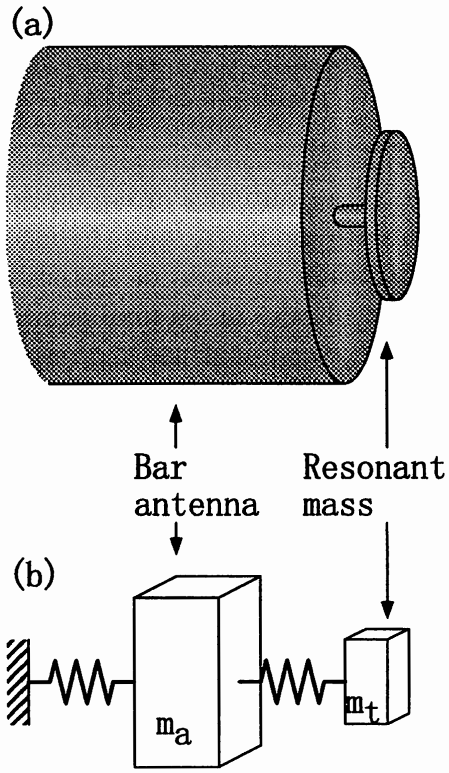

Figure 3.3: The schematic of a resonant transducer:(a) a bar antenna and a resonant mass, (b) the corresponding model of the antenna-transducer harmonic oscillator system

noise of the antenna caused by Brownian motion, too, but the higher sensitivty of the transducer can measure the level less than that of Brownian motion of the antenna.

In this section, let us consider the sensitivity of a resonant mass detector, the thermal noise of the antenna and the noise of the transducer, and express the sensitivity by an effective temperature, T_{eff}, which depends on these noise factors.

3.3.1 Thermal Noise of the Antenna

The resonant mass antenna in the vacuum chamber always keeps the thermodynamic equilibrium with the surrounding heat bath. The antenna comes into contact with the heat bath through direct mechanical coupling, interaction with residual gases in the vacuum chamber, or exchange of photons with the surrounding black body radiation. This contact with the heat bath results in each of the antenna's normal modes being excited to an amplitude such that the nth normal mode has an average energy equal to $\frac{1}{2}k_BT$:

$$\frac{1}{2}\mu_n\omega_n\left\langle \dot{x}^2\right\rangle = \frac{1}{2}k_BT, \tag{3.34}$$

where k_B is Boltzmann's constant. This equation gives the mean square amplitude of excitation for a normal mode of an antenna in equilibrium at temperature T with the effective or reduced mass of the nth mode, μ_n, and the nth eigenfrequency, ω_n. This result is an application of the equipartition theorem of statistical mechanics. That however is only a partial explanation of the physics of thermal equilibrium. In order to describe the antenna's thermal noise in detail, we should use the results of the fluctuation-dissipation theorem and the results of Brownian motion as described by Nyquist [46].

The fluctuation-dissipation theorem gives the relation between the macroscopic frictional force which dissipates energy in a system and the fluctuating forces which excite the same system to thermal equilibrium. As a result of the exchange of energy between the normal modes and the surrounding heat bath, a resistance must appear in the equations which describe the normal modes. The exchange of energy with a particular normal mode is equivalent to a random force with power spectral density [47]:

$$\left\langle F_{thermal}^2(\omega)\right\rangle = 4k_BTR(\omega), \tag{3.35}$$

where $\langle F_{thermal}^2\rangle$ is the power spectral density of the random force and $R(\omega)$ is the mechanical resisitance which enters into the equation of motion for the normal mode. Equivalently, the power spectral density of the motion of the mass is given by

$$\left\langle x_{thermal}^2(\omega)\right\rangle = \frac{4k_BT\sigma(\omega)}{\omega^2}, \tag{3.36}$$

with $\sigma(\omega)$ denoting the mechanical conductance. $R(\omega)$ and $\sigma(\omega)$ are defined in terms of the impedance at the mass as

$$Z = \frac{force}{velocity}, \tag{3.37}$$

$$R(\omega) = Re(Z), \tag{3.38}$$

$$\sigma(\omega) = Re(Z^{-1}). \tag{3.39}$$

In this formulation, the power spectral density is expressed for the customary bandwidth of 1 Hz. For a simple harmonic oscillator, we can write $R(\omega)$ and $\sigma(\omega)$ in terms of the Q of the mode.

$$\left\langle F_{thermal}^2\right\rangle = 4k_BTR(\omega) = 4k_BT\frac{M\omega_0}{Q}, \tag{3.40}$$

$$\left\langle x_{thermal}^2\right\rangle = \frac{4k_BT\sigma(\omega)}{\omega^2} = \frac{4k_BT}{MQ}\frac{\omega_0}{(\omega^2-\omega_0)^2+\left(\frac{\omega_0\omega}{Q}\right)^2}. \tag{3.41}$$

Considering the bandwidth over which the force is measured, Δf, the power spectral density of the force is

$$\begin{aligned} \left\langle F^2_{thermal}(\omega) \right\rangle &= 4k_B T R(\omega)\Delta f & (3.42) \\ &= \frac{4k_B T M\omega_0}{Q}\Delta f. & (3.43) \end{aligned}$$

These equations contain the principal results of the Brownian motion analysis. We see that the mechanical system is continuously being excited by a random force and the mean square amplitude of that force is directly proportional to the temperature T of the system and inversely proportional to the mode Q. Thus we need to lower T and raise Q to decrease the power spectral density of the fluctuating force on the antenna.

3.3.2 Noise of the Transducer

In considering the noise of the transducer, we must deal with a displacement noise and a noise force [48]. The displacement noise, whose spectral density is denoted by ξ_N^2, is output noise of the amplifier to which the signal is fed, and the noise force, which is random, is a back action exerted by the transducer on the antenna. We denote its spectral density f_N^2.

These two noise sources can be also represented in a different way, by defining a "noise temperature" and a "matching coefficient" for the transducer-amplifier combination. The noise temperature T_N can be shown to be given by

$$T_N \equiv \frac{\sqrt{f_N^2 \omega_0^2 \xi_N^2}}{2k_B}. \tag{3.44}$$

The matching coefficient η is defined by

$$\eta \equiv \frac{1}{\mu\omega_0}\sqrt{\frac{f_N^2}{\omega_0^2 \xi_N^2}}. \tag{3.45}$$

It is the ratio between the impedance of the antenna mechanical system, $\mu\omega_0$, and the optimum impedance of the transducer, $\sqrt{f_N^2/\omega_0^2\xi_N^2}$, and indicates the strength of the electromechanical coupling in the antenna-transducer combination.

The effect of these quantities in an actual measurement depends on the method of signal processing. Now we trace the signal processing for the case that the signal is a pulse (the signal duration $\lesssim 1/\omega_0$).

The equation of motion of the antenna sujected to an general external force $f(t)$ is written

$$\mu\Big(\ddot{\xi}(t) + \frac{\omega_0}{Q}\dot{\xi} + \omega_0^2\xi\Big) = f(t). \tag{3.46}$$

Taking the Fourier transform of both sides of Eq.(3.46) gives

$$\xi(\omega) = \mathsf{H}(\omega)\mathsf{F}(\omega), \tag{3.47}$$

$$\mathsf{H}(\omega) = \frac{1}{\mu}\frac{1}{\omega_0^2 - \omega^2 + i\frac{\omega_0\omega}{Q}} \tag{3.48}$$

The response to any external force $f(t)$ is given by its Green function:

$$\begin{aligned} G(t-s) &= \frac{1}{2\pi}\int_{-\infty}^{\infty} \mathsf{H}(\omega)\exp[i\omega(t-s)]d\omega \\ &= \frac{1}{\mu\omega_e}\exp\left[-\frac{t-s}{2\tau_A}\right]\sin(\omega_e(t-s))\theta(t-s), \end{aligned} \tag{3.49}$$

$$\tau_A = \frac{Q}{\omega_0}, \tag{3.50}$$

$$\omega_e = \omega_0\sqrt{1-\frac{1}{4Q^2}} \simeq \omega_0 \quad (Q \gg 1). \tag{3.51}$$

Since the transducer's noise, the displacement noise ξ_N and the back action f_N are approximately white noise near the antenna resonance, the total diplacement noise which the transducer detects is given by

$$\xi(t) = \frac{1}{\mu\omega_0}\int_{-\infty}^{t} \exp[-\frac{t-s}{2\tau_A}]\sin[\omega_0(t-s)]\{f_T(s)+f_N(s)\}ds + \xi_N(t), \tag{3.52}$$

where f_T is the thermal noise, i.e., the Brownian motion of the antenna.

The displacement of the antenna oscillator can be rewritten

$$\xi(t) = \mathrm{Re}\left[(X_1(t)+iX_2(t))\exp(-i\omega_0 t)\right], \tag{3.53}$$

$$Z(t) = X_1(t)+iX_2(t), \tag{3.54}$$

where $Z(t)$ is the complex amplitude of the antenna motion. X_1 and X_2 are obtained by lock-in detection using reference signals $\sin\omega_0 t$ and $\cos\omega_0 t$, respectively. Using $Z(t)$, the signal due to energy change of the antenna mode, after the lock-in detection and sampling at intervals of τ is given by

$$D(t) = \mu\omega_0^2\left|Z(t)-Z(t-\tau)\right|^2. \tag{3.55}$$

Thus the average value of the energy change of the antenna mode due to noise is given by

$$D_N = \mu\omega_0^2\left\langle\left|Z_N(t)-Z_N(t-\tau)\right|^2\right\rangle \tag{3.56}$$

$$= \frac{f_T^2\tau}{4e\mu} + \frac{f_N^2\tau}{4e\mu} + \frac{(1-e^{-1})\,\mu\omega_0^2\xi_N^2}{\tau}. \tag{3.57}$$

Substituting Eqs.(3.44) and , (3.45) into Eq.(3.57), we obtain

$$D_N = \frac{k_B T \omega_0 \tau}{\mathrm{e}Q} + 2k_B T_N \left(\frac{\eta \omega_0 \tau}{4\mathrm{e}} + \frac{1-\mathrm{e}^{-1}}{\eta \omega_0 \tau} \right). \tag{3.58}$$

Optimum matching conditions for the transducer noise, $\eta\omega_0\tau = 2\sqrt{\mathrm{e}-1} \sim 2.6$, gives

$$D_N \geq \frac{k_B T}{\eta Q} + k_B T_N, \tag{3.59}$$

where η, as mentioned above, is the fraction of the energy deposited in the antenna which would be converted into electromagnetic energy by a noiseless transducer[3]. Then the effective temperature of the detector is defined as

$$T_{eff} = \frac{D_N}{k_B}. \tag{3.60}$$

These equations show that the noise of the detector can never be lower than the noise temperature of the transducer T_N. In other words, a low noise transducer with large β can realizes the high sensitivity equal to the cryogenic detectors at room temperature.

From Eq.(3.57), the optimum sampling interval is obtained

$$\tau_{opt} = 2\mu\omega_0 \sqrt{\frac{(\mathrm{e}-1)\,\xi_N^2}{f_T^2 + f_N^2}}, \tag{3.61}$$

and it is generally considered that $T_N \ll T$, the term of $\langle f_N^2 \rangle$ can be neglected, we obtain

$$\tau_{opt} = 2\mu\omega_0 \sqrt{\frac{(\mathrm{e}-1)\,Q\,\langle \xi_N^2 \rangle}{4\mu k_B T \omega_0}}. \tag{3.62}$$

and also τ_{opt} gives the effective temperature T_{eff},

$$T_{eff} = \frac{2\omega_0 \tau_{opt}}{\mathrm{e}Q} T. \tag{3.63}$$

In this case, the detectable minimum energy spectral density of gravitational waves is

$$\begin{aligned} F_{min} &= \frac{20c^3 k_B T_{eff}}{\pi G A_G M \omega_0^2} \\ &\sim \frac{20c^3}{\pi G A_G M \omega_0^2} \left(\frac{\omega_0 \tau_{opt}}{\mathrm{e}Q} k_B T + \frac{1-\mathrm{e}^{-1}}{\tau_{opt}} \mu\omega_0^2 \left\langle \xi_N^2 \right\rangle \right), \end{aligned} \tag{3.64}$$

[3] β depends on the transducer and should be made as large as possible.

where the directivity pattern is averaged over the propagating direction and polarization of the gravitational wave.

The detector's signal-to-noise ratio S/N is defined as

$$\frac{\mathrm{S}}{\mathrm{N}} = \frac{E_a}{k_B T_{eff}}, \tag{3.65}$$

where E_a is the gravitational wave energy captured by the antenna.

The Quantum Limit

From the uncertainty principle applied to the antenna, the limit of detectability for a direct measurement is

$$\Delta\xi_{min} \sim \left(\frac{\hbar}{\mu\omega_0}\right) = 3 \times 10^{-21} \left(\frac{1000\mathrm{kg}}{\mu}\right) \left(\frac{10^4\mathrm{s}^{-1}}{\omega_0}\right) \ [\mathrm{m}]. \tag{3.66}$$

It had been thought that this quantum limit could never be overcome, but in a series of papers by Braginsky [49, 50] a method which overcomes this limit, a "quantum nondemolition" method, was proposed.

In conclusion, to make a sensitive detector one has to choose an antenna cooled to a temperature as low as possible and a transducer of high η, high Q and a low noise temperature.

Chapter 4

The Resonant Antenna and the Laser Transducer of ICRR

The resonant mass detector in ICRR was designed to look for gravitational wave bursts from sources in our galaxy at room temperature. The antenna shape of previous detectors has normally been a bar, and disk antennas have been rare. This detector is currently the only one whose antenna is a disk. The reason that the disk was chosen in ICRR is that disk antennas are suitable for the instrumentation of a laser interferometer.

In this section, I present the ICRR disk antenna in detail with a mathematical description.

4.1 The Disk

The resonant mass antenna at ICRR is located underground in the former "Mutron" experiment building at the Institute for Cosmic Ray Research (ICRR), Univ. of Tokyo, in Midori-tyo 3-2-1, Tanashi City, Tokyo. It comprises a disk, a support rod, and a small upper disk. The antenna proper is a disk of aluminum alloy 5052, 2 m in diameter and 20 cm in thickness. It has a physical mass of about 1700 kg. Its quadrupole modes are at about 1.2 kHz, as discussed below. A disk antenna is most sensitive to gravitational waves propagating in a direction perpendicular to the disk. The disk, supported at its center, is installed on isolation stacks in a vacuum tank. Figure 4.1 shows the antenna installed in the vacuum tank.

Figure 4.2 shows the outline of the antenna from above. The upper disk is used for mounting the optical and mechanical components; a breadboard for optics is fixed to it.

The vacuum tank is equipped with a diffusion pump and a turbo-molecular pump (SEIKO SEIKI STP400) and is set up in the basement of the building. Together the pumps can evacuate the tank to $10^{-6} \sim 10^{-5}$ torr. This degree of vacuum is not very high, because

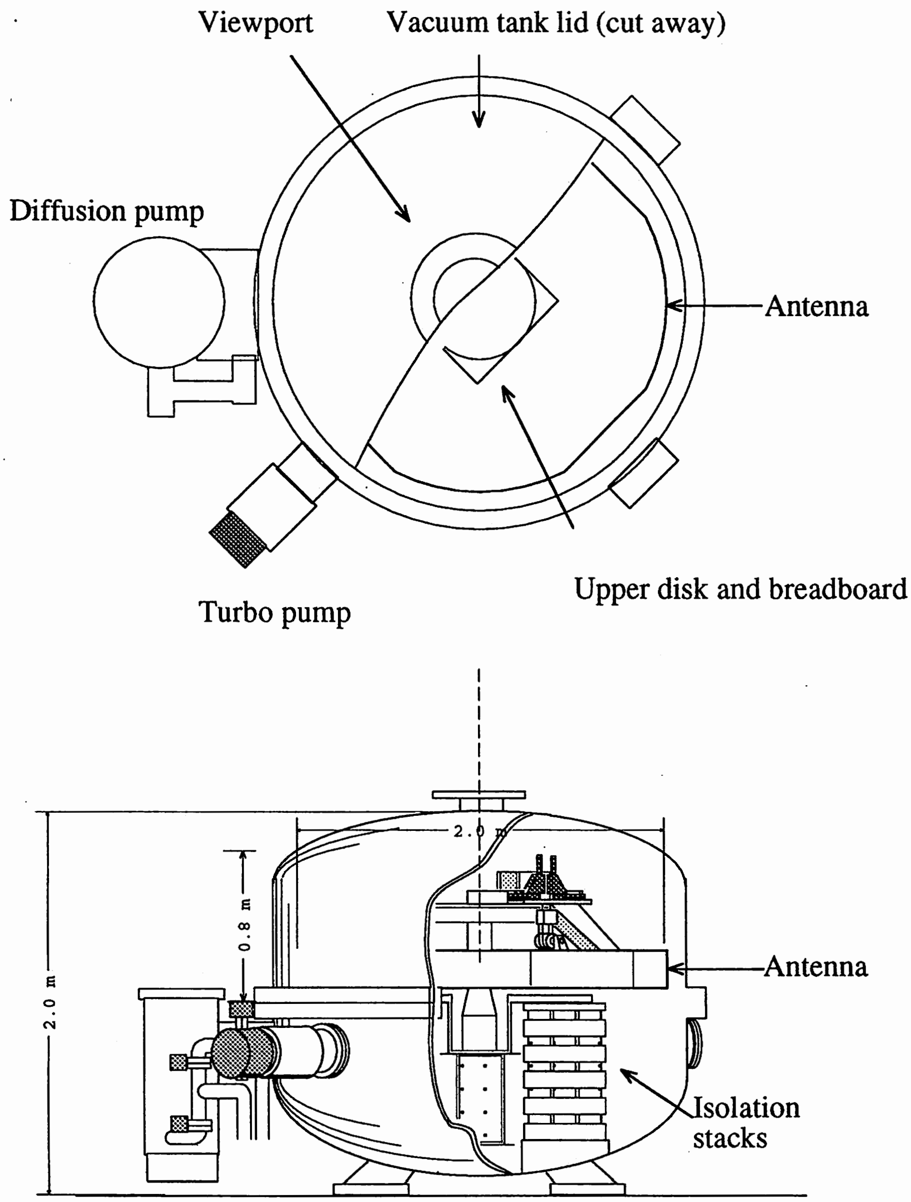

Figure 4.1: The antenna in the vacuum tank

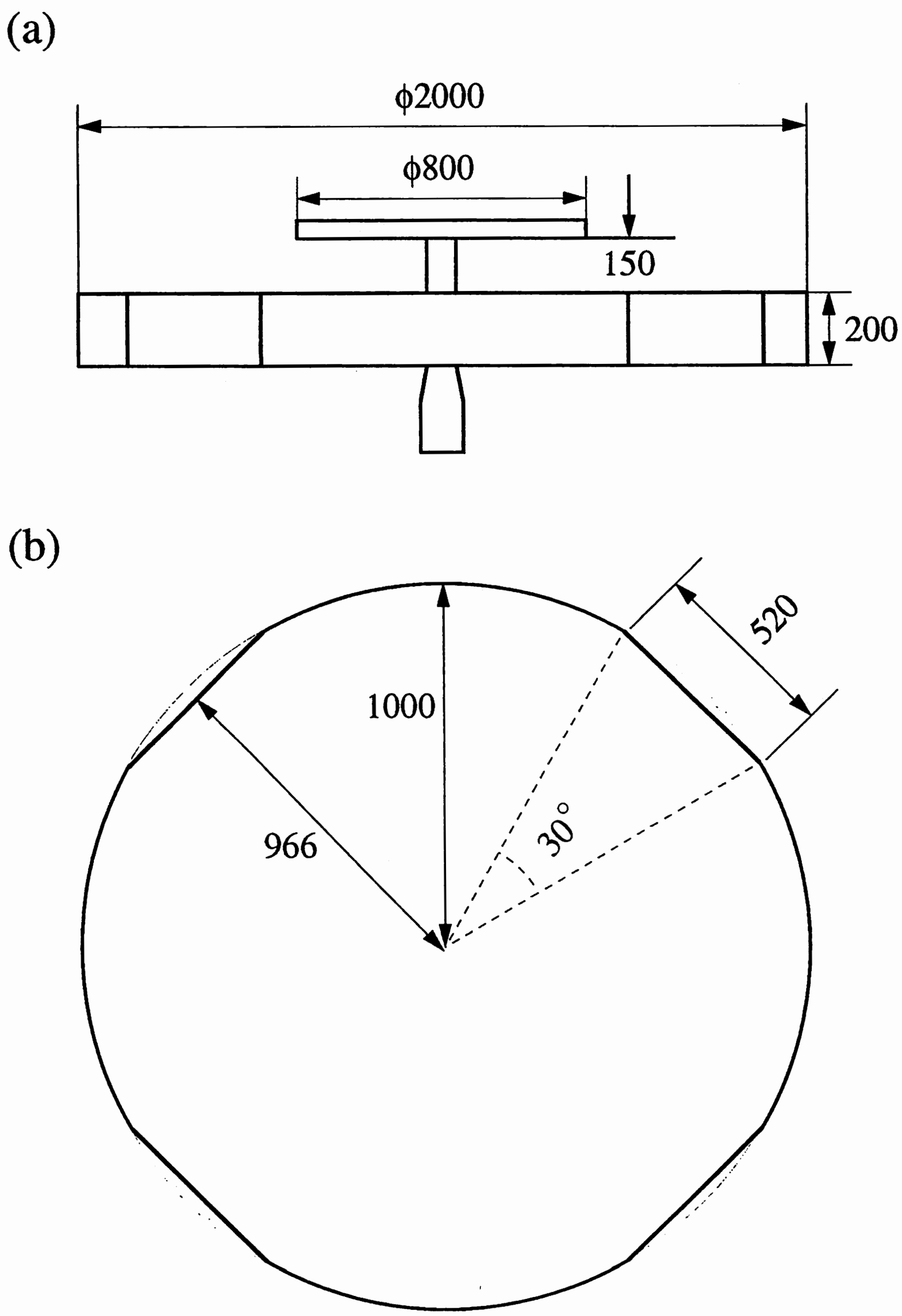

Figure 4.2: The disk antenna of ICRR: (a) a side view of the whole antenna with the support and the upper disk, and (b) a top view of the antenna proper. All dimensions in millimeters.

the isolation stacks use rubber blocks and a number of cables emit gas.

I describe briefly here the shape of the disk, the support rod, and the isolation stacks.

Shape of the Disk

The external form of ICRR disk is not an exact circle. Small parts of the edge of the disk have been cut off (see Fig. 4.2), to adjust the mode frequencies as explained below.

A disk has two fundamental quadrupole modes, the + mode and × mode, which are normally degenerate. The vibration mode patterns match well the two polarizations of gravitational waves. In the usual numbering they are the (2,1,1) and (2,1,2) modes. If the circumference of the disk is a true circle, the eigenfrequencies of these modes are the same. The modes of the actual disk are split in frequency, because of density inhomogeneity caused by the manufacturing process of the alloy, slight departures of the disk from a perfect circle, *etc.*, so that the physical parameters of the disk are not uniform. Although the eigenfrequencies of the modes of a nearly circular disk would be different, the difference would be only very slight, which depends on the shape of the disk, so that one could not easily separate and identify the vibration mode patterns. Thus, in order to split the degeneracy and eigenfrequencies of the modes clearly, the disk is truncated. In this case, the vibration mode patterns are fixed relative to the truncations so that one can specify the mode which the transducer monitors. The method for calculating the quadrupole mode eigenfrequencies of the truncated disk is shown below.

The calculated eigenfrequency of the (2,1,1) mode is 1195 Hz and the (2,1,2) mode 1186 Hz, but the monitored frequency of the (2,1,1) mode is in the range 1180 Hz to 1184 Hz. This is because the shape of the antenna is not exactly the same as that of the design, the antenna parameters used in the calculation differ from the actual ones, the density is not completely uniform, and the internal stress caused by the welding of the support, the lower and upper support with the upper disk, cause changes of elastic constants of the antenna. The frequency of the (2,1,2) mode cannot be measured because a monitoring system, *i.e.*, the transducer, is set so as to monitoring the (2,1,1) mode.

Nodal Support

The support rod is welded to the center of the disk. This support makes the disk largely immune to external vibration, since the center of the disk is a node for the quadrupole modes [51]. The support method of a disk is only this nodal support.

The mode Q of the ICRR disk is 3.2×10^5 at room temperature. Since Qs of disks are less than 10^6 [51], this is a normal value at room temperature, and it is apparent that the disk material has not been degraded by the welding.

Isolation Stacks

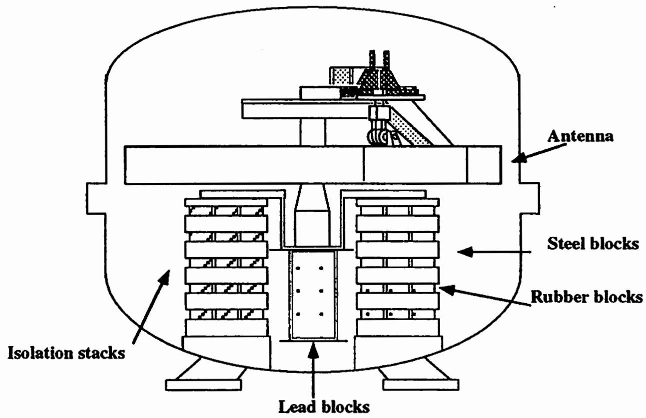

Figure 4.3: The isolation stacks: lead blocks lower the center of mass

The isolation stacks are intended to reduce seismic noise from the ground, which might excite the antenna at the monitored frequency, *i.e.*, the quadrupole mode resonant frequency of the disk which is excited by a gravitational wave.

The typical ground vibration caused by seismic noise is known empirically above 0.1 Hz to be

$$x_{\text{seismic}} \sim 10^{-7} \times \frac{1}{f^2} \, [\text{m}/\sqrt{\text{Hz}}], \tag{4.1}$$

where x_{seismic} is the displacement spectrum, and Eq.(4.1) is characteristic of the decreasing amplitude due to a f^{-2} law for the frequency range [52]: the example of the seismic noise measurement at Univ. of Tokyo, *etc.*, supports this f^{-2} dependency [53] .

The isolation stacks consist of 3 sets of the same stack which has five layers, each of alternate SS41 steel which is no-electrolytic plated with Ni and chloroprene rubber blocks. The isolation stacks were designed taking into account the desired reduction ratio for seismic noise and Euler's buckling force due to the supported mass [54].

Figure 4.3 shows the isolation stacks in the vacuum tank. It is assumed that one stack consists of a coupled oscillator with 5 stages, and each layer has a resonant frequency, f_0 corresonding to the spring constant of the rubber and mass of each oscillator. So the transfer function of the one layer is given by

$$T_{one-layer}(f) = \frac{i\frac{f_0}{Q}f + f^2}{-f^2 + i\frac{f_0}{Q}f + f_0^2}, \tag{4.2}$$

where Q is a quality factor.

Figure 4.4 shows the transfer fuction of the isolation stacks, when Q is assumed to be 10. When the stacks work as designed, the total isolation ratio at the antenna resonant frequency, 1.2 kHz, is expected to be above 10^{-13} and the displacement noise caused by seismic noise to be about 10^{-26} m/$\sqrt{\text{Hz}}$.

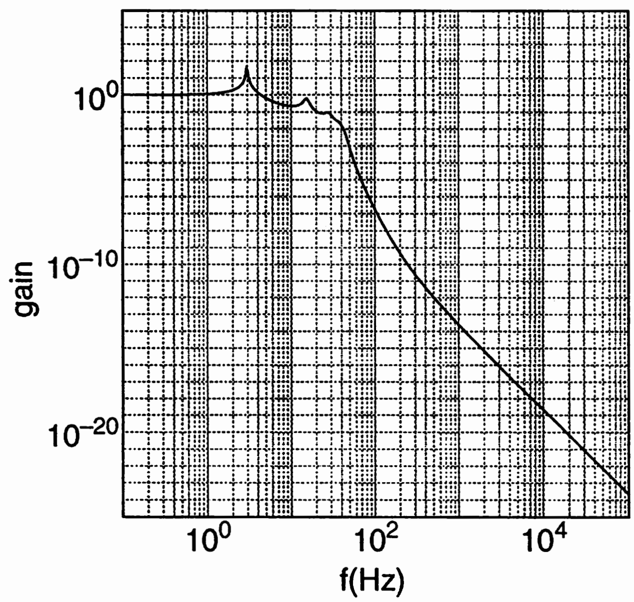

Figure 4.4: The calculated transfer function of the isolation stacks

Figure 4.5 compares the displacement of the edge of the antenna with the displacement of the ground at the detector site, and also shows the calculated displacement of the antenna due to the seismic noise. This was measured in air by a seisomometer (RION Co., Ltd.) which can work under 100 Hz with a sensitivity of 0.2 V/gal.

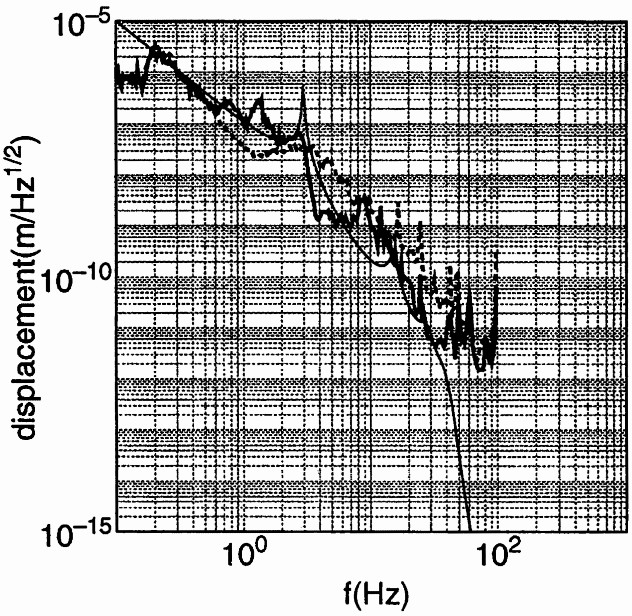

Figure 4.5: The displacement noise caused by seismic noise: measured by RION's seisomometer, the bold solid line corresponds to the noise on the stacks, the bold dashed line to that on the ground, and the thin solid line to the calculated seismic noise through the stacks.

As shown in Fig. 4.5, the isolation stacks work out very slightly for frequencies from several Hz to tens of Hz. There are some peaks at frequencies different from calculated ones. This is because the real spring constants of rubbers and the real quality factors of layers may be different from those used in calculation.

While we expect that the isolation power increases above 30 Hz (see Fig. 4.4), our measurement shows that isolation stacks do not screen the ground noise almost at all, at least up 100 Hz. The reason for the poor isolation above 30 Hz is made clear. The measurement in vacuum, *i.e.*, the measurement of the noise of the laser transducer gives the performance of the stacks, at least up to 100 Hz.

At lower frequencies near 1 Hz the isolation stacks have little effect, even amplifing the motion of the ground. They also cause some problems for the transducer. At the resonant frequencies of the isolation stacks, the slow swinging of the whole antenna makes it difficult to do feedback control of the transducer, and a change in temperature causes a inclination of the disk through expansion and contraction of the rubber blocks, and as a result changes the gain of the transducer. I discuss this problem further below.

4.2 Modes of the Disk's Elastic Motion

A free elastic disk has two degenerate quadrupole modes of vibrational motion interacting with gravitational waves. A in-plane vibrational motion of a disk had been already analyzed [41, 51, 55]. In this section, I present a mathematical derivation of the quadrupole modes, the reduced mass, and the effective area [40, 56] of the disk antenna, to understand the vibrational motion of the disk.

4.2.1 Normal Modes

We work in standard cylindrical coordinates (r, θ, z) aligned with the axis of the disk, which we take to have radius a, thickness h, density ρ, Poisson's ratio σ, and Young's modulus E, and we assume that stress tensors in the z direction are zero, *i.e.*, $\sigma_{rz} = \sigma_{\theta z} = \sigma_{zz} = 0$. We then expand the displacement vector of an arbitrary point on the disk $\vec{u} = (u_r, u_\theta)$, as a sum over modes:

$$u_r = U, \tag{4.3}$$

$$u_\theta = V, \tag{4.4}$$

$$U = \sum U_n \cos n\theta \cos \omega_n t, \tag{4.5}$$

$$V = \sum V_n \sin n\theta \cos \omega_n t. \tag{4.6}$$

The Lagrangian density of a small part $rdrd\theta dz$ is

$$\mathcal{L} = \frac{1}{2}\omega_n^2 \rho (U^2 + V^2) - \frac{1}{2}\sigma_{ik} u_{ik}. \tag{4.7}$$

Then Lagrangian of the whole disk is

$$\begin{aligned} L = \frac{Eh}{2(1-\sigma^2)} \int\!\!\int \Big\{ & k^2(U^2+V^2) - \left(\tfrac{\partial U}{\partial r} + \tfrac{1}{r}\tfrac{\partial V}{\partial \theta} + \tfrac{U}{r}\right)^2 \\ & + 2(1-\sigma)\tfrac{\partial U}{\partial r}\left(\tfrac{1}{r}\tfrac{\partial V}{\partial \theta} + \tfrac{U}{r}\right) \\ & - \tfrac{1-\sigma}{2}\left(\tfrac{1}{r}\tfrac{\partial U}{\partial \theta} + \tfrac{\partial V}{\partial r} - \tfrac{V}{r}\right)^2 \Big\} \, r dr d\theta, \end{aligned} \tag{4.8}$$

where k_n is the wave number, which is a function of the speed of sound v_s and the angular frequency of the nth mode:

$$k_n^2 = \frac{(1-\sigma^2)\omega_n^2 \rho}{E}, \tag{4.9}$$

$$v_s = \sqrt{\frac{E}{\rho(1-\sigma^2)}}. \tag{4.10}$$

Solving the Euler-Lagrange equations for U and V, we obtain

$$U_n = \frac{1}{kr}\left[A_n\left\{nJ_n(kr) - krJ_{n+1}(kr)\right\} + nB_nJ_n(k'r)\right], \tag{4.11}$$

$$V_n = -\frac{1}{kr}\left[nA_nJ_n(kr) + B_n\left\{nJ_n(k'r) - k'rJ_{n+1}(k'r)\right\}\right], \tag{4.12}$$

$$k'^2 = \left(\frac{2}{1-\sigma}\right)k^2, \tag{4.13}$$

where A_n and B_n are coefficients determined by boundary conditions for the stress tensors, and the J_n are Bessel functions.

Now we use integers n, m, and p to index the vibrational modes.

n :	symmetry in θ direction	$n = 0, 1, 2, \cdots$
m :	harmonic number	$m = 1, 2, 3, \cdots$
p :	polarization	$p = 1, 2$

The harmonic number m denotes the order of the root of the eigenequation to the nth mode; large m corresponds to a large frequency. Strictly k should be written k_{nmp}, which means the wave number of order m of the nth mode with polarization p.

The displacement vectors $(u^r_{np}, u^\theta_{np})$ can then be written

$$u^r_{np} = W^r_n(r)(\delta_{p1}\cos n\theta + \delta_{p2}\sin n\theta)\cos\omega_n t, \tag{4.14}$$

$$u^\theta_{np} = W^\theta_n(r)(\delta_{p1}\sin n\theta - \delta_{p2}\cos n\theta)\cos\omega_n t, \tag{4.15}$$

where

$$W^r_n(r) = \frac{1}{kr}\left[A_n\left\{nJ_n(kr) - krJ_{n+1}(kr)\right\} + nB_nJ_n(k'r)\right], \tag{4.16}$$

and

$$W^\theta_n(r) = -\frac{1}{kr}\left[nA_nJ_n(kr) + B_n\left\{nJ_n(k'r) - k'rJ_{n+1}(k'r)\right\}\right]. \tag{4.17}$$

Wave numbers of the modes are calculated by applying the boundary conditions of the stress tensors, specifically, at $r = a$, $\sigma^{rr} = \sigma^{r\theta} = 0$, and these determine the eigenfrequencies of the normal modes. The stress tensors σ^{rr}, $\sigma^{r\theta}$ can be also written

$$\sigma^{rr}_{np} = \chi^{rr}_n(r)(\delta_{p1}\cos n\theta + \delta_{p2}\sin n\theta)\cos\omega_n t, \tag{4.18}$$

$$\sigma^{r\theta}_{np} = \chi^{r\theta}_n(r)(\delta_{p1}\sin n\theta - \delta_{p2}\cos n\theta)\cos\omega_n t, \tag{4.19}$$

where

$$\chi_n^{rr}(r) = \frac{E}{(1+\sigma)r^2}\Bigg[A_n\Big[\Big\{n(n-1)-\frac{(k'r)^2}{2}\Big\}J_n(kr)+krJ_{n+1}(kr)\Big]$$
$$+nB_n\Big[(n-1)J_n(k'r)-k'rJ_{n+1}(k'r)\Big]\Bigg], \tag{4.20}$$

and

$$\chi_n^{r\theta}(r) = \frac{E}{(1+\sigma)r^2}\Bigg[nA_n\Big[(n-1)J_n(kr)-krJ_{n+1}(kr)\Big]$$
$$+B_n\Big[\Big\{n(n-1)-\frac{(k'r)^2}{2}\Big\}J_n(k'r)+k'rJ_{n+1}(k'r)\Big]\Bigg]. \tag{4.21}$$

From the above equations, the boundary conditions are given by

$$\begin{pmatrix} \chi_n^{rr}(a) \\ \chi_n^{r\theta}(a) \end{pmatrix} = \begin{pmatrix} & M & \end{pmatrix}\begin{pmatrix} A_n \\ B_n \end{pmatrix} = 0. \tag{4.22}$$

The wave numbers of the normal modes are obtained by solving the secular equation $\mid M \mid = 0$. Moreover, since B_n/A_n can be obtained from Eq.(4.22), we can determine the normal modes, and calculate the effective area and the reduced mass. Figure 4.6 shows some normal mode patterns for various (n, m, p). The (0,1,1), (2,1,1), (2,1,2), and (2,2,1) modes in Fig. 4.6 can be excited by a gravitational wave and the $n = 2$ modes are quadrupole modes. The eigenfrequencies of (2,1,1) and (2,1,2) mode are the lowest of all modes. The secular equation of the $n = 2$ modes is

$$\begin{vmatrix} \{2-\frac{(k'a)^2}{2}\}J_2(ka)+kaJ_3(ka) & 2\{J_2(k'a)-k'aJ_3(k'a)\} \\ 2\{J_2(ka)-kaJ_3(ka)\} & \{2-\frac{(k'a)^2}{2}\}J_2(k'a)+k'aJ_3(k'a) \end{vmatrix} = 0. \tag{4.23}$$

ICRR disk has four truncations (see Fig. 4.2) and its perimeter is not a circle, but its normal modes can be calculated by describing the shape in terms of a variable radius $a = a(\theta)$ and using a perturbation technique.

The perturbed radius of the disk is written (see Fig. 4.7)

$$a(\theta) = a_0 + \delta a(\theta), \tag{4.24}$$
$$\int_0^{2\pi} \delta a(\theta) d\theta = 0, \tag{4.25}$$

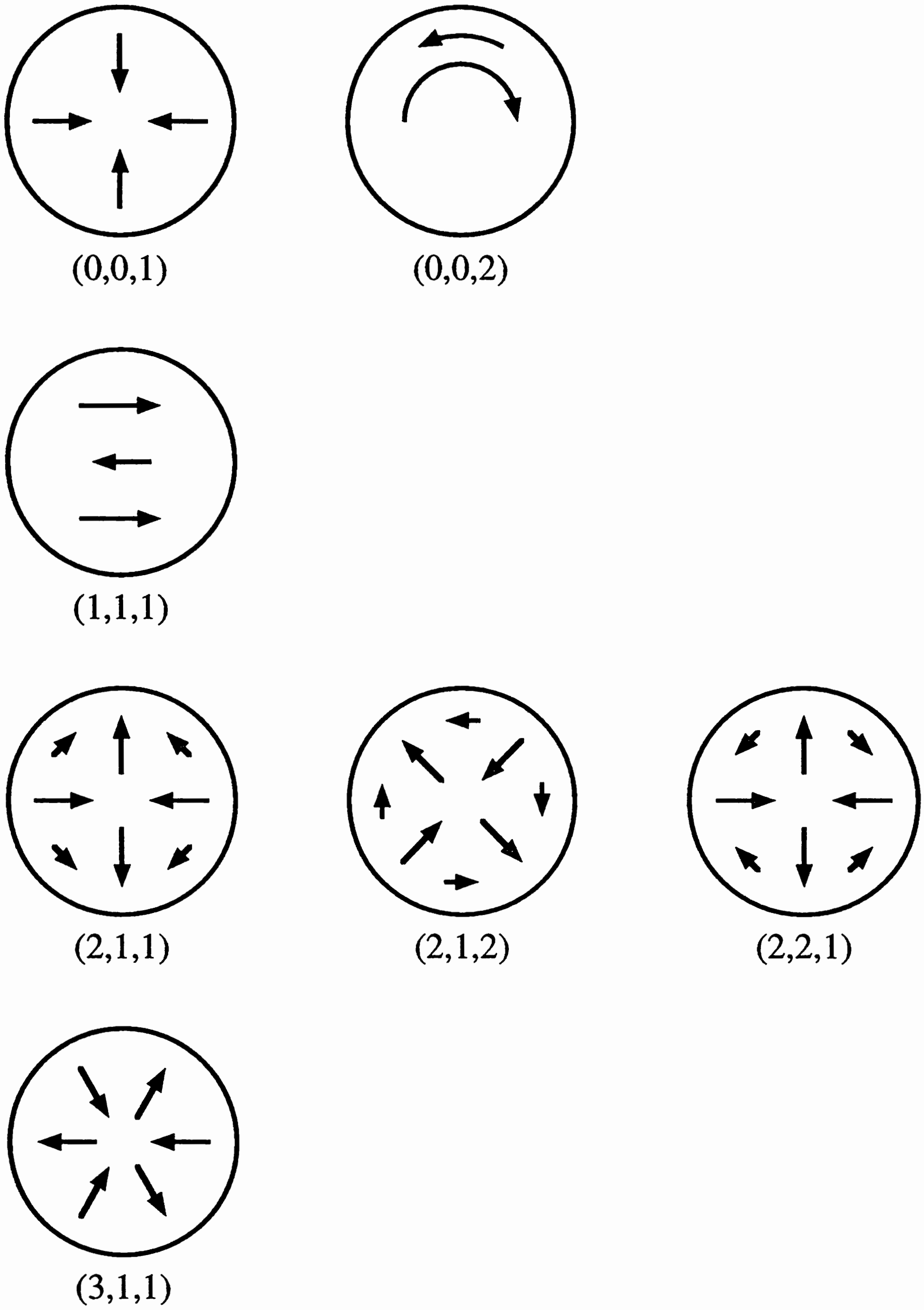

Figure 4.6: The mode patterns of the disk

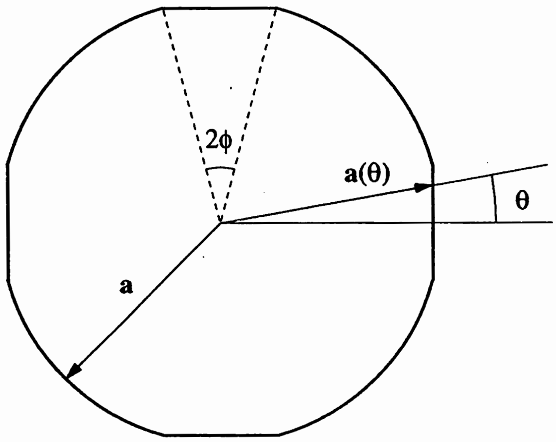

Figure 4.7: The definition of $a(\theta)$

where a_0 is an equivalent radius equal to the circumference divided by 2π and $\delta a(\theta)$ is the perturbation term, which depends on θ. Eq.(4.22) then becomes

$$\chi_{np}^{rr}(a_0 + (-1)^{p+1}\epsilon_n) = 0, \tag{4.26}$$
$$\chi_{np}^{r\theta}(a_0 + (-1)^{p}\ \epsilon_n) = 0, \tag{4.27}$$

where

$$\epsilon_n = \frac{1}{2\pi}\int_0^{2\pi} \delta a(\theta)\cos 2n\theta d\theta. \tag{4.28}$$

The wave numbers can be obtained from the secular equation by substituting $a_0 \pm \epsilon_2$ into a.

4.2.2 Effective Area and Reduced Mass

The effective area A_G and the reduced (or effective) mass μ_n are defined by

$$A_G = \frac{2\sum_{ij} q_{ij}^2}{\mu_n M}, \tag{4.29}$$

and

$$\mu_n = \int \rho\,|\vec{w}_n|^2\,dV. \tag{4.30}$$

A_G is a parameter of the antenna as a whole, unlike μ_n and q_{ij}. It does not depend on the way the general coordinate ξ_n is chosen[1].

In case of quadrupole mode ($n = 2$), the reduced mass is given by

$$\frac{\mu_2}{M} = \frac{1}{[W_2^r(a)]^2} \int_0^1 [(W_2^r(at))^2 + (W_2^\theta(at))^2] t dt, \tag{4.31}$$

and the quadrupole moment and the effective area corresponding to each polarization are given by

$$q_{ij} = \begin{cases} D \begin{pmatrix} 1 & 0 & 0 \\ 0 & -1 & 0 \\ 0 & 0 & 0 \end{pmatrix} & (p = 1) \\ D \begin{pmatrix} 0 & 1 & 0 \\ 1 & 0 & 0 \\ 0 & 0 & 0 \end{pmatrix} & (p = 2) \end{cases}, \tag{4.32}$$

$$\frac{A_G}{S} = \frac{4[\int_0^1 (W_2^r(at) - W_2^\theta(at)) t^2 dt]^2}{\pi \int_0^1 [(W_2^r(at))^2 + (W_2^\theta(at))^2] t dt}, \tag{4.33}$$

where

$$\frac{D}{M} = \frac{a}{W_2^r(a)} \int_0^1 [W_2^r(at) - W_2^\theta(at)] t^2 dt, \tag{4.34}$$

and S is the geometrical area of the disk.

4.2.3 Quadrupole Mode of ICRR Disk

In this section I derive the quadrupole mode of the ICRR disk antenna.

ICRR disk is 1 m in radius and 20 cm in thickness, and is made of an aluminum alloy 5052, with the following parameters:

$$\begin{cases} \text{density} & \rho & = & 2.64 & (\text{g/cm}^3) \\ \text{Poisson ratio} & \sigma & = & 0.33 & \\ \text{Young's modulus} & E & = & 7.03 \times 10^{10} & (\text{N/m}^{-2}) \end{cases}$$

The equivalent radius of the disk a_0 is obtained from the disk's circumference l:

$$\begin{aligned} l &= 2\pi a_0 \\ &= a(2\pi - 8\phi) + 4 \int_{-\phi}^{\phi} \frac{a \cos\phi}{\cos\theta} d\theta \\ &= a(2\pi - 8\phi) + 4a \cos\phi \log \frac{1 + \sin\phi}{1 - \sin\phi}, \end{aligned} \tag{4.35}$$

[1] As mentioned the previous section, the quadrupole moment q_{ij} indicating the degree of coupling between gravitational waves and the antenna is an important factor.

where $a(\theta)$ is the instantaneous radius and 2ϕ is the central angle of each truncated part of the disk, respectively. Calculating l for the disk gives $a_0 \approx 0.9924$ m, and Eq.(4.28) gives

$$\begin{aligned} \epsilon_2 &= \frac{1}{2\pi}\int_0^{2\pi}\{a(\theta)-a_0\}\cos 4\theta d\theta \\ &= \frac{2a}{\pi}\Big[2\cos\phi\int_0^{\phi}\frac{\cos 4\theta}{\cos\theta}d\theta - \frac{1}{2}\sin 4\phi\Big] \\ &\approx 6.8\times 10^{-4} \quad \text{m.} \end{aligned}$$

The wave number of the (2,1,1) mode is obtained by solving the secular equations, Eqs.(4.26) and (4.27):

$$\begin{pmatrix} \chi_{21}^{rr}(r_0+\epsilon_2) \\ \chi_{21}^{r\theta}(r_0-\epsilon_2) \end{pmatrix} = 0. \tag{4.36}$$

A numerical calculation gives $k = 1.374$ and this value corresponds to 1195 Hz.

These equations lead to B_n/A_n, from which one can calculate the reduced mass and the effective area. Table 4.1 shows the calculated quadrupole mode parameters.

Mode	Wave number	Frequency	Reduced mass	Effective area
(2,1,1) (+ mode)	1.374	1195.4 Hz	$0.518M$ (846 kg)	$0.564S$ (1.745 m^2)
(2,1,2) ($\times$ mode)	1.363	1185.8 Hz	$0.519M$ (848 kg)	$0.562S$ (1.739 m^2)

Table 4.1: The quadrupole mode parameters of ICRR disk

Chapter 5

A Laser Transducer

5.1 Principles of the Laser Transducer

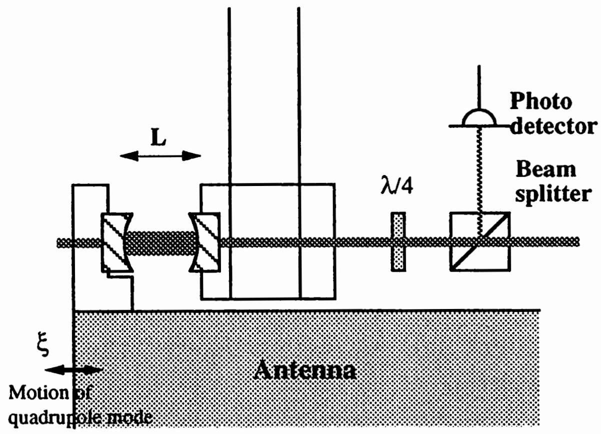

Figure 5.1: The sketch of the laser transducer

Figure 5.1 shows the conceptual sketch of the laser transducer which I have develoed. It consisits of a Fabry-Perot optical resonator (FP cavity) attached to the edge of the antenna. The FP cavity, used either in laser interferometers, comprises two mirrors with the high reflectivity. In the resonant condition, it outputs the phase change of the stored light in the cavity as the intensity change of the reflected light, which is a function of the frequency of light and the cavity length, with a high gain. Because the phase of the reflected light from the FP cavity changes drasticaly near the resonant condition. One mirror is attached to the antenna's edge so as to move with the vibrational motion of the antenna and the other is fixed independently, then the small displacement of the cavity length caused by the quadrupole motion of the antenna excited by a passing gravitational wave can be output at high gain by this transducer.

This laser transducer is one of active types using the parametric action, and can realizes a low noise characteristics, because it uses a laser beam, *i.e.*, photons as an external pumping source. The combination of mirrors with the high reflectivity and photons leads low loss at the signal transfomation and low back action to the antenna. In ideal case the laser transducer can detect the displacment of the cavity length up to the shot noise limit and realize the high sensitivity at room temperature. Since the actual FP cavity has the frequency noise, the intensity noise of the laser beam and the displacement noise of the cavity length originating from seismic noise, *etc.*, many problems must be solved to realize low noise.

I present a detailed mathematical derivation of the signal from the laser tansducer, *i.e.*, the Fabry-Perot cavity in section 5.2 and 5.3, and summarize briefly noises of the FP cavity in section 5.4.

5.2 Fabry-Perot Cavity

There is a good textbook which introduce the Fabry-Perot optical resonantor (FP cavity) in detail [57]. Here, the basic properties of the FP cavity are described.

5.2.1 Response of the Fabry-Perot Cavity

The response of FP cavity is characterized by the reflectivity and transmittance of the mirrors composing the cavity. Now we define the reflectivity and transmittance as shown in Fig. 5.2. Writing the incident light as $E_i(t) = E_0 e^{i\omega_0 t}$, the amplitudes of the transmitted and reflected light can be written

$$E_t(t) = \frac{t_1 t_2 e^{-i\omega_0 \frac{L}{c}}}{1 - r_1 r_2 e^{-i\omega_0 \frac{2L}{c}}} E_i(t). \tag{5.1}$$

and

$$E_r(t) = \left[r_1 - \frac{r_2 t_1^2 e^{-i\omega_0 \frac{2L}{c}}}{1 - r_1 r_2 e^{-i\omega_0 \frac{2L}{c}}} \right] E_i(t), \tag{5.2}$$

The transfer functions of the transmitted and reflected light to the incident light are defined as

$$a(\omega) = \frac{t_1 t_2 e^{-i\omega \frac{L}{c}}}{1 - r_1 r_2 e^{-i\omega \frac{2L}{c}}}, \tag{5.3}$$

$$b(\omega) = r_1 - \frac{r_2 t_1^2 e^{-i\omega \frac{2L}{c}}}{1 - r_1 r_2 e^{-i\omega \frac{2L}{c}}}. \tag{5.4}$$

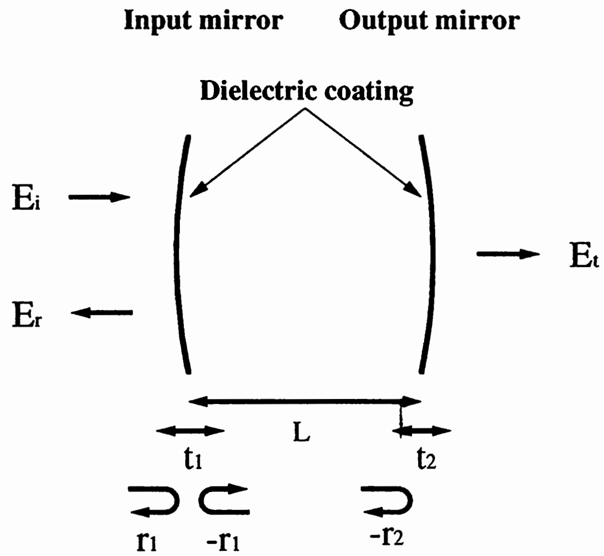

Figure 5.2: The schematic of the Fabry-Perot Cavity

Then the intensity of the transmitted and reflected light, I_t and I_r, are

$$I_t = |a(\omega)|^2 I_i \tag{5.5}$$

$$= \frac{(t_1 t_2)^2}{(1 - r_1 r_2)^2} \frac{1}{1 + \frac{4 r_1 r_2}{(1 - r_1 r_2)^2} \sin^2 \frac{\omega L}{c}} I_i, \tag{5.6}$$

$$I_r = |b(\omega)|^2 I_i \tag{5.7}$$

$$= \frac{\frac{\left\{r_1 - r_2(r_1^2 + t_1^2)\right\}^2}{(1 - r_1 r_2)^2} + \frac{4 r_1 r_2}{(1 - r_1 r_2)^2}(r_1^2 + t_1^2)\sin^2 \frac{\omega L}{c}}{1 + \frac{4 r_1 r_2}{(1 - r_1 r_2)^2}\sin^2 \frac{\omega l}{c}}. \tag{5.8}$$

These are periodical function of ω, the frequency interval for satisfying the resonant condition, $\sin(\omega L/c) = 0$, is called the free spectral range (FSR),

$$\frac{\omega_{\mathrm{FSR}} L}{c} = \pi \quad \longrightarrow \quad \nu_{\mathrm{FSR}} = \frac{c}{2L}. \tag{5.9}$$

When the reflectivity nearly equals 1, $|a(\omega)|^2$ and $|b(\omega)|^2$ have peaks at the interval of ν_{FSR}. The full width of half maximum (FWHM) of these peaks is defined as $\Delta\nu_{\mathrm{FWHM}}$, and the important parameter, the finesse $\mathcal{F}$, which is the ratio of the FSR to the FWHM, is obtained by

$$\mathcal{F} = \frac{\nu_{\mathrm{FSR}}}{\Delta\nu_{\mathrm{FWHM}}}$$

$$= \frac{\pi\sqrt{r_1 r_2}}{1 - r_1 r_2}. \tag{5.10}$$

$\mathcal{F}$ is related with the qulaity value of the cavity Q

$$Q = \omega\frac{\tau_s}{2} = \omega\left(\frac{L\mathcal{F}}{\pi c}\right) = \frac{2L\mathcal{F}}{\lambda}, \tag{5.11}$$

where τ_s is the storage time. The intensity of the reflected and transmitted light turn $1/e$ and $1/e^2$, respectively. $\mathcal{F}$ is the quantity corresponding to the reflection number in the cavity.

Similary, we can define the FSR and the FWHM as the function of L, L_{FSR} and ΔL_{FWHM},

$$L_{\mathrm{FSR}} = \frac{c}{2\omega}, \tag{5.12}$$

$$\Delta L_{\mathrm{FWHM}} = \frac{1 - r_1 r_2}{\sqrt{r_1 r_2}}\frac{c}{\omega}. \tag{5.13}$$

5.2.2 Hermite-Gaussian Mode

In the prevous subsection, we treated the laser beam using geometrical optics. In reality, the laser beam propagates divergently due to its diffraction. Hence, the mirrors of the cavity must be so as to match the wavefront of the laser beam.If a FP cavity is formed by concave mirrors, the modes in the cavity take Hermite-Gaussian forms

$$\psi_{lm} = \frac{w_0}{w(z)}H_l\left(\frac{\sqrt{2}x}{w(z)}\right)H_m\left(\frac{\sqrt{2}y}{w(z)}\right)\exp\left[-\frac{x^2+y^2}{w^2(z)} - ik\frac{x^2+y^2}{2R(z)} - ikz + i(l+m+1)\eta\right], \tag{5.14}$$

where $w(z)$, $R(z)$, and η are the beam radius with $1/\mathrm{e}^2$ of the peak intensity, the curvature radius of the wavefront, and the guoy phase, respectively, as functions of z, given by

$$w(z) = w_0\sqrt{1 + \left(\frac{\lambda z}{\pi w_0^2}\right)^2}, \tag{5.15}$$

$$R(z) = z\left[1 + \left(\frac{\pi w_0^2}{\lambda z}\right)^2\right], \tag{5.16}$$

$$\eta(z) = \arctan\left(\frac{\lambda z}{\pi w_0^2}\right), \tag{5.17}$$

and H_l and z denote the l th Hermite poynominal and the coordinate in the direction of the beam propagating axis, respectively, and $w_0 = w(0)$. Another feature is the dependence of the phase variation the order of the mode, $l+m$; this dependence leads to a difference of the resonant frequency for the higher modes.

Since the Hermite-Gaussian modes form a complete system, the normalized incident beam can be expanded in terms of the cavity modes as

$$\psi_i = \sum_{l,m} c_{lm}\psi_{lm}. \tag{5.18}$$

Stability of the resonant modes is determined by cavity length L and curvature radius of mirrors. For a cavity consisiting of mirrors with curvature radii of R_1 and R_2, the modes of the cavity are stable when

$$0 \leq g_1 g_2 \leq 1, \tag{5.19}$$

where

$$g_{1,2} = 1 - \frac{L}{R_{1,2}}. \tag{5.20}$$

In this case, the resonant frequencies of the Hermite-Gaussian modes are given by

$$\nu_{lm} = \frac{c}{2L}\left[n + (l+m+1)\gamma\right], \tag{5.21}$$

$$\gamma = \frac{1}{\pi}\arccos\sqrt{g_1 g_2}, \tag{5.22}$$

where n is an integer related to the number of the standing waves in the cavity. The modes characterized by n are called longitudinal modes, its frequency interval being ν_{FSR}, while those characterized by l and m are called transverse modes, its frequency interval $\gamma\nu_{\mathrm{FSR}}$.

5.2.3 Mode Matching

The resonant condition of the FP cavity is

$$\exp\left[-i\omega\frac{2L}{c}\right] = 1. \tag{5.23}$$

Pound-Drever method [58] uses the resonant condition and locks the mode of the laser beam in the FP cavity into TEM_{00}.

When an incident beam, ψ_i, has higher modes, it can be expanded by the modes of the FP cavity, a ratio of the matching for the TEM_{00} mode is given by a matching coefficient M,

$$M = \int\int \psi_i \psi_{00}\, dx dy. \tag{5.24}$$

When the incident beam has only a fundamental mode, M=1. Larger M is, a higher sensitivity the FP cavity has.

Since the incident beam without TEM_{00} mode is reflected at the front mirror of the FP cavity (the mirror of the incident side), detected with the signal light, and then decreases the signal-to noise ratio of the signal from the FP cavity. The optical elements must be positioned as possible as $M = 1$, and higher modes should be reduced in the incident beam as possible.

About the modes of the cavity and its optical matching condition, see Ref. [59] in detail.

5.3 Signals from the Fabry-Perot Cavity

The resonant condition of the FP cavity is met by Pound-Drever method [58]. This is a method of siganl detection using *rf* modulation, and measures the phase change of the light in the FP cavity near the resonance as the error signal, which is obtained by demodulating the reflected light from the FP cavity and in turn is fed back to make the resonant condition.

5.3.1 Detection of the displacement by Phase-Modulated Light

5.3.2 Phase Noise (Frequency Fluctuation)

In what follows we discuss the response of the FP cavity for the phase-modulated incident light, when a laser light has phase noise.

If the phase noise $\phi(t)$is mixed in a phase-modulated light with a modulation frequency ω_m and a modulation index m, the incident light to the FP cavity is

$$E_i(t) = E_0 \exp\Big[i(\omega_0 t + m \sin \omega_m t + \phi(t))\Big]. \tag{5.25}$$

If $\phi(t)$ is written

$$\phi(t) = \phi_F e^{i\omega_F t} + \phi_F^* e^{-i\omega_F t}, \tag{5.26}$$

the incident light is

$$E_i(t) = E_0 e^{i\omega_0 t} \sum_{n=-\infty}^{\infty} J_n(m) e^{in\omega_m t}(1 + i\phi_F e^{i\omega_F t} + i\phi_F^* e^{-i\omega_F t}), \tag{5.27}$$

where $\phi_F \ll 1$. Assuming $m \leq 1$, we obtain

$$\begin{aligned} \frac{E_r(t)}{E_0 e^{i\omega t}} &= J_0(m)\left[b(0) + i\phi_F b(\omega_F) e^{i\omega_F t} + i\phi_F^* b(-\omega_F) e^{-i\omega_F t}\right] \\ &\quad + 2iJ_1(m) \sin \omega_F t \left[1 + i\phi_F e^{\omega_F t} + i\phi_F^* e^{-i\omega_F t}\right]. \end{aligned} \tag{5.28}$$

Neglecting second and higher order of ϕ_F ($|\phi_F| \ll 1$), the intensity of the reflected light is given by

$$\frac{I_r(t)}{I_0} = \frac{I_r{}^{(0)}}{I_0} + \frac{I_r{}^{(1)}}{I_0}\sin\omega_m t + \frac{I_r{}^{(2)}}{I_0}\cos 2\omega_m t, \tag{5.29}$$

$$\frac{I_r{}^{(0)}}{I_0} = J_0^2(m)b^2(0) + 2J_1^2(m), \tag{5.30}$$

$$\frac{I_r{}^{(1)}}{I_0} = 4J_0(m)J_1(m)\left[\phi_F\Big\{b(\omega_F) - b(0)\Big\}e^{i\omega_F t} + \phi_F^*\Big\{b(-\omega_F) - b(0)\Big\}e^{-i\omega_F t}\right], \tag{5.31}$$

$$\frac{I_r{}^{(2)}}{I_0} = -2J_1^2(m), \tag{5.32}$$

where $I_0 = |E_0 e^{i\omega_0 t}|^2$. The reflected light demodulated by $\sin\omega_m t$ becomes the error signal which gives the difference between the frequency of the incident light and the resonant frequency of the FP cavity. The feed back to the laser by this signal make it possible to stabilize the frequency of the laser.

If the higher transverse modes do not exit, let us evaluate the actual error signal

$$I_r{}^{(1)} = \frac{8ct_1^2}{L\Delta\omega_c^2}J_0(m)J_1(m)I_0\dot{\phi}\left(t + \frac{\theta_F}{\omega_F}\right)\left[1 + \left(\frac{2\omega_F}{\Delta\omega_c}\right)^2\right]^{-1/2}, \tag{5.33}$$

where

$$\dot{\phi}(t) = \omega_F\phi\left(t + \frac{\pi}{2\omega_F}\right). \tag{5.34}$$

If $\omega_F \ll \Delta\omega_{\mathrm{FWHM}}$, Eq.(5.33) turns to

$$I_r{}^{(1)} = \frac{8ct_1^2}{L\Delta\omega_c^2}J_0(m)J_1(m)I_0\dot{\phi}(t), \tag{5.35}$$

$I_r^{(1)}$ is proprtional to the frequency noise. On the other hand, if $\omega_F \gg \Delta\omega_{\mathrm{FWHM}}$,

$$I_r{}^{(1)} = \frac{4ct_1^2}{L\Delta\omega_c}J_0(m)J_1(m)I_0\phi(t), \tag{5.36}$$

$I_r^{(1)}$ is proportional to the phase noise.

5.3.3 Detection of the Displacement of the Cavity Length

Now considering the frequency-stabilized laser beam, the incident light to the FP cavity is

$$\begin{aligned} E_i(t) &= E_0 e^{i(\omega_0 t + m\sin\omega_m t)} \\ &= E_0 \sum_{n=-\infty}^{\infty} J_n(m)e^{i(\omega_0 + n\omega_m)t}, \end{aligned}$$

then the refelcted light is given by

$$E_r(t) = E_0 e^{i\omega_0 t} \sum_{n=-\infty}^{\infty} J_n(m) b(\theta_0 + n\theta_m) e^{in\omega_m t}, \tag{5.37}$$

where $\theta \equiv \omega L/c$. The small displacement of the cavity length δL causes

$$L = L_0 + \delta L \longrightarrow \theta = \theta_0 + \delta\theta.$$

Since $\omega_m \delta L/c \ll 1$, we obtain

$$\begin{aligned} E_r(t) &= E_0 e^{i\omega_0 t} \left[J_0(m) b(\delta\theta) \right. \\ &\quad \left. + J_1(m) \left\{ b(\theta_m + \delta\theta) e^{i\omega_m t} - b(-\theta_m + \delta\theta) e^{-i\omega_m t} \right\} \right]. \end{aligned} \tag{5.38}$$

The first-order Taylor expansion gives

$$\begin{aligned} b(\delta\theta) &\cong b(0) + \delta\theta \left. \frac{\partial b}{\partial \theta} \right|_{\theta=0} \\ &= r_1 - t_1^2 \sqrt{\frac{r_2}{r_1}} \frac{\mathcal{F}}{\pi} + 2i \frac{t_1^2}{r_1} \left(\frac{\mathcal{F}}{\pi} \right)^2 \delta\theta \\ &\equiv b(0) + i\beta_0 \delta\theta, \end{aligned} \tag{5.39}$$

$$\begin{aligned} b(\theta_m + \delta\theta) &\cong b(\theta_m) + \delta\theta \left. \frac{\partial b}{\partial \theta} \right|_{\theta=\theta_m} \\ &= r_1 - \frac{r_2 t_1^2 e^{-2i\theta_m}}{1 - r_1 r_2 e^{-2i\theta_m}} + i \frac{2 r_2 t_1^2 e^{-2i\theta_m}}{(1 - r_1 r_2 e^{-2i\theta_m})^2} \delta\theta \\ &\equiv b(\theta_m) + i\beta_m \delta\theta, \end{aligned} \tag{5.40}$$

$$\begin{aligned} \frac{E_r(t)}{E_0 e^{i\omega_0 t}} &\cong J_0(m) \{ b(0) + i\beta_0 \delta\theta \} \\ &\quad + J_1(m) \left[\left\{ b(\theta_m) + i\beta_m \delta\theta \right\} e^{i\omega_m t} - \left\{ b^*(\theta_m) + i\beta_m^* \delta\theta \right\} e^{-i\omega_m t} \right] \\ &= J_0(m) \{ b(0) + i\beta_0 \delta\theta \} \\ &\quad + 2J_1(m) \left[iIm[b(\theta_m) e^{i\omega_m t}] - Im[\beta_m e^{i\omega_m t}] \delta\theta \right]. \end{aligned} \tag{5.41}$$

The intensity of the reflected light is

$$\begin{aligned} \frac{I_r}{I_0} &= J_0^2(m) b^2(0) + 2J_1^2(m) \left\{ |b(\theta_m)|^2 - Re[b^2(\theta_m) e^{2i\omega_m t}] \right\} \\ &\quad - 4J_0(m) J_1(m) \left\{ b(0) Im[\beta_m e^{i\omega_m t}] - \beta_0 Im[b(\theta_m) e^{i\omega_m t}] \right\} \delta\theta. \end{aligned} \tag{5.42}$$

For the ideal FP cavity ($b(0) = 0$), we obtain

$$I_r^{(1)} = 4J_0(m)J_1(m)\beta_0 Im\left[b(\theta_m)e^{i\omega_m t}\right]\delta\theta. \tag{5.43}$$

Also, $\omega_m \tau_s \ll 1$ gives $b(\theta_m) \cong b(0) + i\beta_0\theta_m$, then

$$I_r^{(1)} = 16J_0(m)J_1(m)\frac{t_1^4}{r_1^4 r_2^2}\left(\frac{\mathcal{F}}{\pi}\right)^4 \theta_m\delta\theta. \tag{5.44}$$

However in case of the FP cavity with its length of 10 mm and a modulation frequency of 15 MHz as our transducer (see Table 6.1), the above condition is not satisfied, and the modulated frequency componet in the reflected light decreases, and then the detection efficiency becomes worse.

5.4 Noises of the Fabry-Perot cavity

Let us discuss noise sources in the Fabry-Perot interfeometer, in this section.

Shot Noise

A best known noise of the interferometer is shot noise. This noise results from the random nature of the photon arrival times at the photodetector, and a fundamental limit on the sensitivity of the interferometer.

The photon shot noise is connected with the detected photocurrent, I_{dc}, and is white with a frequency independent amplitude

$$\sqrt{2eI_{dc}}, \tag{5.45}$$

where e is an elementary charge and the units are $\mathrm{A}/\sqrt{\mathrm{Hz}}$. The signal to noise ratio of the detectable gravitational waves to the shot noise determines the sensitivity of the interferometer.

The shot noise of an ideal FP cavity with a short cavity length is given by

$$x_{shot} = \frac{1}{4\mathcal{F}}\sqrt{\frac{\pi\hbar c\lambda}{\eta P}}, \tag{5.46}$$

where $\mathcal{F}$, λ, η, and P are finesse of the FP cavity, wavelength of the laser light, quantum efficiency of the photodetector, and the power of the incident light, respectively. In this case, it is assumed that the moduation index m of the phase modulation is $m \ll 1$.

The shot noise level can be improved by increasing the incident laser power because the signal to noise ratio for the shot noise decreases with the square root of the laser power.

Frequency Noise of the Laser

The frequency fluctuation of the laser is another major source.

For the FP cavity, the frequency fluctuations directly affect the signal. The response function of the FP cavity indicates that changes of the cavity length and the frequency of the laser light cause a relative phase difference obeying $\omega L/c$. In briefly, the displacement noise and the frequency noise in the FP cavity are equivalent, and the relation between both is written

$$\frac{\Delta\nu_n}{\nu} = \frac{\Delta L}{L}, \tag{5.47}$$

where $\Delta\nu_n$ and ν are the frequency noise and the frequency of the laser light, respectively, and ΔL is the displacement of the cavity length L.

In order to acheive the sensitivity of the shot noise level for the FP cavity, the phase fluctuation caused by the laser frequency noise must be reduced below the shot noise level. Present technique can well-stabilize the frequency noise of the laser.

Intensity Noise of the Laser

$\Delta P/P$, where ΔP is the intensity fluctuation of the laser power and P is the stationary power of the laser, contributes to the signal of the FP cavity as the intensity noise. When the perfect locking of the FP cavity at resonance and the ideal phase modulation are realized, the intesnsity noise contributes to the signal by only a second order. Any imperfections increases an intensity noise.

Normally, since the modulation frequency of the laser light is sufficiently higher, *i.e.*, is in rf frequency band, the intensity noise is less than the shot noise level. The incompleteness of the ideal locking point due to the seismic noise, the frequency noise, and *etc.*, couples the intensity noise to the displacement signal. The original intensity noise of the laser, $\Delta P/P$, is connected with a corresponding displacement noise, given by

$$\Delta L_{intensity-noise} = \frac{\Delta P}{P}\delta L, \tag{5.48}$$

where δL is a residual fluctuation between the perfect and the real locking point.

Beam Jitter Noise

The laser beam geometry, including the beam direction and the beam shape, fluctuates due to the instability of the laser cavity, the vibration of the optical elements, *etc.* Such beam jitter is equivalent to the fluctuation of the contribution of the higher transverse modes. The most significant contributions to such jitter are the first and second order transverse modes. [60].

One method to suppress the beam jitter noise is an optical fiber which keeps a Gaussian distribution and passes only a fundamental mode corresponding to TEM_{00} mode of the FP cavity. Higher order transverse modes caused by beam jitter cannot pass through such an optical fiber. If the output edge of the fiber, which is located in vacuum in most case of gravitational experiments, is isolated by some isolation system, the output beam from the fiber would not have beam jitter. However, the optical fiber has some disadvantages: the loss of the input power by transmission efficiency and the power limitation of the fiber, which can transmit.

The other is a mode cleaner [35] which works as a mode selector and a frequency stabilization system. A typical mode cleaner consists of a FP cavity which has a couple of suspended mirrors. Large scale interferometers equippes mode cleaners.

Other Noises

There are other noise sources of the interferometer: radiation pressure noise, noise caused by the residual gas, and *etc.*. There are good reviews about noises of the inteferometers [2, 61].

Chapter 6

Design for the Laser Transducer

In this chapter I present the design of the resonant mass detector in ICRR, especially the design of the laser transducer, a prototype transducer, which consists of a single pendulum, and an improved transducer, which comprises a double pendulum, and the frequency stabilization system.

6.1 Optical Design and Elements

The fundamental optical design of the resonant mass detector is shown as follows.

The whole system comprises the resonant mass antenna which is explained in chapter 4, the laser transducer attached to the antenna, and the laser frequency stabilization system. Figure 6.1 shows the scheme of the detector.

Nd:YAG Laser

A laser source, 1 in Fig. 6.1, is a solid-state diode-pumped Nd:YAG ring laser. This is a model 124 of LIGHTWAVE Inc., consisting of a monolithic non-planar ring resonator wihch is thermally controlled and is tunable in frequency using an attached piezoelectric, generates a continuous 50 mW infrared laser beam with a wavelength of 1.064 μm (an oscillation frequency $\cong$ 2.92 THz) in specificatons, actually 58 mW, which is measured by a power meter (TQ8210, ADVANTEST Corp.).

The laser head is fixed on an alminum block working as a heat sink. The control unit of the laser head has threee input BNC conectors: A SLOW FREQUENCY BNC, voltage applied to the SLOW BNC tunes the laser resonator by heating or cooling the laser crystal resonator. Tuning is due to thermally induced effects: a physical expansion of the laser resonator and a change in the index of refraction. This allows to control the laser oscillation frequency with a relatively slow time constant (approximately 1 $\sim$ 10 seconds). The tuning coefficient is about 3.1 GHz/°C.

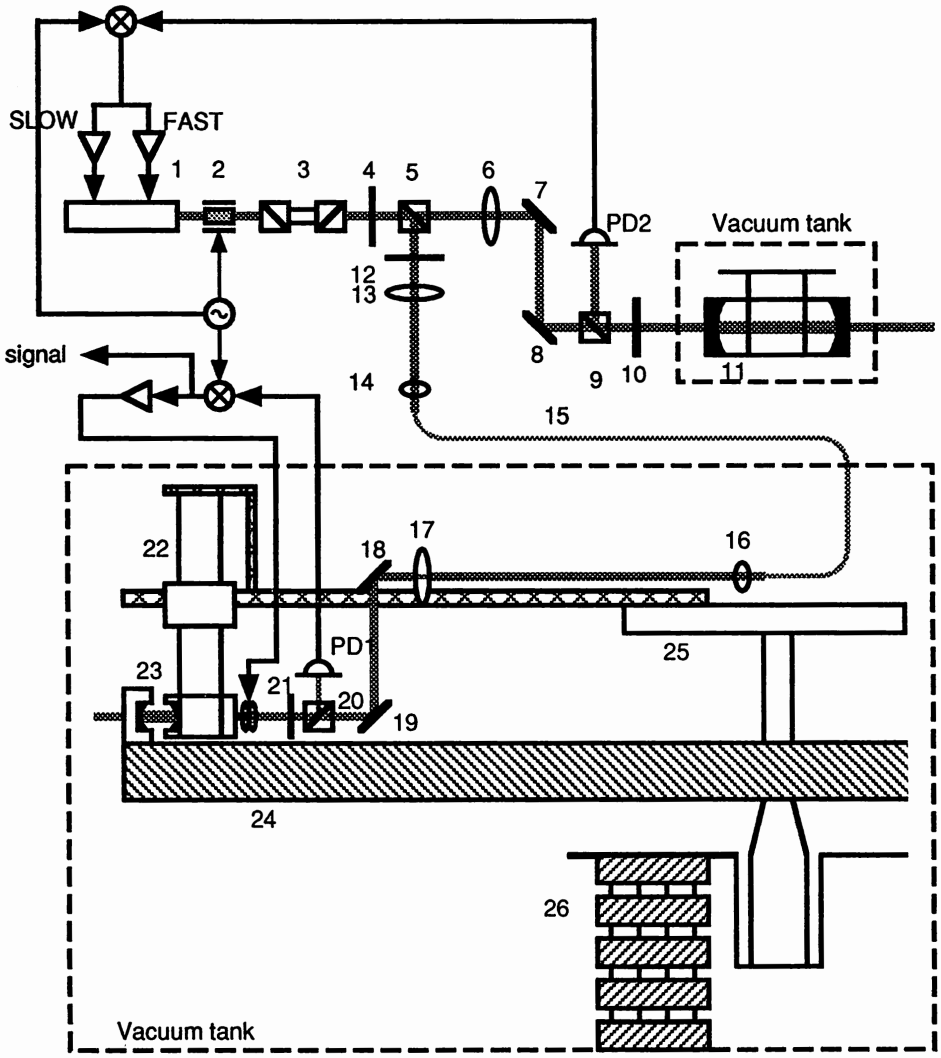

1:Nd:YAG Laser(50mW),2:Phase modulator,3:Isolator,4,12: λ/2,5,9,20:PBS,
6,13,17:Mode matching lens,7:8:Alignment mirror,10,21: λ/4,
11:Frequency stabilization cavity,14,16:Lens of Fiber coupler,
15:Polarization maintaining single-mode fiber,
18,19:Alignment mirror(Motorized),22:Double pendulum,23:FP TRD,
24:Resonant antenna,25:Upper disk,26:Isolation stacks,
PD1:Photodetector of Transducer,
PD2:Photodetector for Frequency stabilization

Figure 6.1: The schematic of the optical system

A FAST FREQUENCY BNC, voltage applied to the FAST BNC contracts a piezoelectric bonded to the laser crystal. This voltage results in a strain sufficeint to vary the frequency by tens of MHz at modulation rates up to 100 kHz. These SLOW and FAST FREQUENCY BNC are used for the frequency stabilization, discussed in detail below.

AN OUTPUT SUPPRESS BNC, by applying a voltage to the SUPRESS BNC the laser diode current can be controlled. With no voltage applied to the SUPPRESS BNC the diode pump is at its rated maximum. The laser is operated at this standard condition.

EOM

A electro-optical modulator (EOM), 2 in Fig. 6.1, phase-modulates the laser light in order to lock the FP cavity on resonance. Our EOM is a Model 4003 producted by NewFocus Inc. The principle of the phase-modulation is explained in detail in Ref. [57]. The phase-modulation frequency should be normally set at a frequency higher than 10 MHz. Because the intensity noise performance of the laser light in such rf field is below the shot noise level. The phase-modulation at rf frequencies is realized by the EOM. The EOM is drived by a circuit using a high-power operational amplifier WB05 (APPEX Inc.), see Appendix A.

Optical Fiber

The laser light through a Faraday isolater, 3 in Fig. 6.1, (NewFocus Inc.) has 50 mW in power, then the beam is divided into the laser transducer and the frequency stabilization of the laser; 40 mW is used for the incident light into the laser transducer in the vacuum tank through a polarization preserving single mode optical fiber (Radiant Communications Corp. FS-HB-5651), 15 in Fig. 6.1, and the remainder 10 mW for the frequency stabilization FP cavity. The power transmittance of the optical fiber is about 70 % constantly.

Optical fibers are circular dielctric waveguides which can transport optical energy and information. They have a central core surrounded by a concentric cladding with slightly lower (by≅1%) refractive index. Our polarization preserving single mode optical fiber has been produced with the V-number<2.405 and a strong intrinsic birefringence, and can transmit the lowest mode of the Hermite-Gaussian beam with the liner polarization [62, 63].

The V-number is defined generally as

$$V = \frac{2\pi}{\lambda} a\, \mathrm{NA}, \tag{6.1}$$

where λ is the wavelength of the laser beam in vacuum, a is the radius of a fiber core, and NA is the numerical aperture of a fiber. Our fiber has 3.2 μm in radius of the fiber core and 0.13 in NA. When V¡2.405, the fiber can propagate only the lowest LP_{01} mode in weakly guiding approximation, *i.e.*, the HE_{11} mode, which matches to the TEM_{00} mode of the

FP cavity. The mode profile of the LP_{01} mode in the fiber is approximated by Gaussian distribution:

$$w = a\left(0.65 + \frac{1.619}{V^{1.5}} + \frac{2.879}{V^{6}}\right), \tag{6.2}$$

where w is the width at which the intensity becomes $1/e^2$.

A fiber with the strong birefringence have a well-defined principal axis to maintain the propagating polarization even when the fiber is bent or twisted. A small birefringence causes the two polarization components to propagate at different phase velocites. As a result, the net polarization state of the output beam varies with fiber length and changes as the fiber is bent or twisted.

The fiber is led into the vacuum tank through the hole of a small flange for the fiber, and wired from the fiber coupler of the incident edge, 14 in Fig. 6.1, to the coupler of the output edge, 16, in the vacuum tank. The total length of the fiber is about 10 m. From the incident coupler to the flange for the fiber, the fiber is guided through a vinyl pipe with 3 mm in diameter in a hard plastic pipe with 5 cm in diameter for protection. The fiber coupler of the output edge is fixed at the place where the mode of the tansmitted light is matched to the mode of the FP cavity of the laser transducer.

The incident edge of the fiber is cut by a fiber cleaving tool with a diamond cutter (F-BK2, NEWPORT Corp.) in order to make a smooth section. Because the smooth section increases the incident efficiency of the laser beam.

The fiber coupler positions the incident edge of the fiber to an adequate place determined by the waist radius of the incident Gaussian beam, matching lenses, and the radius of the core and NA of the fiber. Good coupling efficieny requires a precise positioning of the fiber to center the core in the focused beam spot, *i.e.*, to maximize coupling efficiency into the single-mode fiber, we must match the incident field distibution to that of the fiber mode. The position of the fiber and the radius of the focused spot of the beam can be obtained by calculating the coupling to the fiber through a focusing lens system [64].

If two lenses, 13 and 14 in Fig. 6.1 in order to match the laser beam into the fiber, forms the confocal system, *i.e.*, $d_0 = f_1$, $d_1 = f_1 + f_2$, and $d_2 = f_2$, where d_0, d_1, and d_2 are intervals between the position at the beam waist of the incident beam and a first lens, *i.e.*, 13 in Fig. 6.1, betwen the first lens 13 and the second lens 14 in the fiber coupler, and between the second lens 14 and the focused position, respectively, and f_1 and f_2 are focal lengths of the first and second lenses, respectively, the focused spot size of the beam, w_2, is converted as obeying Eq.(6.3).

$$\left(\frac{w_2}{w_1}\right)^2 = \frac{1}{\left(-\frac{f_1}{f_2}\right)^2}. \tag{6.3}$$

The confocal system with two lenses is convenient to produce a smaller focused spot and positon the lenses by selecting focal lengths of lenses.

In oreder to obtain the good coupling efficiency the spot size into the fiber must be almost the same as the radius of the fiber core, 3.2 μm. In case of our lens system, the two matching lenses has f_1=400 mm and f_2=8.3 mm in focal length, then the Gaussian incident beam with a beam waist radius of w_1=164 μm is reduced to the focused spot with a radius of $\frac{f_2}{f_1}w_1$=3.4 μm.

The lens 13 and the fiber coupler with the lens 14 in Fig. 6.1 are set as forming confocal system. The half-wave ($\lambda/2$) plate, 12 in Fig. 6.1, fits the direction of the line polarization of the incident beam to the polarization direction of the fiber, which produced by the strong birefringence.

The output edge of the fiber is cut with a slightly non-perpendicular angle to the fiber tranmission axis by a nipper for precise cutting. In case of using the diamond cutter, the incident and output edges consisting of the smooth sections perpendicular to the fiber axis form a kind of a FP cavity with a cavity length of the fiber's total length, and then the transmitted power flactuates due to the temperature change of the total length. Also, since the shape of the cut section decides the shape of the transmitted light, in order to obtain the circular beam geometry with Gaussian distribution, it is required to cut the fiber carefully.

After a few trials and errors, the smooth section of the output edge of the fiber has been obtained. Fig 6.2 shows the output beam taken by an infrared CCD camera. Its shape can be regarded as almost circular.

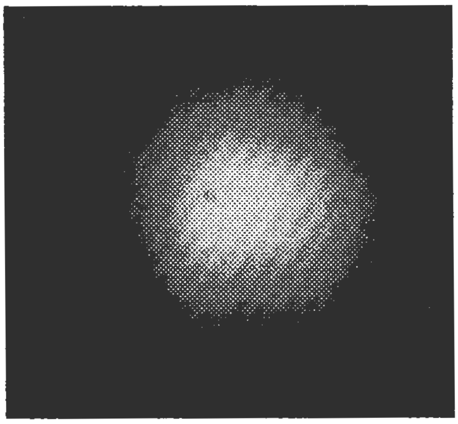

Figure 6.2: The photograph of the output beam from the optical fiber: the oblique lines and the spot nearby the center are caused by the protecting film of the CCD.

The beam profile of the output beam through the lens of the fiber coupler, 16 in Fig.

6.1, with 10 mm in focal length is shown in Fig. 6.3. The output beam is regarded nearly as an ideal Gaussian beam.

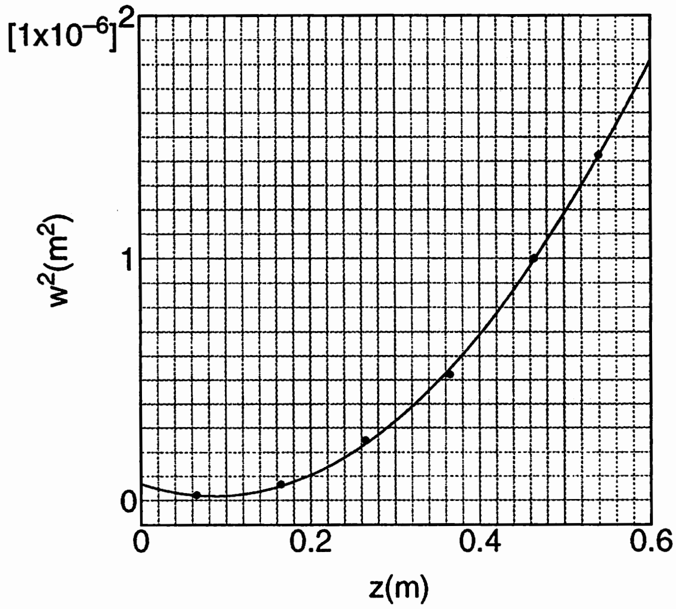

Figure 6.3: The beam profile of the fiber transmitted beam: z is the distance from the fiber coupler, w is the beam radius, and the solid curve is a fit to the data by using Eq.(5.15).

Laser Transducer

Two alighment mirrors, 13 and 14, and the lens with a focal length of 300 mm, 17 in Fig. 6.1 adjust the output beam from the fiber into the TEM_{00} mode of the FP cavity of the laser transducer. One mirror of the FP cavity is glued on a small aluminum block bonded to the edge of the disk antenna and forms an end mirror of the FP cavity, and the other is glued at an alminum mass suspended by two tungusten wires and a front mirror of the FP cavity. The glue is an "alonealpha 201" of TOA GOSEI Co., Inc. Since a suspended mass as a pendulum behaves as almost the free falling mass at frequencies higher than the resonant frequency of the pendulum, it is considered that this suspended mirror is fixed in an inertial frame at the resonant frequency of the disk antenna. Moreover the suspension as a pendulum works to isolate the front mirror of the FP cavity from external noise at higher frequencies.

The reflected light from the FP cavity is modulated in amplitude responsing the phase fluctuation in the FP cavity and is detected by a rf detector, PD1 in Fig. 6.1, using a PIN silicon photodiode S3759, HAMAMATSU PHOTONICS K.K. (see Appendix A). The photodetector needs a low noise performance for sensitivity. I made it by applying a LC tank circuit resonant at the phase-modulation frequency 15 MHz of the laser. The signal detected by the photodetector is demodulated with a demodulator by mixing with a properly phase-shifted reference oscillation, which consists of a passive double balanced mixer (R&K Inc. M1) and a low noise operatinal amplifier AD797 (ANALOG DEVICES Inc.). The demodulated signal, *i.e.*, the error signal, is fed back to the actuator, consisting of two coils and two magnets attached to the suspended mass, through the servo filter to lock the FP cavity on the resonace condition. By measuring the demodulated shot noise level of the photodetector as a function of the photocurrent, we can estimate the shot noise level of the laser transducer in operation.

Also the error signal from the laser transducer is transmitted to an A/D convereter, VME, which is able to acquire signals at fast frequencies, and to a UNIX workstation at last. A Gaussian fitting for the error signal data gives to the effective temperature of the transducer.

Figure 6.4 shows the final set up of the optical elements. The pendulum is sususpended as a double pendulum from two XZ-stages on the plate fixed at aluminum beams connected to the upper disk, and a photodetector (PD in Fig. 6.4), a polarizing beam splitter (PBS), a quadrupole plate ($\lambda/4$), and two coil bobins as the feedback actuator are fixed at a plate joined to the one of alminum beams. The two alignment mirrors, a matching lens, and the fiber coupler at the output side can be motorized to adjust the mode of the output laser light through the fiber to that of the FP cavity, and are Motorized mirror 1 and 2, Matching lens, and Fiber coupler in Fig. 6.4. An eddy current damping system [65] by strong Nd magnets is adopted on the upper mass of the double pendulum to suppress the pendulum motion at the resonant frequenciy of the upper pendulum. All cables for the rf and feedback signal, *etc.*, are wired to the BNC connectors on the flange of the vacuum tank through simple isolation systems, which consist of two cupper blocks and two springs with a large spring constant.

The mechanical elements of the transducer are detailed in the next section.

Parameters of the Fabry-Perot Cavity Table 6.1 shows the parameters of the mirrors used in the laser transducer, *i.e.*, the two mirrors of the FP cavity. The two mirrors have the same concave shape with 1000 mm in curvature radius, are made of silica (produced by SHOWA Optronics Corp.), which have $\phi 20 \times 10t$ mm in dimension and 6.9 g in weight, and the finesse of the FP cavity with these mirrors is about 3000. The concave surface of

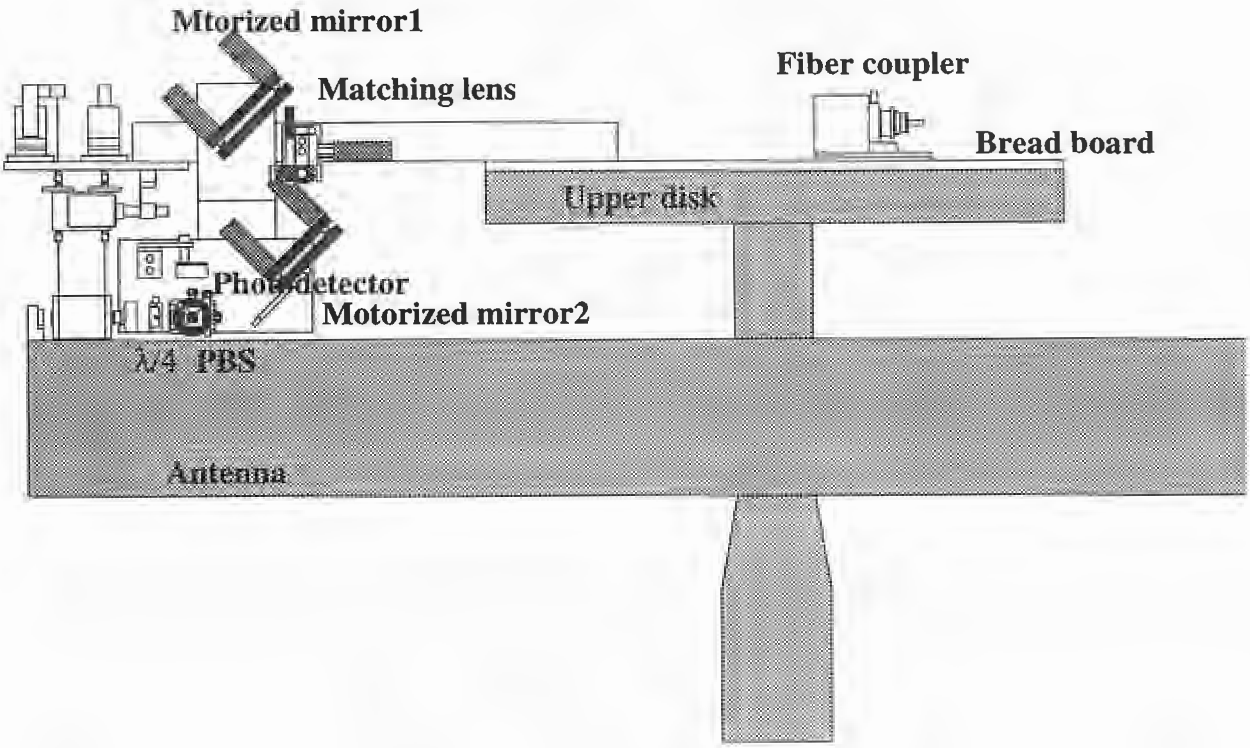

Figure 6.4: The side view of the laser transducer

the mirror is coated by dielectric multi-layers, the opposite surface has an anti-reflection coating.

From above parameters, the storage times can be calculated

$$\tau_s = \frac{2L\mathcal{F}}{\pi c} \approx 6.66 \times 10^{-8} \quad [\text{sec}]. \tag{6.4}$$

Since the quadrupole mode frequency of the ICRR disk is about 1.2 kHz,

$$2\pi \times 1.2 \times 10^3 \times \tau_s \ll 1, \tag{6.5}$$

then the small displacement of the cavity length at 1.2 kHz can be regarded almost as the DC displacement.

Frequency Stabilization System

The frequency stabiblization is realized by using another frequency reference meter. By comparing the oscillaton frequency of the laser with the frequency reference, the laser

Parameter	Symbol	Value	Units
reflectivity	$r_{1,2}^2$	0.999	
curvature radius	R	1000	mm
cavity length	L	10	mm
finesse	$\mathcal{F}$	3000	
beam waist radius	w_0	155	μm
free spectral range	ν_{FSR}	15	GHz
cut-off frequency	$\Delta\nu_{\mathrm{FWHM}}$	4.78	MHz
geometrical factor	$g_1 g_2$	0.98	
higher-mode interval	γ	0.045	

Table 6.1: Parameters of the FP cavity of the laser transucer

frequency can be controlled so as to compensate the difference between both frequencies. In the Pound-Drever method [58], a FP cavity whose cavity length is completely fixed is regarded as a frequency discriminator, and the reflected light for the phase-modulated incident light to such a FP cavity is used to obtain the difference between the resonant frequency of the FP cavity and the laser frequency as a frequency noise (see Section 5.2). This difference is a frequency noise. The feedback of the demodulated signal of the reflected light, *i.e.*, the error signal as the frequency noise of the laser, to the laser can realize the frequency stabilization.

The best method to obtain the frequency reference meter is to fix the two mirrors of a FP cavity by a spacer whose length never changes. In reality, however, such a spacer does not exist, and we cannot realize an absolute frequency reference. Thus the spacer of the FP cavity for the frequency stabilization must be made of a material which is not affected too much by the change of the surrounding environment, especially the change of temperature. The thermal expansion and contraction of the cavity length by the change of temperature changes the resonant condition of the FP cavity. No control of the resonant condition causes that the locking point of the laser beam to the TEM00 mode will be off from the FP cavity some time, and then we can not stabilize the frequency of the laser. In conclusion, two feedback systems are needed. One corresponds to the change of the resonant condition of the FP cavity, *i.e.*, the low frequency components of the error signal, and the other stabilizes the frequency components around the resonant frequency of the antenna, the high frequency components.

The low frequency components can be controlled by changing the cavity length of the FP cavity by, for example, a piezoelectric, or the oscillation frequency of the laser by the thermal control of the laser crystal, which follows the resonant condition of the FP cavity.

I selected the latter, and both low and high frequency components are fed back to the laser.

As shown in Fig. 6.1, except of the feedback control system, the optical design for the frequency stabilization detailed below is in priciple similar to that of the laser transducer.

The two alignment mirrors, 7 and 8 in Fig. 6.1, and the matching lens with a focal length of 400 mm, 6 in Fig. 6.1, adjust the Gaussian mode of the laser beam to the FP cavity. The FP cavity, 11 in Fig. 6.1, consists of two concave mirrors and a super-inver pipe to fix the mirrors. The super-inver cavity is installed in a vacuum tank and suspended as a pendulum for the purpose of seismic isolation on small isolation stacks, and the eddy current magnet damping is applied in oreder to suppress the pendulum motion.

An inver has a small thermal expansion coefficient equivalent to that of glass, for example, flint glass and Pyrex glass. A super-inver has a smaller thermal expansion coefficient, and the change of the cavity length of the super-inver FP cavity is smaller than that made of stainless, alminum, and *etc.*. In this case, it need not take a wide frequency bandwidth for the feedback control, and the thermal control of the laser crystal is easy. The actual feedback bandwidth of the low frequency components is less than 1 Hz, and the thermal control can follow the change of temperature well.

Parameters of the Fabry-Perot Cavity Table 6.2 shows the parameters of the mirrors used in the frequency stabilization FP cavity. The two mirrors have the same concave shape with 500 mm in curvature radius, are made of silica (produced by SHOWA Optronics Corp.), which have $\phi 20 \times 10t$ mm in dimension and 6.9 g in weight.

Parameter	Symbol	Value	Units
reflectivity	$r_{1,2}^2$	0.99	
curvature radius	R	500	mm
cavity length	L	300	mm
finesse	$\mathcal{F}$	300	
beam waist radius	w_0	279	μm
free spectral range	ν_{FSR}	500	MHz
cut-off frequency	$\Delta\nu_{\mathrm{FWHM}}$	1.59	MHz
geometrical factor	$g_1 g_2$	0.16	
higher-mode interval	γ	0.369	

Table 6.2: Parameters of the FP cavity for the frequency stabilization

The cut-off frequency of the FP cavity, $\Delta\nu_{\mathrm{FWHM}}$, is about 1.6 MHz, so the frequency width for stabilization is enough, 100 kHz in width can be obtained easiliy.

Thermal Expansion of the Fabry-Perot Cavity To maintain the resonant condition of the FP cavity, it is better that the cavity length of the reference FP cavity for the frequency stabilization is as constant as possible. In order to realize superiority as the reference, we chose the super-inver pipe to fix the two mirrors. The thermal expansion coefficient of our super-inver pipe, which is made by Daido Steel Co., Ltd. is 0.668×10^{-6}/K at room temperature, it is smaller than that of Pyrex glass, 2.8×10^{-6}/K, and as small as that of fused silica,about 0.5×10^{-6}/K.

Let us consider the case of no feedback control of the low frequency components in the error signal.

If the change of the cavity length due to thermal expansion and contraction is smaller than the FWHM of the FP cavity, the control of the oscillation frequency of the laser to maintain the resonant condition of the FP cavity is not needed, *i.e.*, when

$$\Delta L < \delta L_{\mathrm{FWHM}}, \tag{6.6}$$

we need not to feed back the low frequency components to the laser, where ΔL is the change of the cavity length. From the thermal expansion coefficient of the super-inver pipe, which is defined as

$$\frac{1}{l_0}\frac{dl}{dT}, \tag{6.7}$$

where l_0 is length at 0 °C (293 K). $lislength$ at T K, and T is temperature, and parameters of the FP cavity, if the change of temperature

$$\Delta T < 8.5 \times 10^{-3}\ [\mathrm{K}], \tag{6.8}$$

the change of the cavity length is less than δL_{FWHM}. This indicates that the change of temperature of the FP cavity must be less than 10 mK in case of no thermal control. Even for the vacuum tank at the underground site, it is impossible to realize the change of temperature less than 10 mK. The feedback control to match the oscillation frequency of the laser light to the resonant frequency of the FP cavity must be done.

6.2 Mechanical Design

In this section, I present the mechanical components and elements of the laser transducer and the frequency stabilization system.

6.2.1 Prototype Transducer

In order to develop the laser transducer, it must be made sure whether the FP cavity, which consists of the fixed mirror and the suspended mirror, is locked at the resonant condition on the antenna. Because, as mentioned in Chapter 4, and as shown in Fig. 4.5, the whole antenna is swinging slowly with larger amplitudes than those on the ground at the lower frequency region, it is difficult to control the cavity length of the transducer by feedback. Because the pendulum motion is amplified at the resonant frequency of the pendulum. Therefore I made a prototype transducer and verified to be able to lock the FP cavity at the resonant condition on the antenna.

Figure 6.5 shows a prototype transducer. It consisted of a single pendulum, and Table 6.3 shows the specifications.

Suspended mass	
material	alminum alloy 5056
dimension	$\phi 40 \times 60$ mm L
weight	193 g
support	two grooves, 0.2 mm deep
Suspension	
material	tungsten
dimension	$\phi 0.1$ mm $\times$ 220 mm
resonant frequency	1.06 Hz

Table 6.3: The specifications of the prototype transducer

A suspended mass made of an aluminum alloy 5056 fixed the mirror by three screws weighs about 200 g, and was suspended by two loops of the tungsten wires with 0.1 mm in diameter. The hole of 10 mm diameter was hollowed in the mass for the laser beam, and the hole of 21 mm diameter and 10 mm depth for the mirror.

The wire length was 220 mm, and the resonant frequency of the suspension was 1.06 Hz. Two wires were fixed at a movable plate on the top plate connected with the beam connecting to the upper disk. Since the movable plate with micrometers can change the inclination of the mirror mass, *i.e.*, control the pitch and yaw of the mirror, and is available for the rough alignment. However this plate is not fixed firmly and easy to recieve external noise, for example, the seiemic noise, so the high sensitivity could not be hoped.

Also the suspended mass has two magnets glued at the opposite side to the mirror attached side (Nd:Fe magnet, 2 mm in diameter and 10 mm in length). These and two fixed coil bobins form the actuator for the feedback control. Two coils, denoting 1 and 2 for convenience, have almost the same performance. If the impedance of the coil is defined as $R + j\omega L$, each measured R and L of the two coils are as shown in Table 6.4.

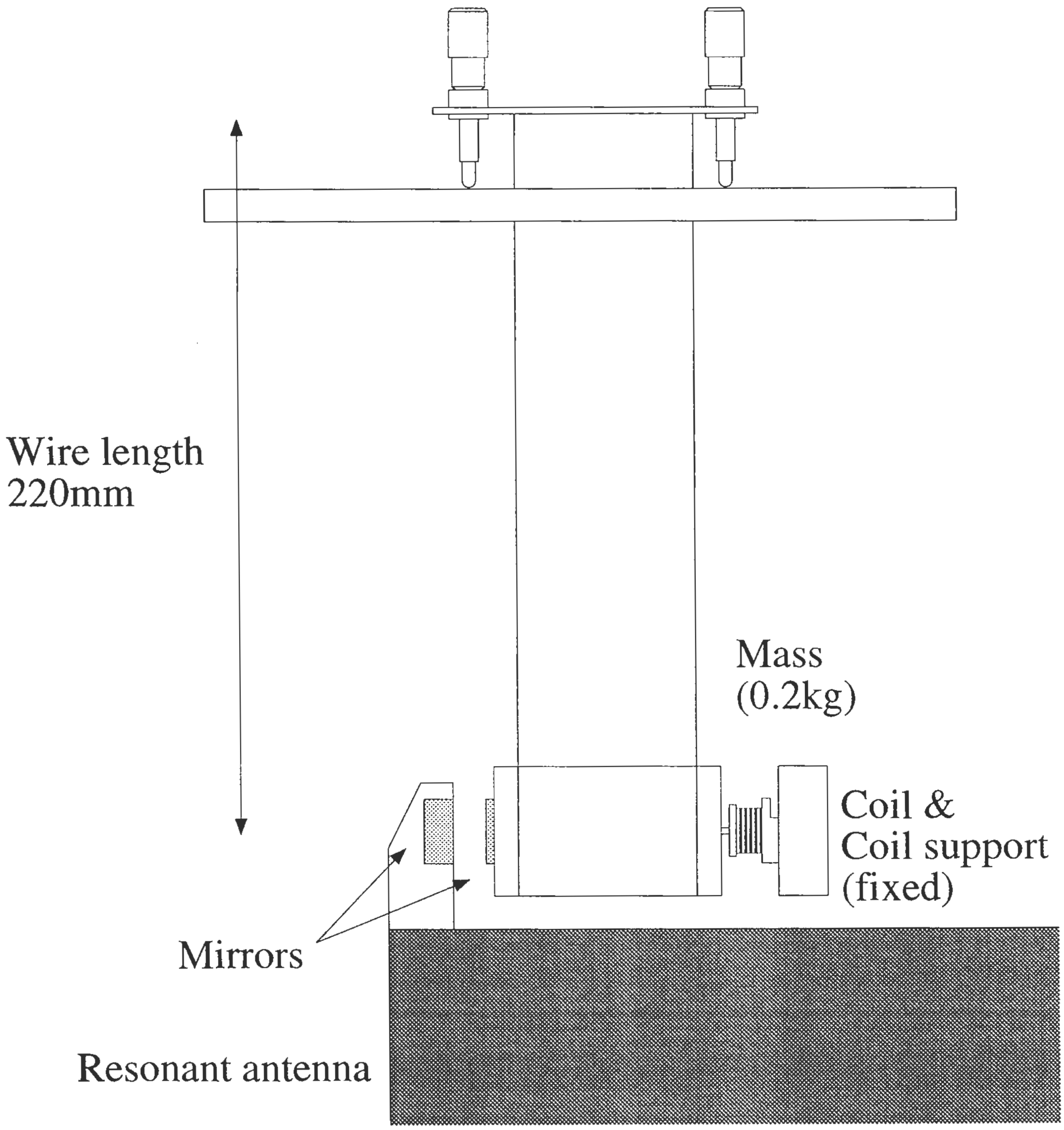

Figure 6.5: The prototype transducer (side view)

Coil	$R[\Omega]$	$L[H]$
coil1	5.06	5.34×10^{-4}
coil2	5.04	5.30×10^{-4}

Table 6.4: Impedance parameters of the actiator coils

Also, by the measurement of force for dc current flowing in the coils, the driving forces of the two coils were given. Both coils have the same driving force 0.124 N/A.

6.2.2 Improvement of the Transducer

The major improvement of the transducer is to design a suspension system utilizing a double pendulum. The double pendulum improves the isolation ratio from the external noise. It was hoped that the many peaks above 100 Hz of the prototype transducer were removed, and the high sensitivity was given.

Also I made new electric circuits, a photodetector and a servo control filetr for the feedback control, to obtain a low noise servo system.

Figure 6.6, 6.7 show the laser transducer consisting of the double pendulum.

In this section I describe each mechanical component of the improved transducer in detail.

Double Pendulum Suspension

The vibration isolation ratio for an n-stage suspension system, at frequencies higher than its resonances, can be approximated by

$$\frac{x_{\text{lowest mass}}}{x_{\text{suspension point}}} \propto \left(\frac{f_0}{f}\right)^{2n}, \tag{6.9}$$

where x's denote the displacements, and f_0 and f are a resonant frequency of the suspension and the frequency of the input vibration, respectively. From Eq.(6.9), it is apparent that the multi stage suspension system realizes a high isolation ratio.

I made a 2-stage suspension, a double pendulum: the upper and lower mass are made of aluminum alloy 5056, each shape is 45 mm $\times$ 50 mm $\times$ 75 mm and ϕ55 mm $\times$ 70 mm, respectively. A hole with 10 mm in diameter is hollowed in the lower mass to pass the laser beam, and a hole with 20 mm in diameter and 9 mm in depth for the mirror to attach the mirror. Two magnets (Nd:Fe magnet, 1 mm in diameter and 10mm in length) are attached to the opposite side of the mirror.

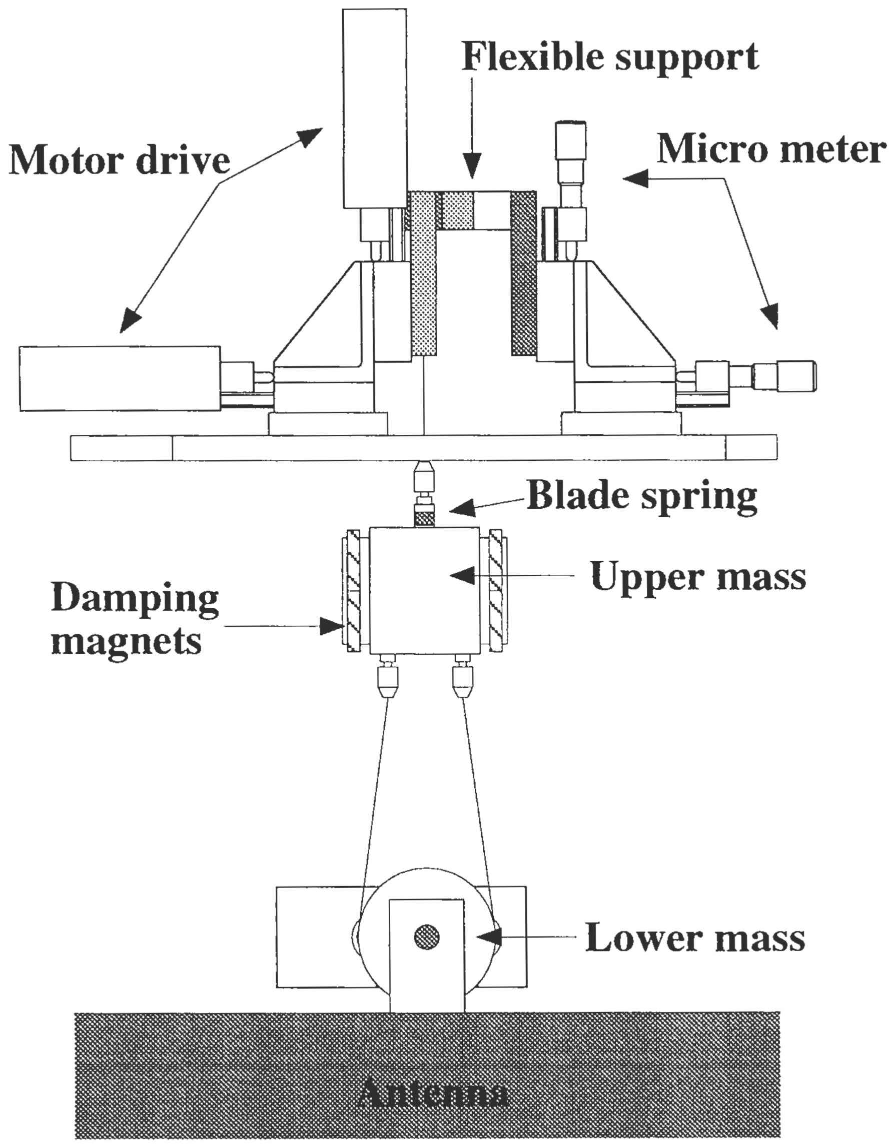

Figure 6.6: The design of the transducer (front view)

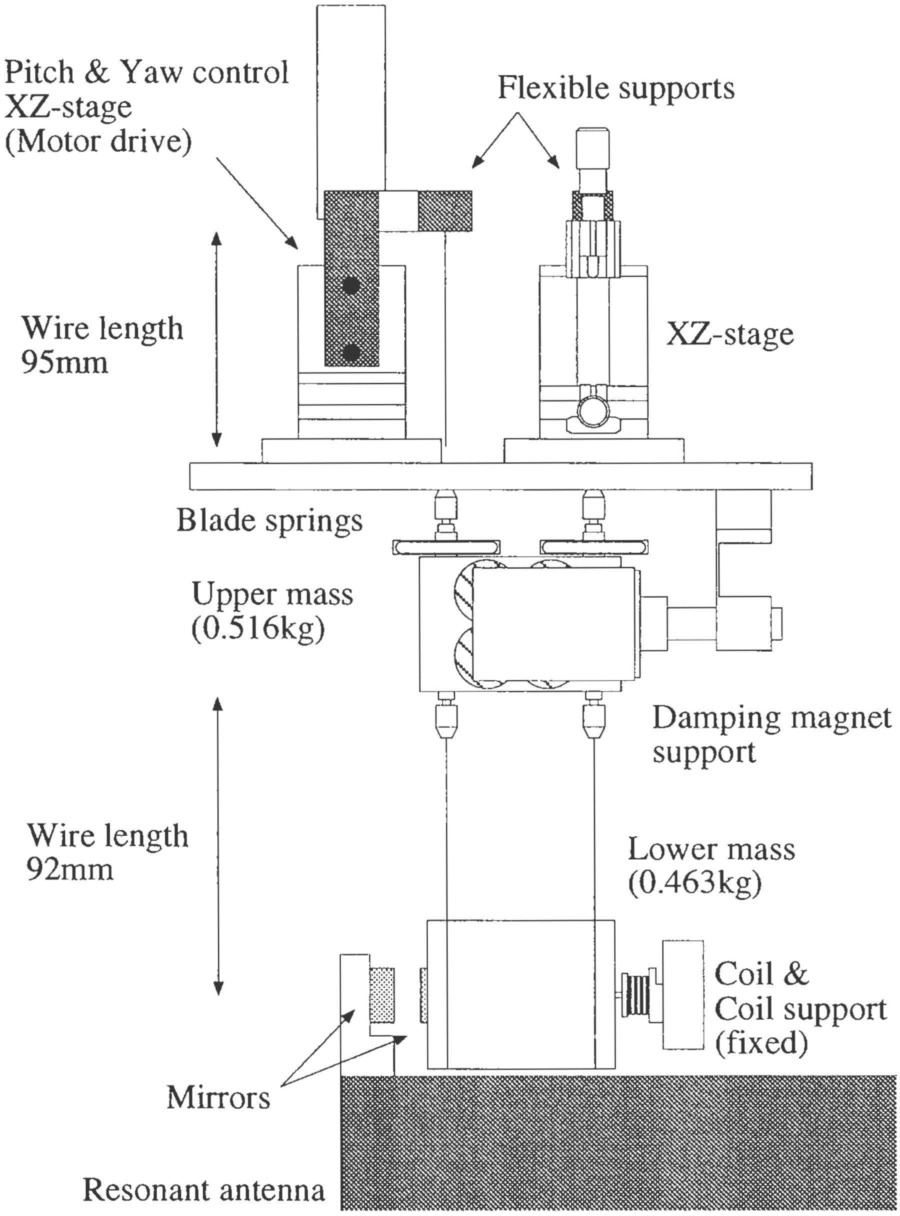

Figure 6.7: The design of the transducer (side view)

The double pendulum suspension aims for increasing the islation ratio to suppress external noises caused by mechanical components, especially, the beam connected to the upper disk.

Also I adopted a lower mass heavier than the mass of the prototype transducer. The reason is to decrease the thermal noise of the pendulum motion even slightly [47].

Flexible Supports

The flexible supports are one of the vibration isolation systems. These are conbimed with the double pendulum suspension and were designed to obtain a larger ratio of the vibration isolation. The flexible supports are made of phosphor bronze, and the main part of these is a beam which has 1 mm in thickness, 15 mm in width, and 15 mm in length. Its calculated fundamental resonant frequency from the shape of the beam and the suspended masses is 79 Hz. The calculated second resonant frequency is 11.56 kHz. In the frequency region from the fundamental to the second resonant frequency, a vibration trasmission of such a beam decreases as being proportional to f^2. In order to obtain a good vibration isolation, the fundamental resonant frequency of the beam is as low as possible, and the second resonant frequency is a little higher than a traget frequency, *i.e.*, the resonant frequency of the antenna (see [66]). When the second resonant frequency is lower than the resonant frequency of the antenna, the third, fourth, or higher resonance might coincide with the antenna resonance, because thsese resonances exist continuously at frequencies higher than the second resonance. Although the isolation of the double pendulum reduces these resonance, it is better that the antenna resonance exists between the fundamental and second resonant frequencies of the beam.

The lower fundamental frequency of the beam of the flexible support, which is given by a thinner or longer shape of the beam, gives a high isolation ratio from vibrations of a supported point, *i.e.*, the beam connecting to the upper disk. Considering the large amplitude of the motion of the upper disk at lower frequencies, the fundamental frequency should not be less than 20 Hz. The pendulum motion might amplifies the fundamental resonance of the beam of the flexible support, and then the feedback control of the FP cavity will become hard. So I designed the shape of the flexible support which had the fundamental frequency between 20 Hz and 100 Hz.

Eddy Current Damping

A pendulum amplifies the external motion at the resonant frequency. A double pendulum amplifies so large, when resonant frequencies of two pendulums are almost the same. Unless the pendulum motion is suppressed, it is impossible to feedback-control the FP cavity. In order to suppress this large motion of the pendulum, I adopted an eddy current damping applied to the upper mass. The damping force is produced between 8 strong Nd:Fe magnets with 20 mm in diameter and 5 mm in thickness and supresses the pendulum motion of the upper mass, and the motion of the lower mass is suppressed automatically.

The damping magnets are supported flexibly by a phosphor bronze beam. If the magnets are supported rigidly, external noises at its supported point fluctuates the magnets so that the damping to the upper mass weakens. In order to prevent the upper mass from fluctuating, the magnets should be isolated.

In the simple model for magnets regarded as a concentrated mass and the beam, its fundamental resonant frequency is about 40 Hz.

Vertical Vibration Isolation

Vertical vibration can easily couple to the horizontal motion and cause noise. In order to isolate the vertical vibration, two rectangular blade springs are inserted at the suspension point of the upper mass. The spring has 0.5 mm in thickness, 8 mm in width, and 40 mm in length, and is made of phosphor bronze which is nonmagnetic and can be used in vacuum. Its fundamental resonant frequency is 20 Hz, and was designed to isolate vertical vibration above this frequency. However the effect of the springs was not observed.

Alignment Control Using Motordrives

Since the suspension system is installed in the vacuum tank, the double pendulum should be controlled from outside the tank to align the lower mass to the incident beam. For simplicity, the alignment is realized by controlling the position of one of the suspension points of the pendulum. The upper mass is suspended by two tungsten wires; one is fixed at the XZ-stage with micrometers, and the other is fixed at the XZ-stage with motordrives. By using motordrives, the yaw and pitch of the lower mass can be controlled. However, since changes of the yaw and pitch of the mirror by motordrives are large and affect the mode matching of the FP cavity considerably, the motordrive control of the XZ stage are used only for a rough control: above 1μm from the motordrive specification. The fine alighnment to match the incident beam to the mode of the FP cavity is controlled by two alignment mirrors, 18 and 19 in Fig. 6.1, which are controlled by motordrives, too. Since motordrives equipped with alignment mirrors produce a small change of the inclination of the mirror, they enables to align the incident beam to the TEM_{00} mode finely.

Table 6.5 shows the specifications of the improved pendulum.

Upper mass	
material	alminum alloy 5056
dimension	45 × 50 × 75 mm L
weight	516.2 g
support	two wires and blade springs
Suspension of the upper mass	
material	tungsten
dimension	ϕ0.1 mm × 220 mm
resonant frequency	1.62 Hz
Lower mass	
material	alminum alloy 5056
dimension	ϕ55 × 70 mm L
weight	463.5 g
support	two wire loops
Suspension of the lower mass	
material	tungsten
dimension	ϕ0.1 mm × 220 mm
resonant frequency	1.64 Hz

Table 6.5: The specifications of the double pendulum

6.2.3 Frequency Stabilization

Figure 6.8 shows the FP cavity in the small vacuum tank for the frequency stabilization. The super-inver cavity is 330 mm in length, 30 mm in diameter, and is hollowed out with a diameter of 15 mm and a length of 300 mm and with a diameter of 20 mm and a length 15 mm at both ends. The two mirrors are fixed by screw rings at both ends of the cavity. The FP cavity itself is suspended as a double pendulum from the top plate on the isolation stacks. The cavity has about 1400 g in mass, and the upper mass, Copper block in Fig. 6.8, is made of copper with a mass of 1200 g, which is damped its pendulum motion by 8 Nd magnets.

Firstly, we locked the laser beam to the FP cavity in this system. In case that the upper mass was not damped very well, the pendulum motion of the super-inver cavity would make it hard to lock at the resonance condition. However, the copper block was damped very well, we could lock easily on the resonance, and two feedback control systems, the feedbacks of the lower and higher frequency components of the error signal to the laser, were realized. They works stably, and the frequency stabilization succeeded.

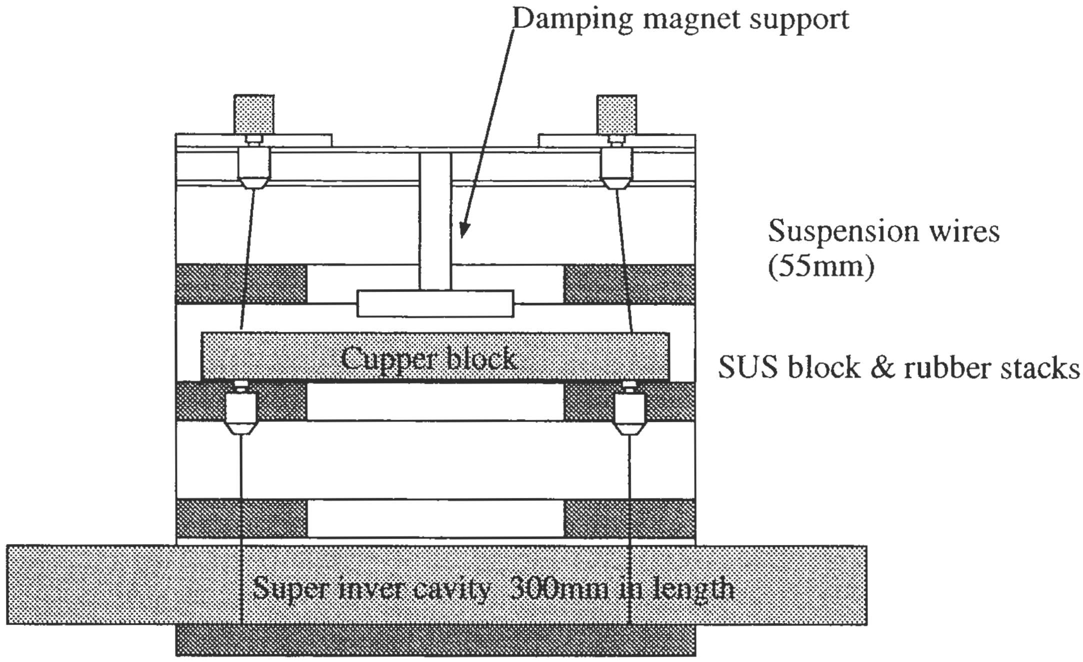

Figure 6.8: Fabry-Perot cavity for the frequency stabilization

Seconarily, we tried to lock the laser beam through the optical fiber. Figure 6.9 shows the stabilization system utilizing the output beam from the optical fiber. The output beam is divided into two optical paths by the polarized beam splitter (PBS in Fig. 6.9), one is for the transducer (TRD) and the other is aligned to the FP cavity (Cavity) through a matching lens (f: 400 mm in focal length) by two motorized mirror (Motorized mirror 1 & 2). The reflected light from the cavity is detected by a photodetector (PD, see Appendix A). Two mirrors, M1 and M2, chnage the height of the optical path.

Two feedback controls of the lower and higher frequency components worked stably and, this system is operating now. This system which uses the output beam from the fiber aims to suppress an external noise which is mixed into the beam through the optical fiber, for example, the vibration of the rotary pump and a sound noise. If the optical fiber picks up such a noise, this system can reduce it.

In conclusion, the displacement noise of the transducer with the second frequency stabilization system did not change from that of the first system. This indicates that the optical fiber does not pick up external noises.

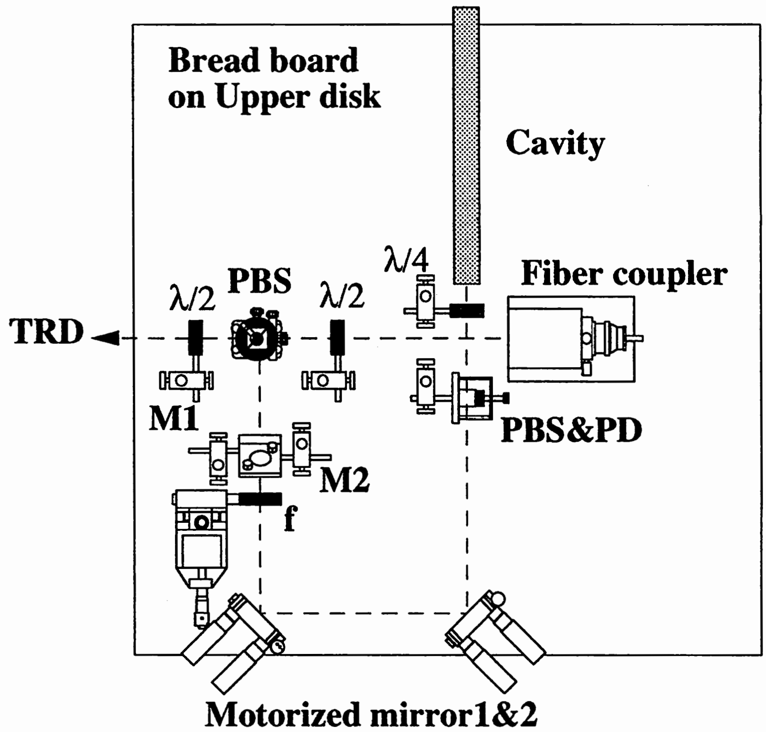

Figure 6.9: Setting of the frequency stabilization system in the antenna vacuum tank

6.3 Servo Control Design

In order to operate the laser transducer, three feedback control systems are deigned and I made each servo control circuit for feedback as shown in Appendix A. One is a pendulum servo to lock the FP cavity to the laser on the resonance. The others are frequency stabilization servos, a feedback servo for the frequency stabilization to stabilize high frequency components and a servo to thermally-control the laser crystal at low frequencies. The block diagrams of these feedback servos are shown in Fig. 6.10 and Fig. 6.11. The low and high frequency servos for the frequency stabilization have fundamentally the same feedback structure, and are represented by the diagram shown in Fig. 6.11.

These three servo control systems are simple negative feedback systems. A feedback loop supresses a signal coming into the system by $1 + G$, where G is the open loop gain of the feedback loop, and outputs as an error signal. In order to obtain a true signal, the error signal must be compensated by the open loop gain.

The feedback loop and the error signal are analyzed by the FFT servo analyzer, we can obtain the true signal from the measured transfer functions.

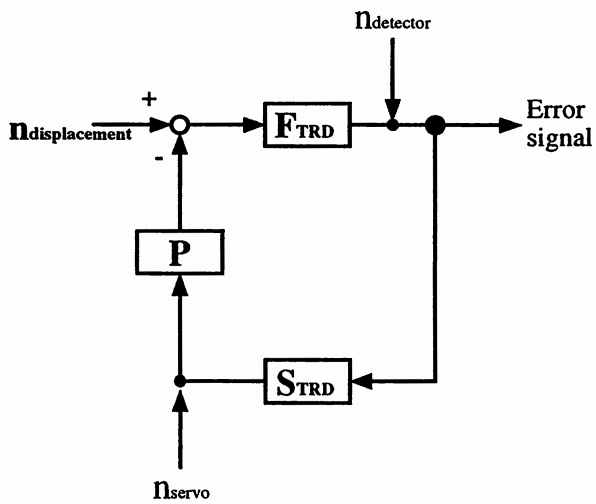

Figure 6.10: Servo control block diagram for the laser transducer: synbols are explained in the text.

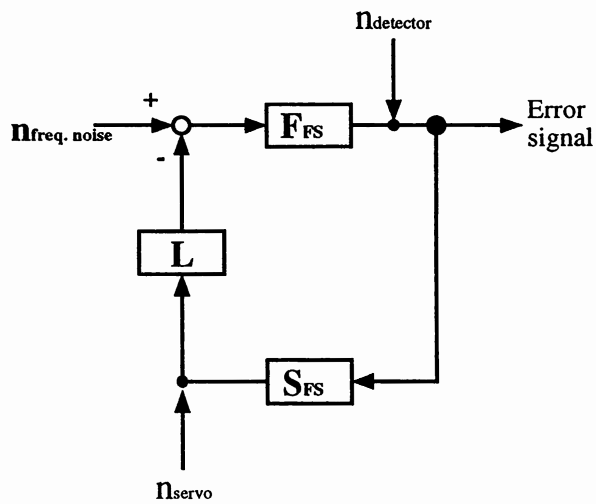

Figure 6.11: Servo control block diagram for the frequency stabilization: symbols are explained in the text.

6.3.1 Loop of the Laser Transducer

Figure 6.10 shows a feedback servo loop of the laser transducer. F_{TRD}, S_{TRD}, and P are transfer functions of the FP cavity, the servo control filter, and the pendulum with the actuator, respectively. $n_{displacement}$ is a small displacement of the cavity length of the FP cavity, and is output as the error signal, v_e, compensated by the open loop gain. $n_{detector}$ and n_{servo} are a detector's noise from the photodetector and the noise of the servo control filter, respectively

The error sinal of the transducer, v_e, is written

$$v_e = \frac{F_{TRD}}{1 + F_{TRD}S_{TRD}P} n_{displacement}, \tag{6.10}$$

where the open loop gain is $F_{TRD}S_{TRD}P$. $n_{displacement}$ presents, when gravitational waves passing, the small displacementof the cavity length caused by a the vibrational motion of the antenna, which is generated by gravitational waves, but naturally includes some other noises which cause a displacement noise: a seismic noise through the isolation stacks, a thermal noise of the mechanical elements, a radiation pressure noise of the laser light, a frequency noise of the laser light, and *etc.* Also the detector's noise, $n_{detector}$, and the nosie of the servo control filter n_{servo}, come into the servo loop at each point as shown in Fig. 6.10. Each noise is reduced by technical improvements as much as possible, when no gravitational wave passing, the output of the transducer, *i.e.*, the error signal, becomes the sum of these noise, and is measured as the displacement noise.

Assuming that the servo control system doesn't contain any electric noises, the displacement noise of the transducer is given by

$$n_{displacement} = \left| \frac{1 + F_{TRD}S_{TRD}P}{F_{TRD}} \right| v_e. \tag{6.11}$$

In reality, electric noises increse the displacement noise, and contribute to the displacement noise with each corresponding gain in the servo loop.

6.3.2 Loop of the Frequency Stabilization

In case of the frequency stabilization, two feedbacks are needed. One corresponds to changing the laser oscillation frequency slowly, which follows the change of the cavity length due to the thermal expansion caused by the change of temperature, *i.e.*, the low frequency components of the error signal from the FP cavity. The other is a normal frequency stabilization, the stabilization of the high frequency components. A servo control filter for the low frequencies feeds back the error signal to the thermal control of the laser crystal, and a servo for the high frequencies to the piezoelectirc of the laser. In their feedback loops in Fig. 6.11, F_{FS}, S_{FS}, and L are each transfer function of the FP cavity, a servo control filter of the low or high frequencies, *i.e.*, and the thermal control of the laser crystal or the piezoelectric which modulates the laser frequency, respectively. $n_{freq.noie}$ shows a frequency fluctuation of the low or high frequency components, *i.e.*, a frequency noise of the laser, is obtained as the error signal suppressed by $1 + G$, where G is each open loop gain.

When the low frequency componenets are stabilized, *i.e.*, the thermal control follows the thermal expansion of the cavity length and the laser beam is locked at the TEM_{00} mode of the FP cavity stably, a long-term frequency stabilization at high frequencies can be realized and frequency componenets at the antenna resonance can be stabilized. In this case, the frequency noises of these two loops are obtained as

$$v_e = \frac{F_{FS}}{1 + F_{FS}S_{FS}L} n_{freq.noise}, \tag{6.12}$$

where $F_{FS}S_{FS}L$ is each open loop gain of stabilization servos, $F_{FS}v_e$ is the stabilized frequency noise. $n_{detector}$ and n_{servo} are detector's noise and noise of the servo control filter, respectively. The frequency noise of the laser is suppressed by the 1+open loop gain, and this frequency-stabilized beam is used for the transducer.

Chapter 7

Performance of the Laser Transducer

In this chapter, I present experimental results of the laser transducer and its noise caracteristics.

7.1 Measurement of the Displacement Noise

Firstly the original version of the transducer, the prototype transducer, that has a simple pendulum stage is desribed. Second the improved version with double pendulum stages, the improved transducer, is presented.

7.1.1 Displacement Noise of the Prototype Transducer

The FP cavity of the prototype transducer is locked to the laser beam by using a suitable servo control filter. The locking stability is determined by the servo filter. The electric circuit of the servo filter is shown in Appendix A. The open loop transfer function of the servo loop determines the properties of the performance of the FP cavity.

Figure 7.1 shows the schematic diagram to control the FP cavity, where the ratio CH-B/CH-A gives the open loop transfer function with noise applied. This measurement gives the transfer function shown in Fig. 7.2 by a FFT servo analyzer (R9211C, ADVANTEST Corp.). The FP cavity of the prototype transducer was stably locked on the resonance condition with a UGF of 400 Hz and phase margin 25°. The error signal includes the componenets of the antenna resonance at 1.2 kHz with a good S/N ratio because the open loop gain is high and the noise is low. Fig. 7.3 shows the Fourier-tarnsformed error signal of the prototype transducer, *i.e.*, the displacement noise of the prototype laser transducer.

Before discussing the noise figure of the transducer, I breifly present the calibration.

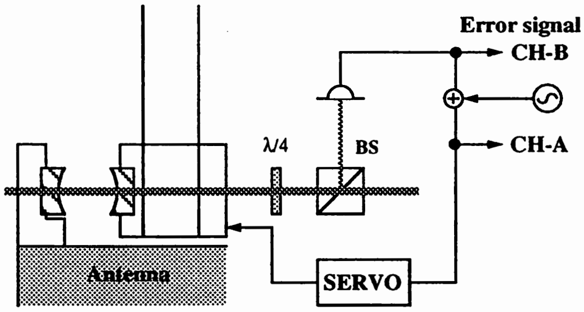

Figure 7.1: Schematic diagram of the servo control of the FP cavity. The reflected light from the FP cavity is used to lock the cavity to the incident laser beam. The open loop transfer function is measured by an FFT analyzer to calculate the ratio CH-B/CH-A.

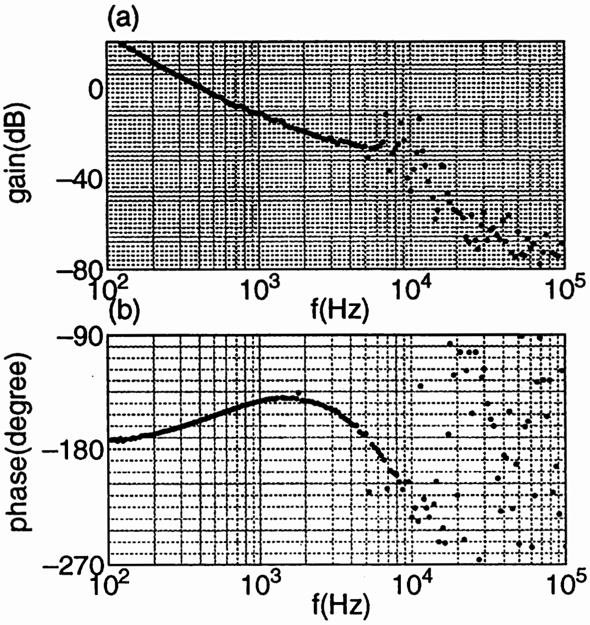

Figure 7.2: Bode diagram of the open loop transfer function of the transducer: (a) the amplitude gain, (b) the phase. Above 10 kHz the transfer function was not measured because of the insufficient sensitivity.

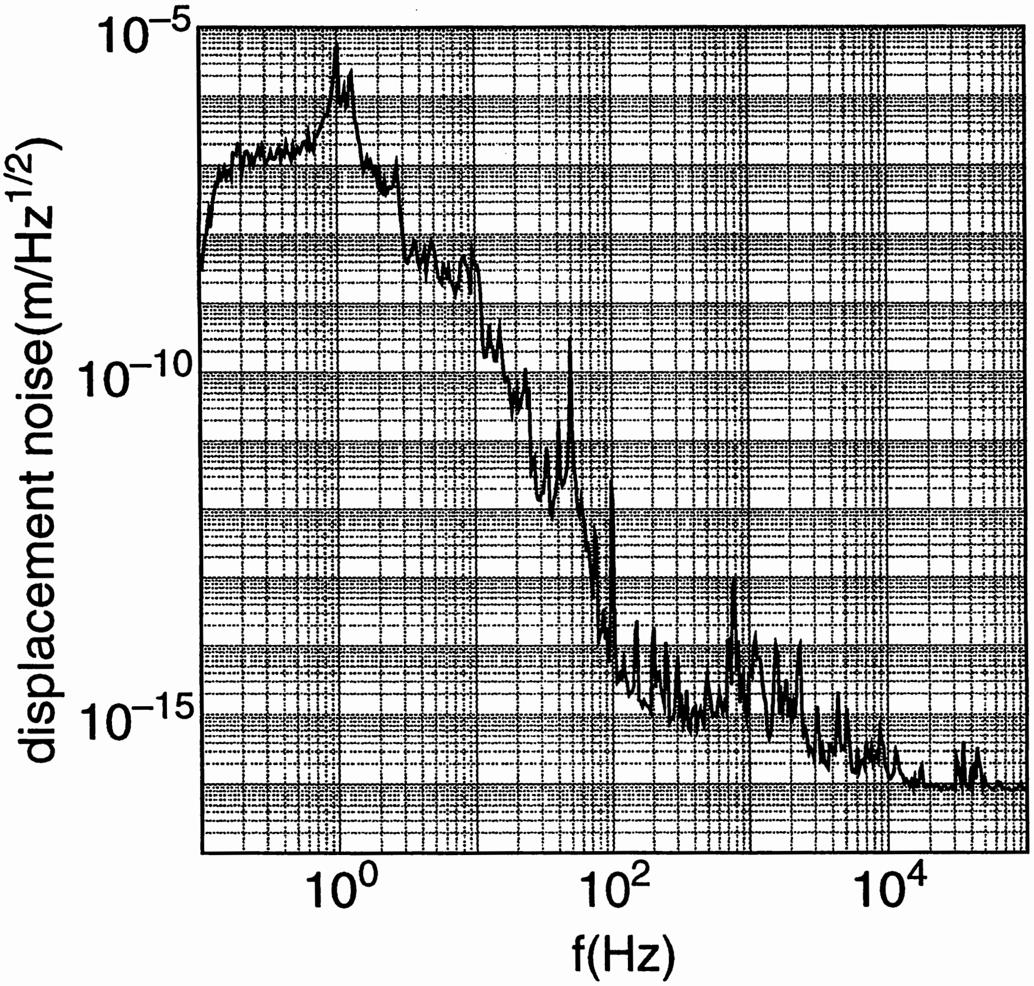

Figure 7.3: Displacement noise spectrum of the prototype transducer. Some peaks at 50, 100, 150 Hz, and $\cdots$, are originated from the power-line frequency at 50 Hz and its harmonics, and there are many peaks caused by mechanical resonaces above 100 Hz.

Calibration

In order to estimate the sensitivity of the transducer, the error signal from the locked FP cavity is converted into the corresponding displacement noise. There are two ways to obtain the calibration factor from the error signal to the displacement.

One way is to calculate the ratio of the interferometer gain between the Michelson interferometer which uses the front mirror of the FP cavity and the FP cavity. Both configurations are shown in Fig. 7.4 and Fig. 7.5. Because the Michelson's gain is reliably obtained by known parameters

As shown in Fig. 7.4, before installing the FP cavity, we make a Michelson interferometer consisting of the suspended mirror, *i.e.*, the front mirror, and another fixed mirror. The output of the Michelson interferometer at CH-B is given by

$$\text{CH-B} = \frac{V_{max} + V_{min}}{2} + \frac{V_{max} - V_{min}}{2} \sin\left(2kx\right), \tag{7.1}$$

where V_{max} and V_{min} are the maximum and minimum output signal intensities, respectively, k is the wavenumber of the light and x is the displacement of the suspended mirror. If the position of the suspended mirror is controlled so that $\sin(2kx) = 0$, a small departure from this equilibrium position produces the output

$$\text{CH-B} = 2kA_0x, \tag{7.2}$$

where A_0 is the possible maximum output of the Michelson interferometer divided by two ,$(V_{max} - V_{min})/2$. Next we find a transfer function α from the voltage applied at the actuator to the displacement of the front mirror. Since the pendulum motion is proportional to $1/f^2$ at frequencies higher than the resonance of the suspension, x becomes $x = \alpha/f^2$. The ratio CH-B/CH-A in Fig. 7.4 gives the transfer function from the actuator to the Michelson interferometer through the pendulum

$$\frac{\text{CH-B}}{\text{CH-A}} = \frac{2kA_0\alpha}{f^2}. \tag{7.3}$$

Applying a sinusoidal signal to the actuator, the output signal accords to the above equation, which gives α.

Simirarly, CH-B/CH-A in Fig. 7.5 gives a transfer function from the actuator to the error signal:

$$\frac{\text{CH-B}}{\text{CH-A}} = \frac{\alpha\beta}{f^2}, \tag{7.4}$$

where β is a gain from the displacement to the signal voltage of the FP cavity.

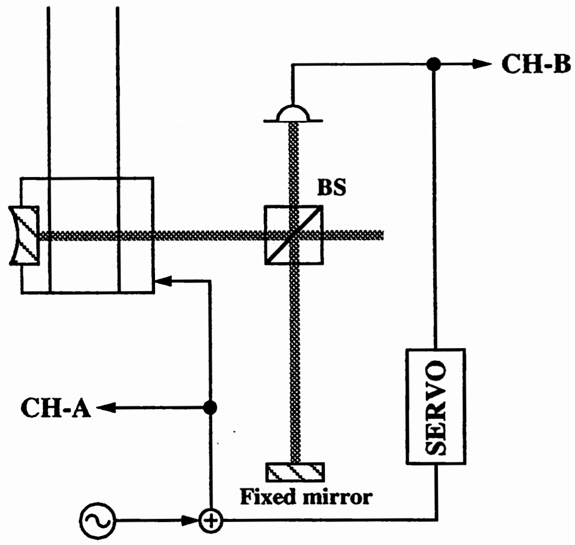

Figure 7.4: Calibration scheme by a Michelson interferometer. The ratio CH-B/CH-A gives the transfer function from the actuator to the output of the Michelson interferometer on the resonance.

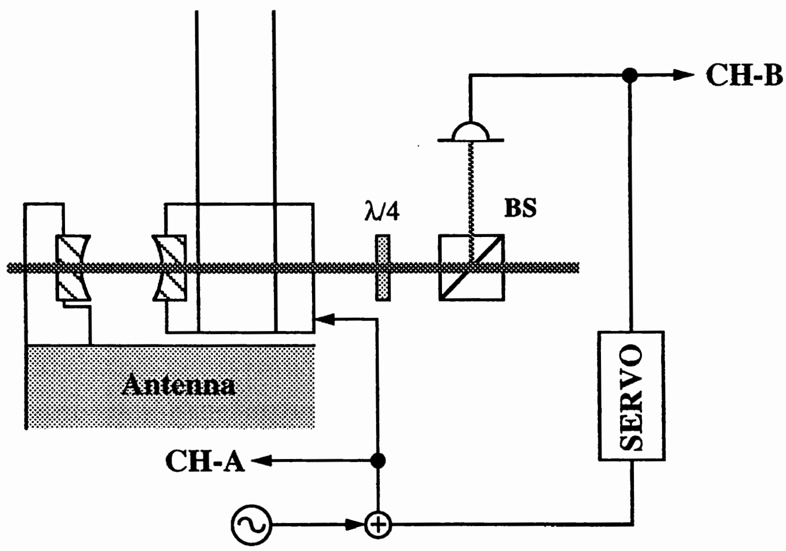

Figure 7.5: Calibration scheme of the FP cavity. The ratio CH-B/CH-A is a transfer function from the actuator to the output of the FP cavity on the resonance.

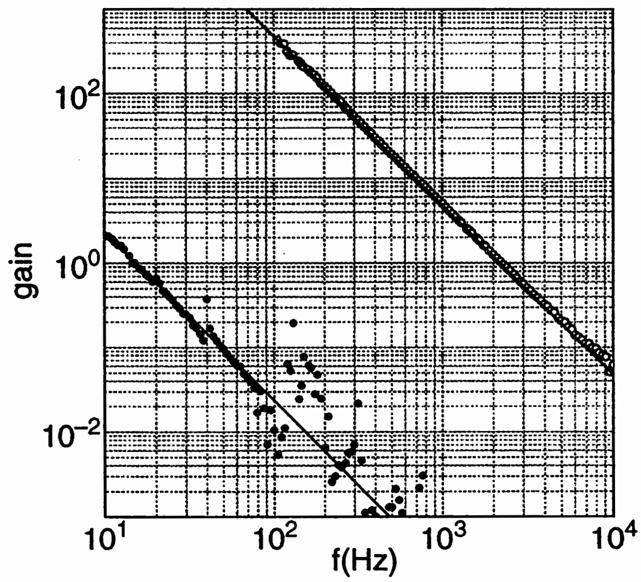

Figure 7.6: Calibration factors in the Michelson interferometer and the FP cavity: the solid circles show the gain curve in the Michelson interferometer, which was satisfactorily measured below 100 Hz, and the circles the gain curve the FP cavity. By these two fitting lines, we obtain the fuction, β, between the displacement and the error signal in the FP cavity.

Gains of each transfer function, CH-B/CH-A, had been measured and are shown in Fig. 7.6. Two fitted lines for the Michelson interferometer and for the FP cavity give the value of β, *i.e.*, the calibration factor of the FP cavity to the displacement.

We obtained

$$\frac{2kA_0\alpha}{f^2} = \frac{243}{f^2}, \tag{7.5}$$

and

$$\frac{\alpha\beta}{f^2} = \frac{4.8 \times 10^6}{f^2}, \tag{7.6}$$

where $A_0 = 1.98$ V.These equations give $\beta = 2.4 \times 10^{11}$ V/m. The value of β changed, however, for different measurements with new settings of the Michelson interferometer, because the same alignment of the mirrors was not realized in every setting.

Although the calibration way utilizing the Michelson interferometer is not good and the β value changes, the order of β was constantly 10^{11}, and β of the improved transducer with the double pendulum was constantly the order of 10^{11}.

The other calibration way to obtain the gain of the FP cavity is to utilize the frequency noise of the laser light.

From Eq.(5.47) where a laser light with some frequency noise, $\Delta\nu_n$, is injected into a FP cavity with a cavity length of L, the frequency noise causes displacement noise $(\Delta\nu_n/\nu)L$. If the noise output of the transducer can be explained almost by only the frequency noise of the laser as usually satisfied, we can estimate the displacement noise corresponding to the frequency one.

From the results of the frequency stabilization described in the next section, it is obtained that the frequency noise of the laser light is ~ 1 Hz/$\sqrt{\text{Hz}}$ at 10 kHz. This frequency noise corresponds to 3.5×10^{-17} m/$\sqrt{\text{Hz}}$ in terms of displacement noise of the FP cavity laser transducer with a cavity length of 10 mm. The noise of the laser transducer without the frequency stabilization is constantly $3.5 \sim 4.0 \times 10^{-17}$ m/$\sqrt{\text{Hz}}$ at 10 kHz. From the above, the FP cavity of the laser transducer has the calibration factor of about 1×10^{11} V/m.

Above two methods give alomost the same value for β to be the order of 10^{11} V/m. In case of utilizing the Michelson interferometer, however, since the setting of the Michelson interferometer considerably affects its output, it is difficult to obtain the accurate value of the gain of it. On the other hand, the way converting the frequency noise outputs is almost constant within an error of the order of 10 %.

For the purpose of the calibration, I selected the way using the frequency noise of the laser for accuracy, and used the Michelson interferometer method to check the order.

Noise measurement

Figure 7.3 shows that the prototype transducer had a sensitivity of about 1.0×10^{-15} m/$\sqrt{\text{Hz}}$ at the antenna resonance. It is considered that below 100 Hz the seismic noise was dominant, and at frequencies higher than 100 Hz many peaks were produced by mechanical resonances of the transducer system. The attainable sensitivity of the prototype transducer was about 1.0×10^{-16} m/$\sqrt{\text{Hz}}$, which was observed above 10 kHz and limited by the noise of the photodetector. The reason that the sensitivty did not attain 1.0×10^{-16} m/$\sqrt{\text{Hz}}$ at the antenna resonance was not identified, one possibility is that the plate for the pendulum suspension was unstable.

In conclusion this level, 1×10^{-16} m/$\sqrt{\text{Hz}}$ is was bad because even the frequency noise of the laser was not observed at higher frequency.

Although the sensitivity was not good and many mechanical resonance peaks above 100

Hz prevented from attaining a higher sensitiviy, the prototype transducer attained continuous operation. It was proved that it is possible to operate the laser transducer consisting of the FP cavity on the antenna, and the isolation stacks was effective in locking the FP cavity at the resonance condition.

To improve the sensitivity, I introduced a double pendulum to the transducer for higher isolation ratio of external noises, and improved electric circuits with lower noise.

7.1.2 Displacement Noise of the Improved Transducer

The FP cavity of the improved laser transducer could be continuously locked at the resonance condition. Figure 7.7 shows the displacement noise spectrum of this transducer compared with that of the prototype transducer.

We maintained the locking of the FP cavity for over one week. This means that we can operate this system for a long time unless any excess vibrations such as earthquakes are caused. The gain of the FP cavity, however, changed from hour to hour corresponding to the change of ambient temperature through the inclination of the disk caused by expansion and contraction of the isolation stacks introduced the change of beam alignment. This is a problem we cannot avoid, and in order to maintain the gain of the FP cavity constant the axis of the incident beam to the transducer had to adjusted frequently so as to cancel the inclination of the isolation stacks.

As shown in Fig. 7.7, at higher frequency the sensitivity of the transucer was improved. Many peaks caused by mechanical resonances were removed and the noise of the photodetector was also reduced.

Below 100 Hz the seismic noise was dominat similary to that of the protype transducer. The noise level in the frequency range of tens of Hz was smaller than the level measured by the seisomometer shown in Fig. 4.5. It is considered that the noise figure below 100 Hz shows the seismic noise reduced by the isolation stacks. Because the mirror of the double pendulum is isolated from the seismic noise by he isolation ratio of the pendulum at frequency higher than the resonance of the pendulum motion, it is supposed that the seismic noise through the isolation stacks vibrates the end mirror attached to the antenna edge together with the whole antenna. In this case, however, the measured noise spectrum shows that the isolation stacks did not work as calculated around tens of Hz. In the later section this problem is discussed again.

We shall examine the noise of the transducer in detail later. Figure 7.8 and Fig. 7.9 show noise spectra below 2 kHz and 10 kHz with a bandwidth of 1.25 Hz and 6.25 Hz, respectively.

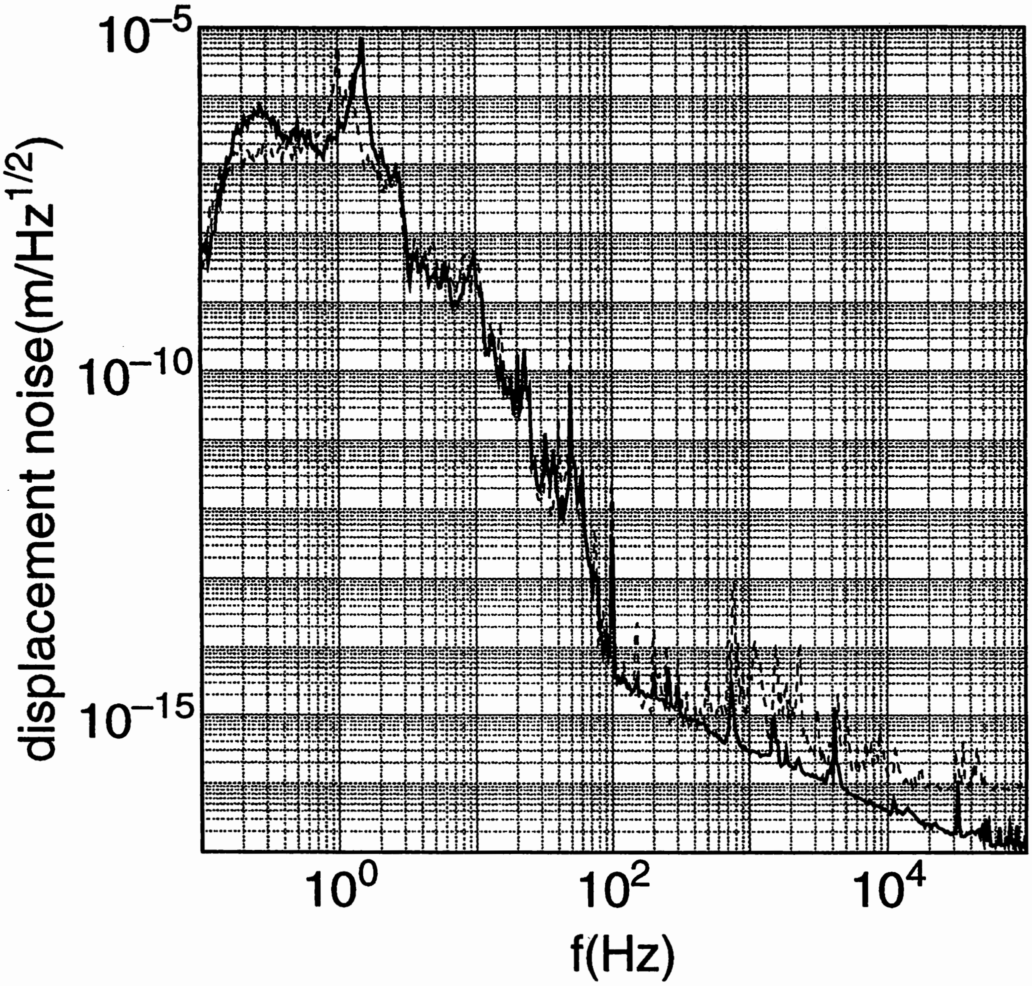

Figure 7.7: Displacement noise spectra: the solid curve shows the noise of the improved transducer, and the dashed curve the noise of the prototype transducer. There are some peaks orignated from the power-line frequency at 50 Hz. The sensitivity of the transducer was improved at higer frequency.

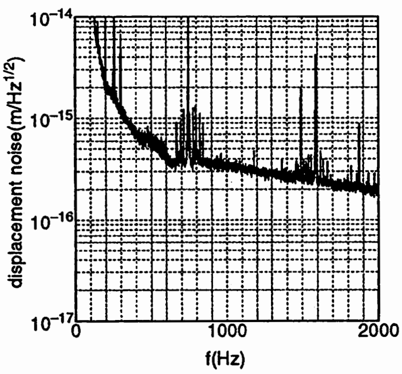

Figure 7.8: Displacement noise spectrum of the transducer. Peaks near 750 and 1500 Hz were caused by the turbo-molecuar pump, and the peak of the antenna resonance can be seen at about 1180 Hz .

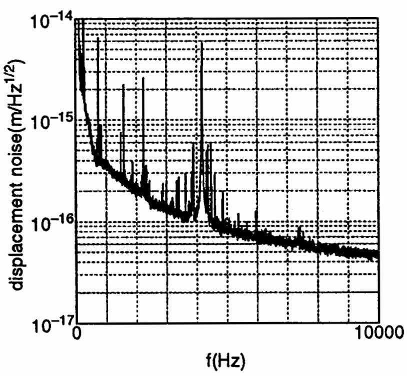

Figure 7.9: Displacement noise spectrum of the transducer up to 10 kHz. Peaks near 0.75, 1.5, and 2.2 kHz were caused by the turbo-molecuar pump, and the resonance at about 4.2 kHz is discussed in the next section.

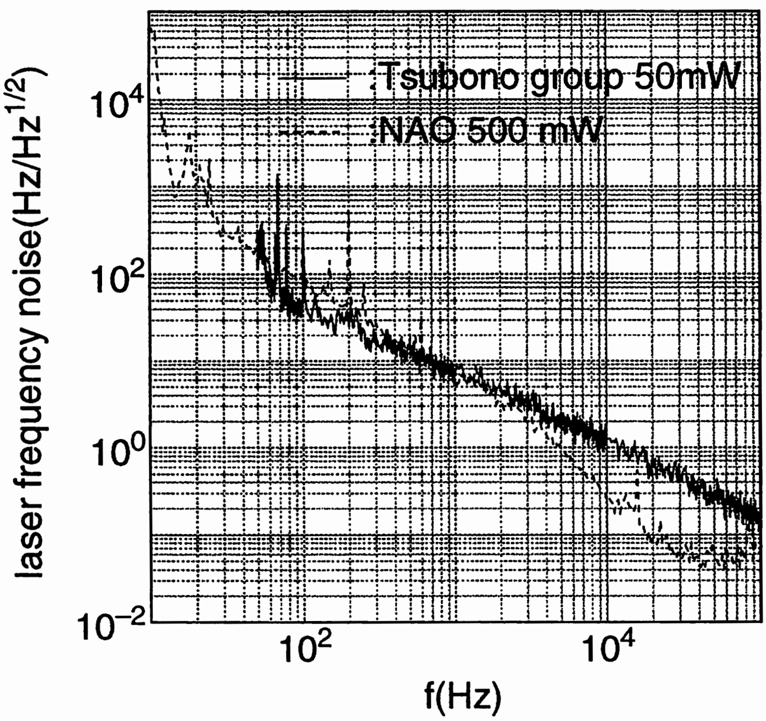

Figure 7.10: Examples of the frequency noise of the Nd:YAG laser: of 50 mW laser of 3 m interferometer in Tsubono group of Univ.of Tokyo (solid line) and of 500 mW laser of 20 m interferometer in NAO at Mitaka (dashed line).

Peaks at about 750 Hz and 1500 Hz corresponding to the rotation frequency of the turbo-moleculer pump and its second harmonics can be seen in Fig. 7.8, and also its third harmonics in Fig. 7.9. These resonances are caused by the vibration of mechanical elements: the isolation stacks, signal cables, or the optical fiber, and which induces a phase noise in the FP cavity are produced by the turbo-moleculer pump. Stopping the turbo-moleculaer pump, these peaks vanished. Since then I have been operating the transducer without the turbo-moleculer pump. While a level of vacuum went worse, the noise figure did not change.

The resonance at about 4.2 kHz is discussed in the next section.

The peak of 1184 Hz in Fig. 7.8is certainly the antenna's motion of the (2,1,1) quadrupole mode. Because it had observed that the amplitude of the peak increased when the antenna was slightly excited in vacuum. The other (0,1,1), (1,1,1), and (3,1,1) modes are the calculated to be 1812 Hz, 1387 Hz, and 1815 Hz, respectively. Other peaks are not clear whether they were caused by mode vibrations or mechanical resonances irrelevant to modal oscillations of the antenna.

From Fig. 7.7, 7.8, and 7.9, it is considered that the floor level of the noise spectrum cooresponds to the frequency noise of the laser. Because the typical frequency noise of the Nd:YAG laser as shown in Fig. 7.10 coincides well with the corresponding displacement noise of the FP cavity with a cavity length of 10 mm. For example, a frequency noise level of 10 $\mathrm{Hz}/\sqrt{\mathrm{Hz}}$ at 1 kHz as shown in Fig. 7.10 becomes a displacement noise of 3.5×10^{-16} $\mathrm{m}/\sqrt{\mathrm{Hz}}$, which agrees well with the noise of the transducer.

From the above results, we had to construct the frequency stabilization system for the laser frequency noise in order to verify that the frequency noise limits the noise level of the improved transducer, and to acheive a higher sensitivity.

7.2 Frequency Stabilization

The configuration of the frequency stabilization system was shown in Chapter 6. In this section I present the measurements of the frequency stabilization.

The frequency stabilization system worked stably. For over one week the FP cavity for the frequency stabilization had been locked and the mode matching of the FP cavity and the alignment of the beam had hardly changed. The thermal control of the laser crystal almost completely worked by feedback less than 1 Hz. In conclusion, the frequency stability was achieved an sufficient level, and the stability less than 0.1 $\mathrm{Hz}/\sqrt{\mathrm{Hz}}$ was easily obtained at 1 kHz.

We shall discuss the results of the frequency stabilization in detail.

7.2.1 Measurement of the Frequency Stabilization Gain

Figure 7.11 and Fig. 7.12 show the intensity of the transmitted light of the FP cavity and the error signal from the FP cavity as a function of the frequency of the laser, which is centered at the resonance of the TEM_{00} mode and normarized by the phase-modulation frequency, 15 MHz. The data were taken as follows: since the FP cavity is held by the super-inver pipe, we can ignore the thermal expansion of the cavity in short time scale and assume that the phase signal corresponds to only the frequency shift of the laser. A very slowly increasing or decreasing voltage applied to the thermal control of the laser (SLOW BNC connector) shifts the osillation frequency of the laser, and then a suitable voltage

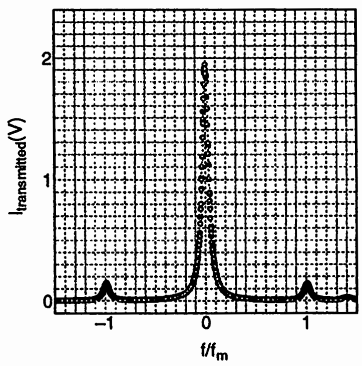

Figure 7.11: Transmitted intensity as a function of the normalized frequency of the laser: the circles are outputs of the photodetector, and the solid line is a fit of the function of the transmission intensity, Eq.(5.6). f_m is the phase-modulation frequency, 15 MHz. The fitting gives the finesse of the FP cavity to be 309.

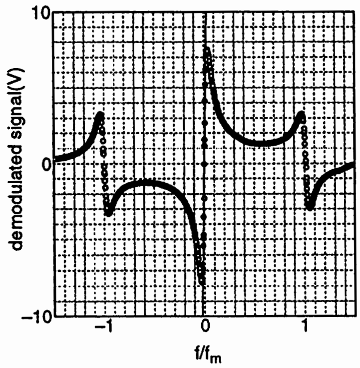

Figure 7.12: Error signal as a function of the normalized frequency: the circles are measured data, and the solid curve is a fit of the function of the frequency response.

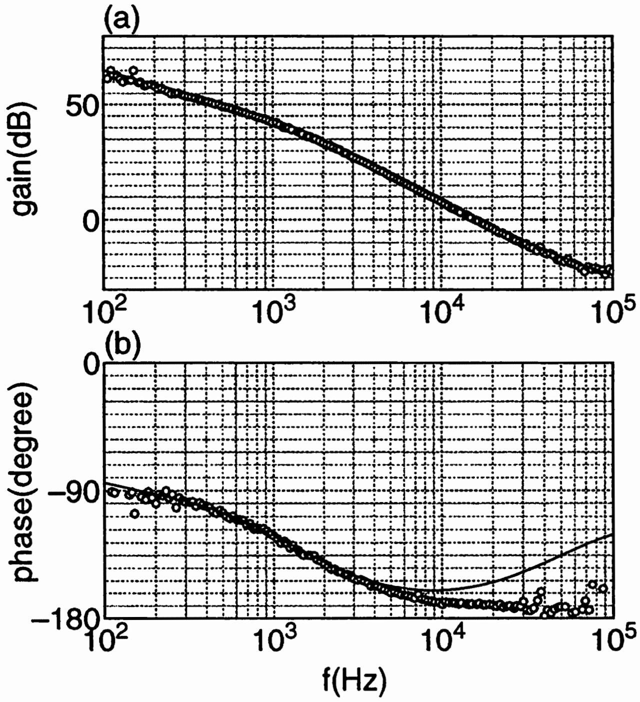

Figure 7.13: Bode diagram of the open loop transfer function of the frequency stabilization system: (a) the gain, (b) the phase, and the solid lines are the calculated transfer function on the basis of those of the servo loop. About 40 dB stabilization would be realized at the antenna resonace.

which matches the frequency of tha laser to the TEM_{00} mode of the FP cavity can be obtained. Here a sine-wave voltage with, for example, 8 V in amplitude and 1 Hz in frequency, is also applied to the piezoelectric of the laser (FAST BNC connector), then the oscillation frequeny of the laser is modulated around the frequency of the TEM_{00} mode by, in case of 8 V, about $\pm$ 30 MHz. Then we can obtain the intensities of the reflected and transmitted light of the FP cavity, and the error signal as a function of the frequency of the laser around the TEM_{00} mode. This scanning with respect to the frequency of the laser allows to obtain precisely the response of the FP cavity for the phase-modulated light.

From the intensity of the transmitted light the finesse of the FP cavity can be calculated, and from a voltage which modulates the phase-modulation frequency, 15 MHz, the frequency change for a voltage applied to the FAST BNC connector of the laser, can be extraced.

In Fig. 7.11 the intensity of the transmitted light and a theoretical fit of the fuction of Eq.(5.6) gave 309 in finesse, and this value indicates the mirrors of the FP cavity have 99 % in reflectivity as designed and a frequency bandwidth for the stabilization is obtained over 100 kHz. In Fig. 7.11 the voltage applied to the FAST BNC is converted into the frequency of the laser by the transfer function of the piezoelctric of the laser and furthermore the frequency is normalized by the phase-modulation frequency, 15 MHz. Also a ratio between the power of the carrier and that of the sideband gave the phase-modulation index, $m = 0.556$. This is under the condition of $m < 1$ explained in Chapter 5.

The fitting curve in Fig. 7.12 shows the change of the error signal as a function of the frequency of the laser produced by the voltage apllied to the poezoelectric, and we can obtain the gain of the FP cavity for the frequency stabilization. It was 1.1×10^5 Hz/V.

As shown in Fig. 7.13, the gain of the measured open loop transfer function of the frequency stabilization servo loop agreed well with the calculated one from the transfer functions of the FP cavity, electric circuits, and the piezoelectric of the laser. At the resonant frequency of the antenna 40 dB gain was obtained. If the frequecncy noise of the laser is typically 10 Hz/$\sqrt{\text{Hz}}$ at 1 kHz, 40 dB gain reduces the frequency noise below 0.1 Hz/$\sqrt{\text{Hz}}$, which cooresponds to the noise level of about 3×10^{-18} m/$\sqrt{\text{Hz}}$.

The freqency stabilization system stably operated with the above characterisitcs. Figure 7.14 shows the stabilized frequency noise and the frequency noise, when the frequency stabilization servo loop is cut (free-run). The frequency noise at free-running was obtained by compensenting the stabilized frequency noise with the loop gain.

The frequency noise is stabilized less than 0.06 Hz/$\sqrt{\text{Hz}}$ at 1 kHz as shown in Fig. 7.14. This frequency noise level produces a displacement noise of 2×10^{-18} m/$\sqrt{\text{Hz}}$ as calculated from Eq.(5.47). Also the future improvement of the frequency stabilization servo will attain the order of 10^{-19} m/$\sqrt{\text{Hz}}$.

Figure 7.15 shows the frequency noise of our laser at free-running in the frequency range from 0.1 Hz to 100 kHz. Except power-line noises and its harmonics, the frequency noise of the laser is almost the same as the typical noise of the Nd:YAG laser, which has a $1/f$ dependency.

7.2.2 Displacement Noise of the Laser Transducer with the Frequency Stabilization

Figure 7.16 shows the observed displacement noise of the laser transducer without the frequency stabilization and the displacement noise in a cavity length of 10 mm equivalent to the frequency noise of the laser which is calculated from Eq.(5.47). These two noise spectra agree very well. It is clear that the sensitivity of the laser transducer without the frequency stabilization is limited by the frequency noise of the laser light. We expect that

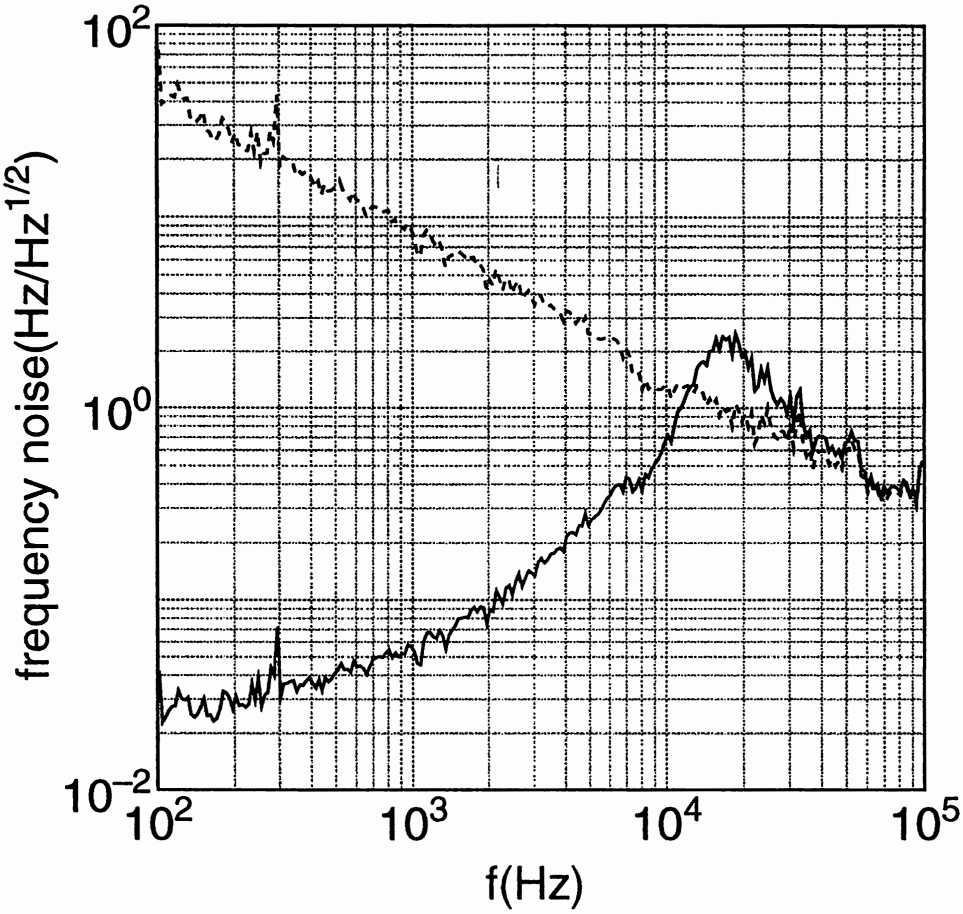

Figure 7.14: Stabilized frequency noise of the laser: the solid line is the stabilized frequency noise, in comparison the dashed line the noise at free-running spectrum of the laser.

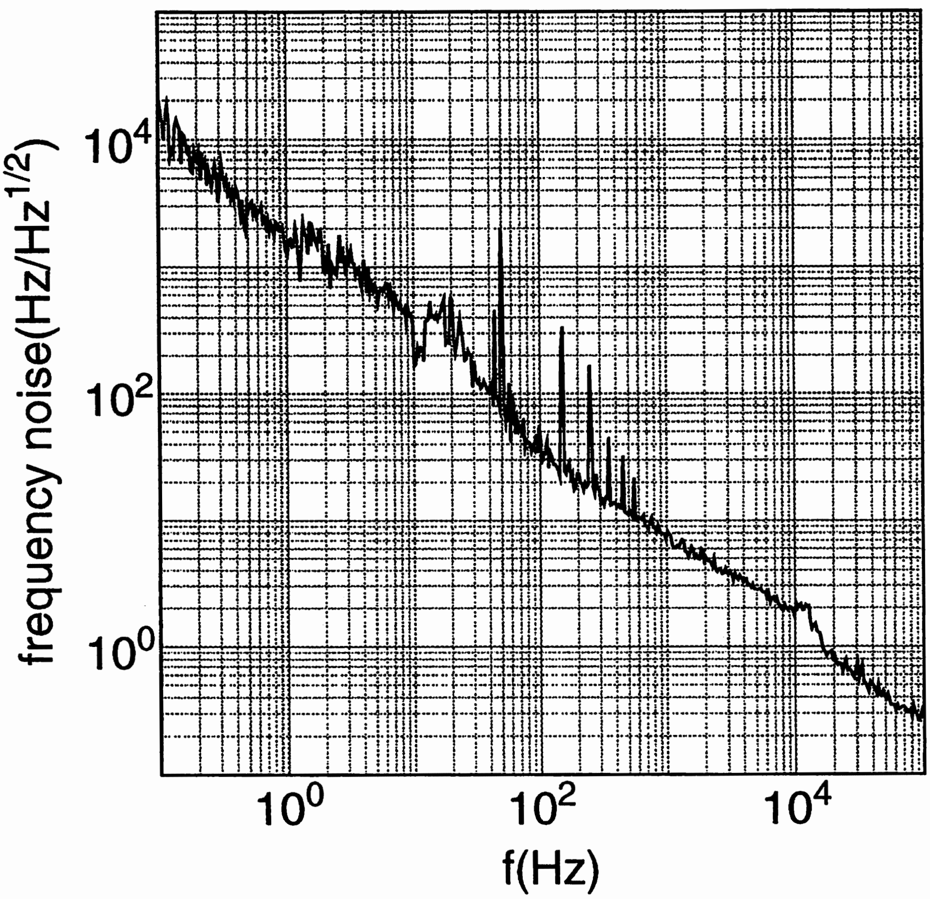

Figure 7.15: Frequency noise of the laser at free-running.

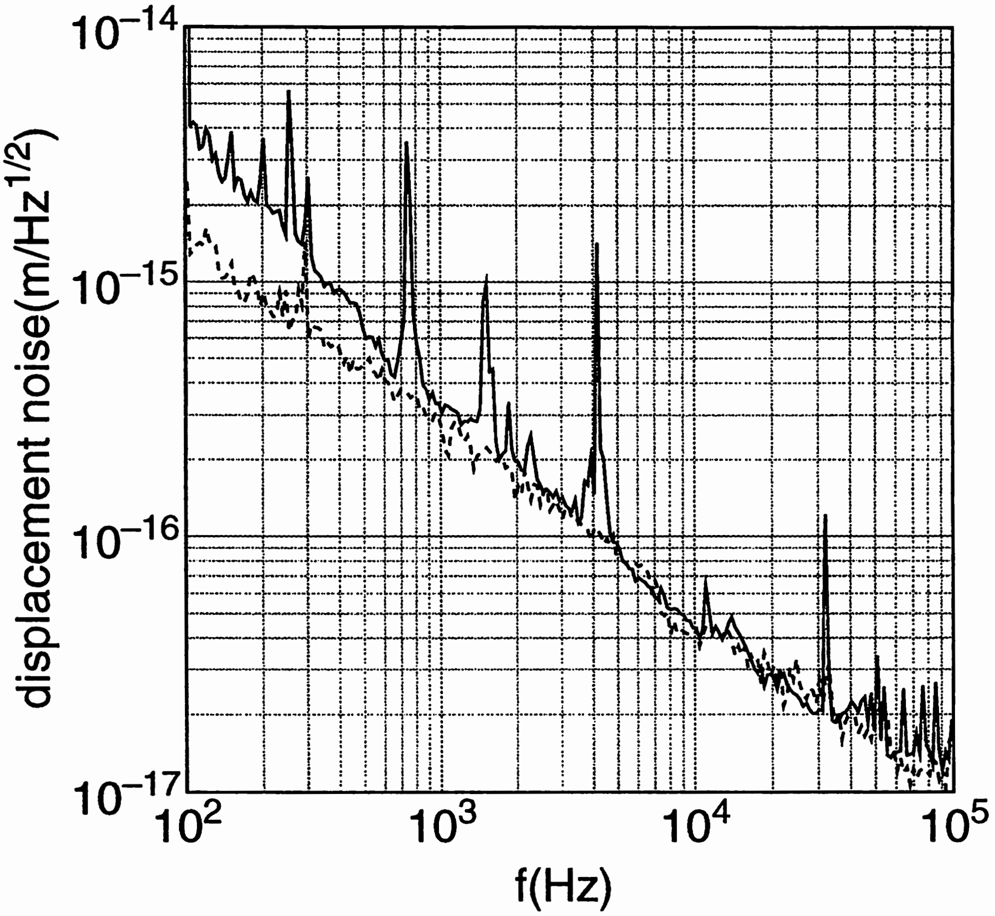

Figure 7.16: Displacement noise spectra of the transducer at free-running: the solid curve is the observed displacement noise of the transducer, and the dashed curve calculated one estimated from the frequency noise of the laser. It indicates that the sensitivity of the transducer is limited by the frequency noise.

the frequency stabilization reduces the noise of the transducer.

The solid curve in Fig. 7.17 shows the displacement noise of the laser transducer with the frequency stabilization, and the dashed line the displacement noise without the stabilization. The frequency-stabilized laser reduced the displacement noise of the transducer, although the sensitivity have not been improved as expected from the frequency stabilization gain, and the level did not reach the order of 10^{-18} m/$\sqrt{\text{Hz}}$. What is the source which limits the sensitivity?

Let us now consider the frequency stabilization system.

Since the frequency of the laser is stabilized by utilizing the output beam from the optical fiber, phase noise in the output beam from the fiber are expected to be stabilized, unless unexpected sudden events induce vibrations on the fiber; accordingly, we can assume that the incident beam to the transducer has only the stabilized frequency noise of the order of 10^{-18} m/$\sqrt{\text{Hz}}$.

Strictly speaking, since the frequency stabilization system stabilizes all noises along its optical path, for example, the vibrational motions of optical elements: matching lens, alignment mirrors, and *etc.*, if the isolation ratio of the isolation stacks is not good, the feedback system of the frequency stabilization might add unnecessaary signals to the laser so as to cancel vibrational noise of such elements. In this case, the laser would have an extra noise. However a FP cavity is most sensitive to the phase fluctuation in the cavity, thus the noise caused by the optical elements woud be considerably smaller than the seismic noise picked by the transducer itself.

In conclusion, it is reasonable to suppose that noises which limit the sensitivity of the laser transducer are generated by sources in some part of the transducer.

Now we will discuss noise sources in detail.

7.3 Estimation of Noises of the Laser Transducer

As shown in Fig. 7.17, the displacement noise of the transducer with the frequency stabilization has a $\frac{1}{f}$ slope from 100 Hz to 3 kHz, and a peak at 4.2 kHz. A resonance in the range from 10 kHz to 20 kHz was caused by the servo cntrol of the frequency stabilization, since the feedback control increases the noise in the vicinicity of the UGF inevitably.

First we will identify the noise source of the peak at 4.2 kHz.

Figure 7.18 shows the noise spectrum of the transducer near 4.2 kHz. The bandwidth of the peak was 6 Hz, and then the quality factor of this resonance is 700. Such a broadband resonance does not originate from a mechanical resonance, because 700 is considerably smaller than the expected ones of mechanical components.

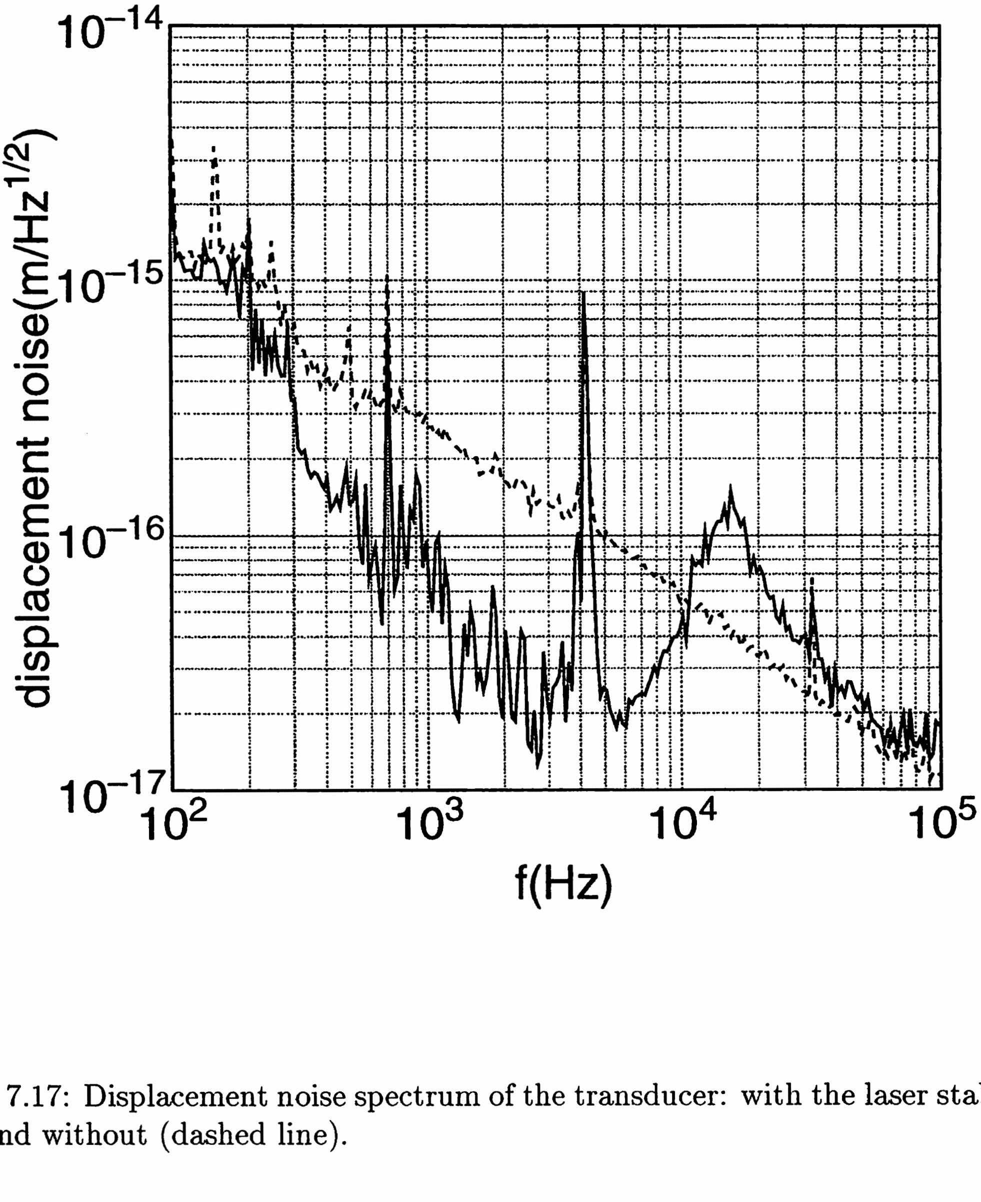

Figure 7.17: Displacement noise spectrum of the transducer: with the laser stabilized (solid line) and without (dashed line).

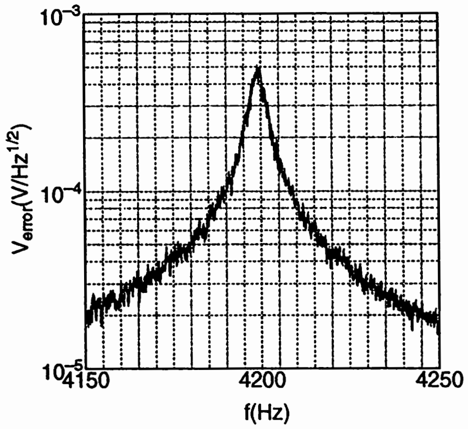

Figure 7.18: Noise spectrum of the transducer near 4.2 kHz. The resonance peak has a quality factor of 700.

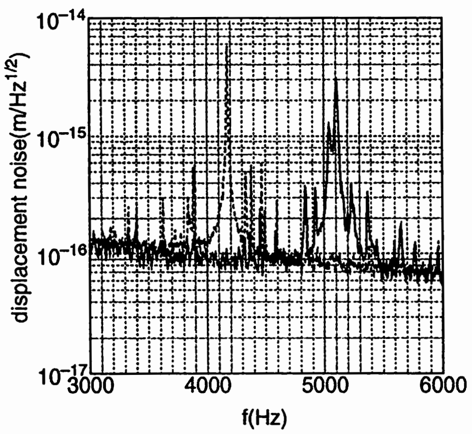

Figure 7.19: Noise spectra of the transdcuer with 31.0 g and 45.6 g in mass of the end mirror block. The resonant frequency moved from about 4.2 kHz of a mass of 45.6 g (dashed line) to about 5.1 kHz of 31.0 g (solid line).

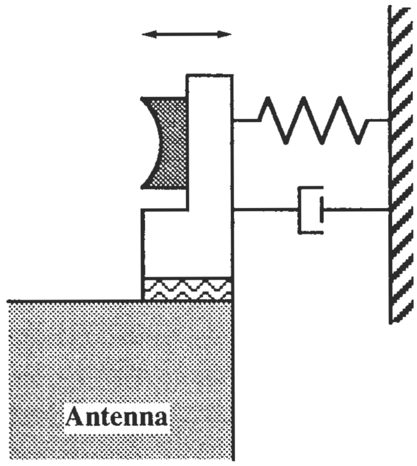

Figure 7.20: Schematic model of the vibration of the end mirror block: the glue (the part of wave lines) is regarded as a spring with dissipation.

Thus let us focus on the alminum block mounting the end mirror of the transducer and the glue which fixes this block on the antenna. Because the glue (alonealpha 201, of TOHA GOUSEI Co., Inc) has a smaller Young modulus of 5.9×10^8 N/m^2, than those of metals, for example, 7×10^{10} N/m^2 of aluminum, and is regarded as a spring as shown in Fig. 7.20, which shows a simple model to simulate the situation. Did the vibration of the block cause such a broadband resonance?

I carried out an experiment to check the above. I changed the mass of the block from 45.6 g to 31.0 g. If the glue is regarded as a spring, the resonant frequency would change.

The result is shown in Fig. 7.19. The resonant frequency moved from 4.2 kHz to 5.1 kHz, and its quality factor did not change. Moreover, I checked the change of the resonant frequency in case of an alminum plate with 0.5 mm in thickness instead of the alminum block. Resonances of the plate, which is regarded as a thin beam, its first, second, third resonace, and higher resonances, were clearly observed at 80, 756, 2606 Hz, and higer frequencies, respectively. It was confirmed that the peak of 4200 Hz was the vibration of the block.

What was the source which caused such vibration? The thermal noise of the block system or seismic noise?

In order to estimate the thermal noise of the block system, we must know several infromation: the process of dissipation of the glue, the bonding condition including a thickness and an area of the glue, and the motion of the block, *etc.* In reality, however, only limited information are clear; the quality factor of the resonance, the resonant frequency, and the mass.

In case of seismic noise, the ambiguity is similar. The source of the vibration of the antenna is regarded as the seismic noise because of the insufficient isolation ratio of the isolation stacks, and it is considered that the vibraion of the antenna makes the motion of the block through the glue as a soft spring. However we know only the resonant frequency of the motion and its amplitude. Unless a better sensitivity of the transducer is realized, it is impossible to analyze this resonance quantitatively. If the seismic noise is large, it is considered that the noise from 100 Hz to about 4 kHz as shown in Fig. 7.21 is caused by the seismic noise. Anyway the seismic noise and the performance of the isolation stacks shoud be investigated in detail.

Second, we consider another noise sources whose origin are definite.

These noise sources are the thermal noises of the doubule pendulum, seismic noise, a detector's noise including the shot noise, the noise of electric circuits for the servo control.

The thermal noises of the double pendulum are expected to be less than the order of 10^{-18} m/$\sqrt{\text{Hz}}$ at the antenna resonance, unless the quality factors are extremely bad less than 1000. The normal setting can make enough quality factors. The thermal noise of the pendulum motion, furthermore, depends on $f^{-5/2}$ at frequencies higher than the resonance of the pendulum [46, 47], about 1.5 Hz, and the thermal noise of the pendulum mass $f^{-1/2}$ at frequencies lower than the resonance of the pendulum mass, about 24 kHz. These frequency dependencies can not be seen in Fig. 7.21. In conclusion, the thermal noises do not determine the sensitivity of the transducer.

The shot noise of an ideal FP cavity with a short cavity length is given by Eq.(5.46). Practically, the imcompleteness of the mode matching, a decrease of reflectivities due to the contamination of mirrors, and *etc.*, increase the shot noise. It appears as the noise of the error signal from the photodetector, V_n;

$$V_n = R_n\sqrt{2}\sqrt{2e\,(I_{dc} + I_{det})}, \tag{7.7}$$

where R_n, is a demodulation gain, e is the electron charge, I_{dc} is the photocurrent in the photodetector, and I_{det} is the equivalent noise current of the photodetector where the power of light into the photodiode is zero. The term $\sqrt{2eI_{dc}}$ corresponds to the shot noise and $\sqrt{2eI_{det}}$ is the noise of the detector. The actual detector noise consists of the shot noise and the noise of the detector, and can be calculated by using Eq.(7.7) and the photocurrent I_{dc}.

Figure 7.22 shows the measured detector noise as a function of the photocurrent, I_{dc}. When the photocurrent is small, the shot noise satisfies Eq.(7.7), while the increase in photocurrent gives rise to the saturation in the photodiode, and V_n^2 departs from being proportional to I_{dc}.

The calculated shot noise level of the transducer from the photocurrent and the measured noise of the detector are shown in Fig. 7.21. The shot noise level is 6.5×10^{-18} m/$\sqrt{\text{Hz}}$ and is higher than the expected level. This is because the mode matching to the TEM_{00}

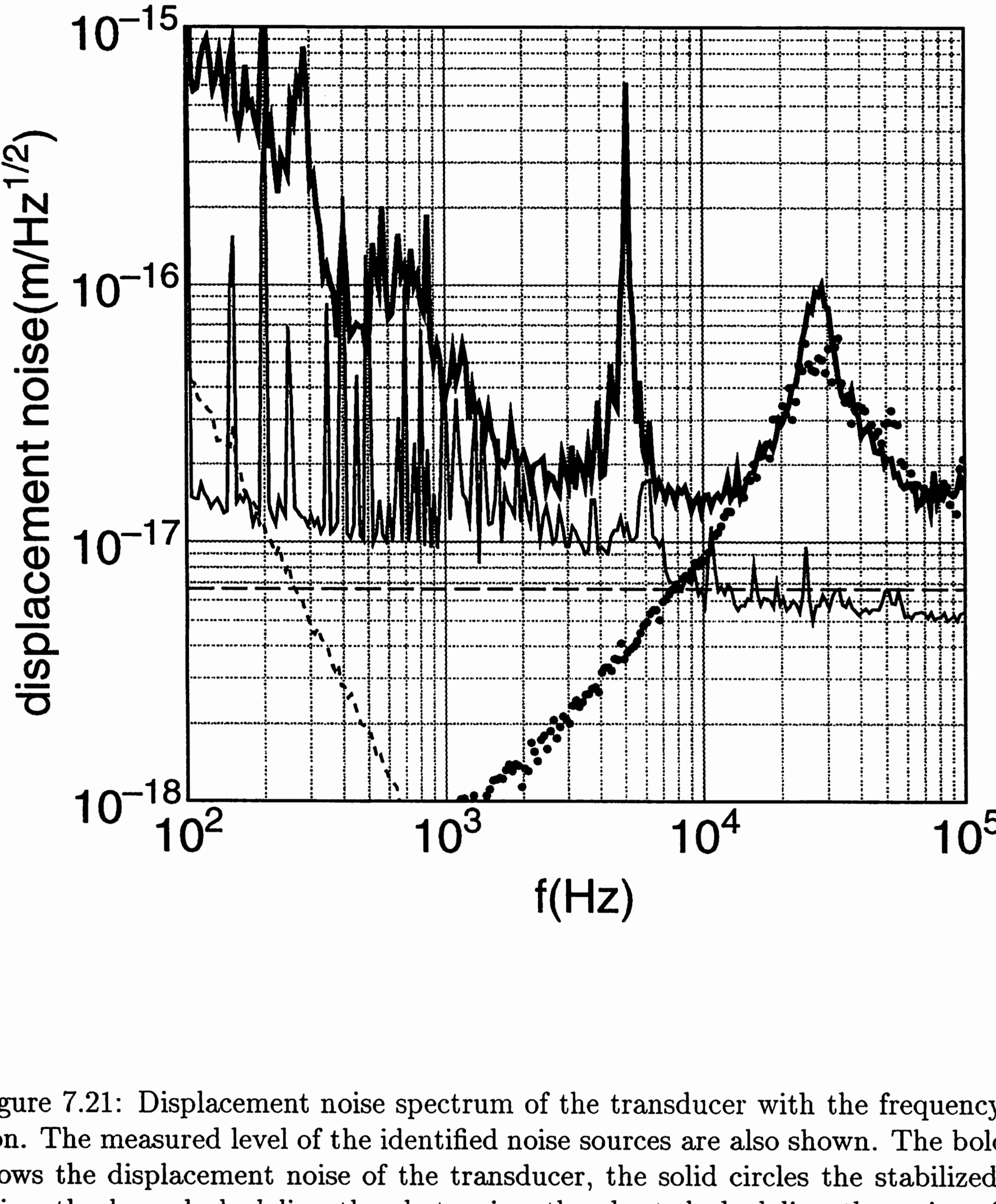

Figure 7.21: Displacement noise spectrum of the transducer with the frequency stabilization. The measured level of the identified noise sources are also shown. The bold solid line shows the displacement noise of the transducer, the solid circles the stabilized-frequency noise, the long dashed line the shot noise, the short dashed line the noise of the servo filter, the thin solid curve the noise of the detector. The peak at 5.1 kHz is caused by the vibration of the end mirror block.

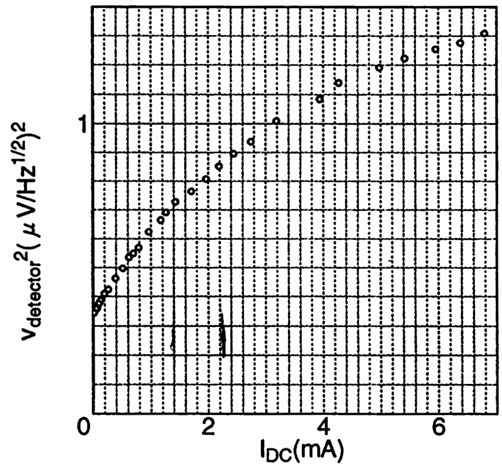

Figure 7.22: Measurement of the shot noise. When the photoelectric currrent, I_{dc}, is small, the noise from the photodetector accords to Eq.(7.7).

mode was not good, and the reflected light was increased. Moreover the imcompleteness of the mode matching decreases the gain of the FP cavity and increased the noise of the detector relatively. The noise of the detector is more than 1×10^{-17} m/$\sqrt{\text{Hz}}$ below about 7 kHz, and contains also many peaks due to the power-line.

The filter noise, *i.e.*, the noise of the servo control circuit, is also shown in Fig. 7.21. As shown in Fig. 6.10, it is considered that the filter noise is added at the point after the servo filter, then the filter noise is increased by the gain of the pendulum.

All of these nnoioses are estimated in equivalent to displacement noise and shown in Fig. 7.21. However, the sum of them and the noise of the stabilized frequeny does not explain the observed displacement noise of the transducer, especially, in the frequency range from 100 Hz to 4 kHz. The discrepancy suggests that unidentified noise source caused the noise in the transducer.

Let us now attempt to discuss the seismic noise.
In respect to the seismic noise, the displacement noise curve in Fig. 7.7 clearly shows the performance of the isolation stack system in a frequency range from 10 Hz to 100 Hz. The power of the frequency dependence is seven if we take the steepest gradient. Since the end

mirror of the transducer fixed on the edge of the antenna which is isolated through five stages of isolation stacks, its frequency dependence of the transfer function becomes five if the every stage of stack has relatively low Q as in the case of the present system. Seismic noise itself varies with the power of two. Because the suspended mirror of the FP cavity is much more isolated by the double pendulum isolation system and it can be regarded as in an ideal inertial frame. Therefore, the noise spectrum of the transducer output represents the motion of the antenna edge referenced to the inertial frame in the frequency range where the double pendulum suspension system effectively works and the end mirror block is firmly fixed.

Thus, the vibrational amplitude of the end mirror is estimated to be less than 1×10^{-20} m/$\sqrt{\text{Hz}}$ as is easily extrapolated in Fig. 7.7. Since the vibration of the suspended mirror is much less than the end, there is no possible seismic noise which explains the cause of the unidentified noise floor in this transducer system. Moreover, the frequency dependence of the noise floor is f itself. Therefore, it is reasonable to conclude its origin has something to do with elctrical noise. However, we have not definately detected yet..

Figure 7.23 shows the displacement noise spectrum up to 2 kHz. Some resonance peaks are excited. The mechanical components caused these noises probably.

Figure 7.24 shows the displacement noise spectrum from 1150 Hz to 1250 Hz. The peak at 1184 Hz is of the (2,1,1) quadrupole mode of the disk antenna. The amplitude of the peak almost coincides with the amplitude of the antenna Brownian motion, *i.e.*, the thermal noise of the antenna:

$$\begin{aligned} \sqrt{\left\langle x^2_{Brownian-motion} \right\rangle} &= \sqrt{\frac{k_B T}{\mu \omega_0^2}} \\ &\approx 2.98 \times 10^{-16} \quad [\text{m}]. \end{aligned} \tag{7.8}$$

Finally let us calculate the performanceof the laser transducer as a gravitational wave detector.

The sensitivity of the laser transducer is about 2×10^{-17} m/$\sqrt{\text{Hz}}$ around the resonant frequency of the antenna. From Eq.(3.62), we can calculate the optimum sampling interval τ_{opt},

$$\begin{aligned} \tau_{opt} &= 2\mu\omega_0 \sqrt{\frac{(\mathrm{e}-1)Q < \xi_N^2 >}{4\mu k_B T}} \\ &= 0.5782 \ [\text{sec}], \end{aligned}$$

and from Eq.(3.63) the effective temperature is given by

$$\begin{aligned} T_{eff} &= \frac{2\omega_0 \tau_{opt}}{\mathrm{e}Q} T \\ &= 2.96 \ [\text{K}], \end{aligned}$$

and is about 3 K. Since then the detectable frequency bandwidth is defined [68] as

$$\Delta f \approx \frac{1}{4\tau_{opt}}, \tag{7.9}$$

and the laser tansducer can detect the strain ampltude of gravitational burst waves,

$$\begin{aligned} h &\sim 2 \times 10^{-17} \times \sqrt{\Delta f} \\ &= 1.3 \times 10^{-17}. \end{aligned}$$

This sensitivty is not sufficient at all and many improvements must be done.

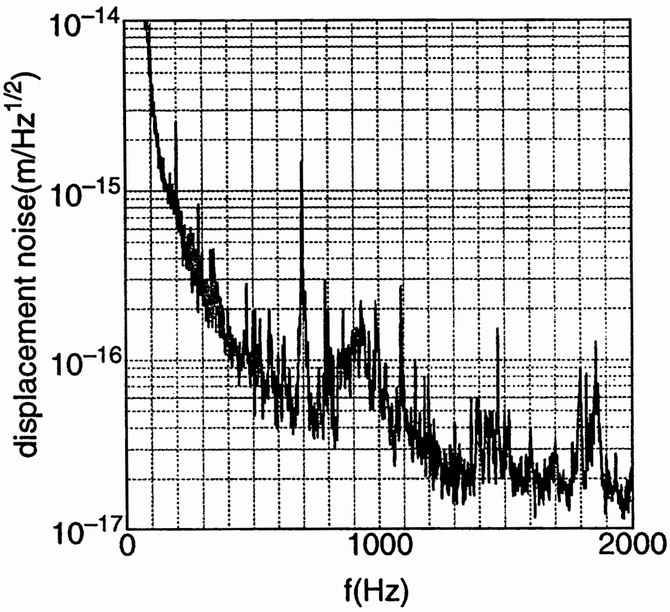

Figure 7.23: Displacement noise spectrum of the transducer. The antenna resonace is observed at about 1180 Hz.

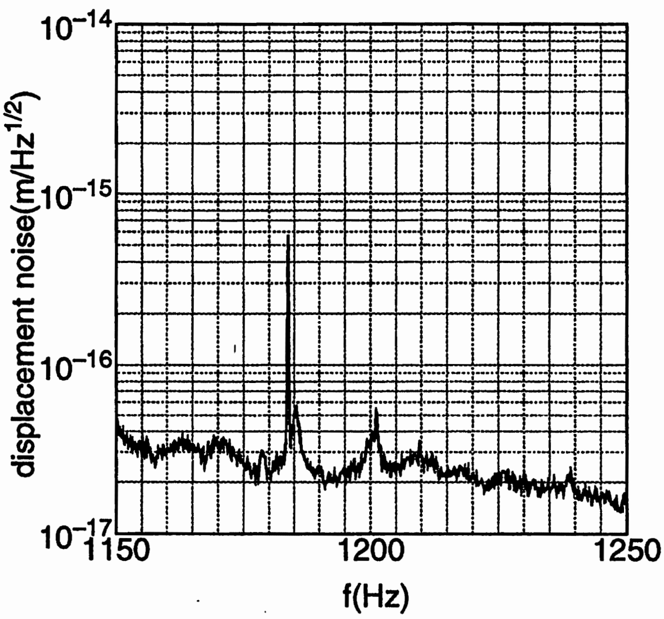

Figure 7.24: Displacement noise spectrum of the transducer. The peak at 1184 Hz agrees well with the amplitude of the antenna Brownian motion.

Chapter 8

Conclusions and Discussions

I have developed the disk-type resonant mass detector equipped with the laser transducer, which consists of the FP cavity with the short cavity length of 10 mm and the super-inver FP cavity with 300 mm length to achieve the frequency stabilization. The laser transducer including the frequency stabilization system has operated continuouly. The measurement of the displacement noise of the laser transducer showed noise sources that limit the sensitivity of the detector, and made clear remaining problems.

In this chapter, I summarize the results and discuss the problems.

8.1 Experimental Results

The perfomance of the resonant mass detector is:

- The displacement noise of the laser transducer is 2×10^{-17} m/$\sqrt{\text{Hz}}$ at the resonant frequency of the antenna under the condition of the well-stabilized frequency less than 0.1 Hz/$\sqrt{\text{Hz}}$.
- It is possible to operate the system continuously. The frequency stabilization works very stably for a long term. The gain of the FP cavity of the laser transducer, however, changes gradually.
- The noise sources of the laser transducer are identified except for an undefined one in the frequency range from 100 Hz to 4 kHz. The vibrational motion of the system consisting of the glue and the end mirror block causes a broadband peak, whose quality factor is about 700. The shot noise and the noise of the detector remain insufficient level.

The resonant mass detector of ICRR can detect a gravitational wave only when its strain amplitude $h > 1.3 \times 10^{-17}$. This sensitivity is worse than those of the cryogenic detectors.

There is little chance that our detector catch gravitational waves, even if the events occurr in our Galaxy. Many efforts should be done to improve the sensitivity.

8.2 Present Problems and Possible Improvements

In this section, let us discuss problems of the transducer and consider their solutions.

Unidentified Noise from 100 Hz to 4 kHz

The one of the largest problems we must solve is to identify the noise source in the frequency range from 100 Hz to 4 kHz. Unless this noise is reduced, a door to the higher sensitivity does not open. What is the noise source? Since electric noises in the servo loop are identified, vibrational motions of mechanical components and optical elements, especially, the actuator, and the vibration of the output edge of the optical fiber are proposed. In these case the noise source might be seismic noise. The slow swinging of the antenna, which caused by the seismic noise and isolation stacks might excite higher frequency vibrational motions of these components.

Another noise source is an unknown electro-magnetic noise. A signal and feedback cables are long near 10 m, they may pick up such a noise.

It will be difficult to reduce this noise, when realized, the sensitivity will achieve at the level of the sum of the shot noise and the noise of the detector.

Isolation Stacks

The isolation ratio of the isolation stacks seems good. From the noise figure in the frequency region from 10 Hz to 100 Hz the isolation ratio is expected to be sufficient at the antenna resonance frequency.

The problem of isolation stacks is to cause the inclination of the antenna disk. They are affected by the change of the ambient temperature. The different expansion and contraction between 3 stacks causes an inclination of the antenna itself. This disturbs the alignment of the laser beam, and the gain of the FP cavity. Since such gain is connected to the sensitivity, the alignment of the laser beam should be controlled to cancel the change of temperature should be controlled so as to be constant always.

In order to solve this problem and keep the sensitivity of the laser transducer constant, at least one alignment per day is needed. A computer can do auto-control for this alignment. Several time controls per day is then possible, so that we can keep the best alignment, *i.e.*, the laser transducer maintains the best sensitivity.

Vibrational Motion of the End Mirror Block

The next problem is the vibrational motion of the end mirror block. The resonant frequency is several kHz and the quality factor is 700, its amplitude at the antenna resonance frequency is probably large. The source of this vibration is unclear. Thermal noise of the this block system or the seismic noise through the isolation stacks? We have little information to analyze quantitatively this noise, and in order to discuss the noise source the sensitivty must be improved so far as observing the slope of this resonance.

In either case, it is conceivable that a proper glue could reduce the amplitude at the antenna resonance frequency. Since available glues do not differ very much in the property of dissipation, we cannot expect dramatic improvement.

One way to avoid the vibrational motion of the end mirror block is to weld the end mirror block with the antenna. The quality factor of the resonance will increase very large and the amplitude of the vibration at the antenna resonance frequency will decrease. In this method, however, a install of the end mirror will be considerably difficult. The other way is to glue the end mirror directly at the side surface of the antenna. In this case the end mirror block is the antenna itself, and the problem of the vibrational motion of the end mirror block will vanish, while a drastic modification of the optical elements and mechanical components will be needed.

Shot Noise and Noise of the detector

The present shot noise and the noise of the detector are bad. The shot noise level is 6.5×10^{-18} m/$\sqrt{\text{Hz}}$, and the noise of the detector more than 1×10^{-17} m/$\sqrt{\text{Hz}}$. The shot noise can be be improved by increasing the incident laser power and making the better mode matching of the laser, and the noise of the detector by the mode matching, too, and making the photodetector with lower noise.

The mode matching could not be improved. Since the incident beam has the fine Gaussian distribution and the positions of the optical elemnts are suitable, the aberration of the matching lens or the contamination of the mirrors which decreases the reflectivity of the mirrors by power loss of the beam and disturbs the TEM_{00}. It is better to use new mirrors.

In order to decrease the shot noise it is the best way to inject a high power beam into the FP cavity. To utilize a high power laser and the improvement of the mode matching will achieve a drastic improvement of both noises.

8.3 Conclusions

The resonant mass detector equipped with the laser transducer has been developed and the long term operation at room temperature has been made possible. As a result, the sensitivity 2×10^{-17} m/$\sqrt{\text{Hz}}$ was achieved. We found a much of the problems that should be solved in the futre. This sensitivity is not enough to catch burst events in the center of our Galaxy. However, this resonant mass detector with the laser transdcuer can work for monitoring lucky events which may occur nearby our solar system under continuos operation with moderate maintenance cost of money and manpower, it does not stand alone for this object, though. I hope that people succeed this work and improve its sensitivity step by step.

Appendix A

Circuits for the system control

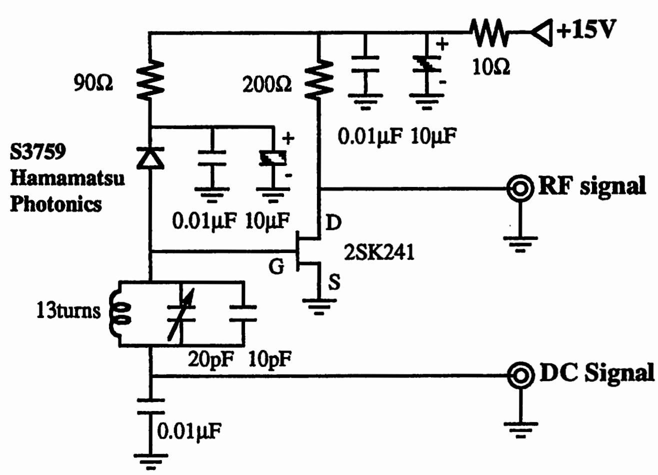

Figure A.1: Photodetector for the laser transducer

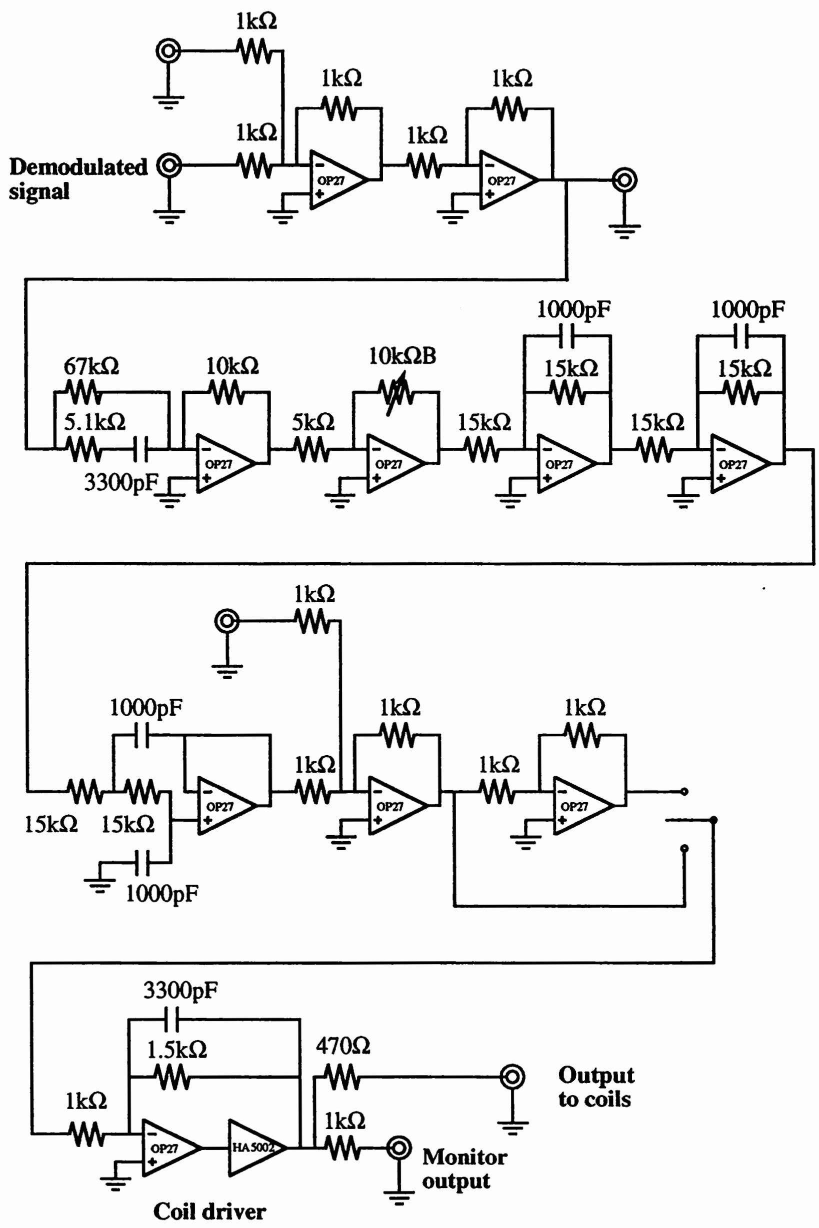

Figure A.2: Feedback servo for the laser transducer

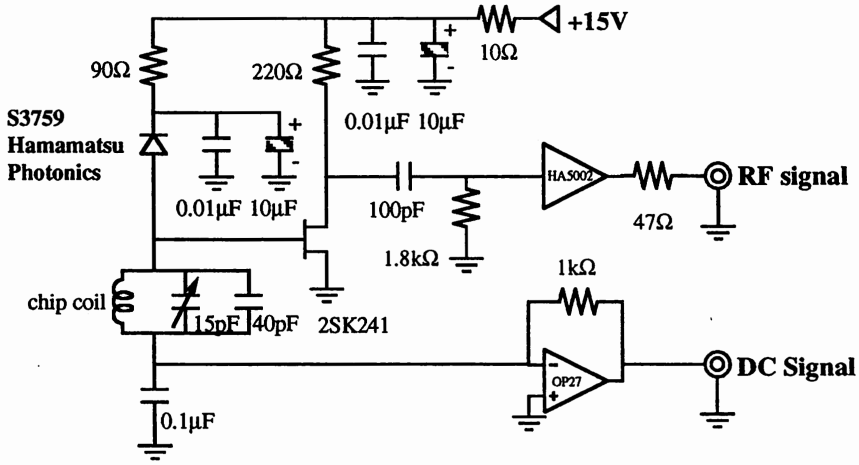

Figure A.3: Photodetector for the frequency stabilization

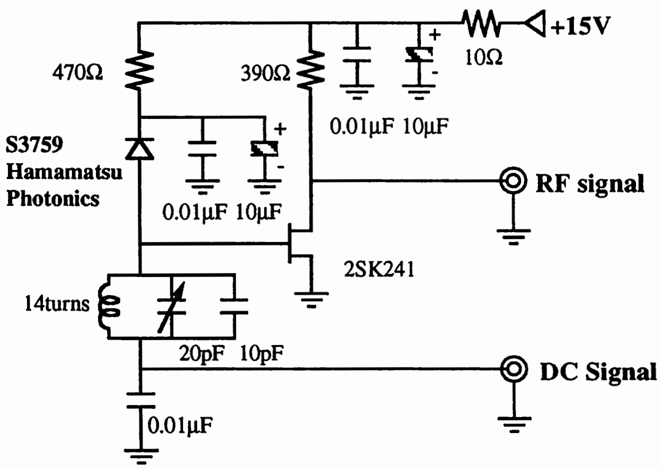

Figure A.4: Photodetector for the frequency stabilization in the antenna tank

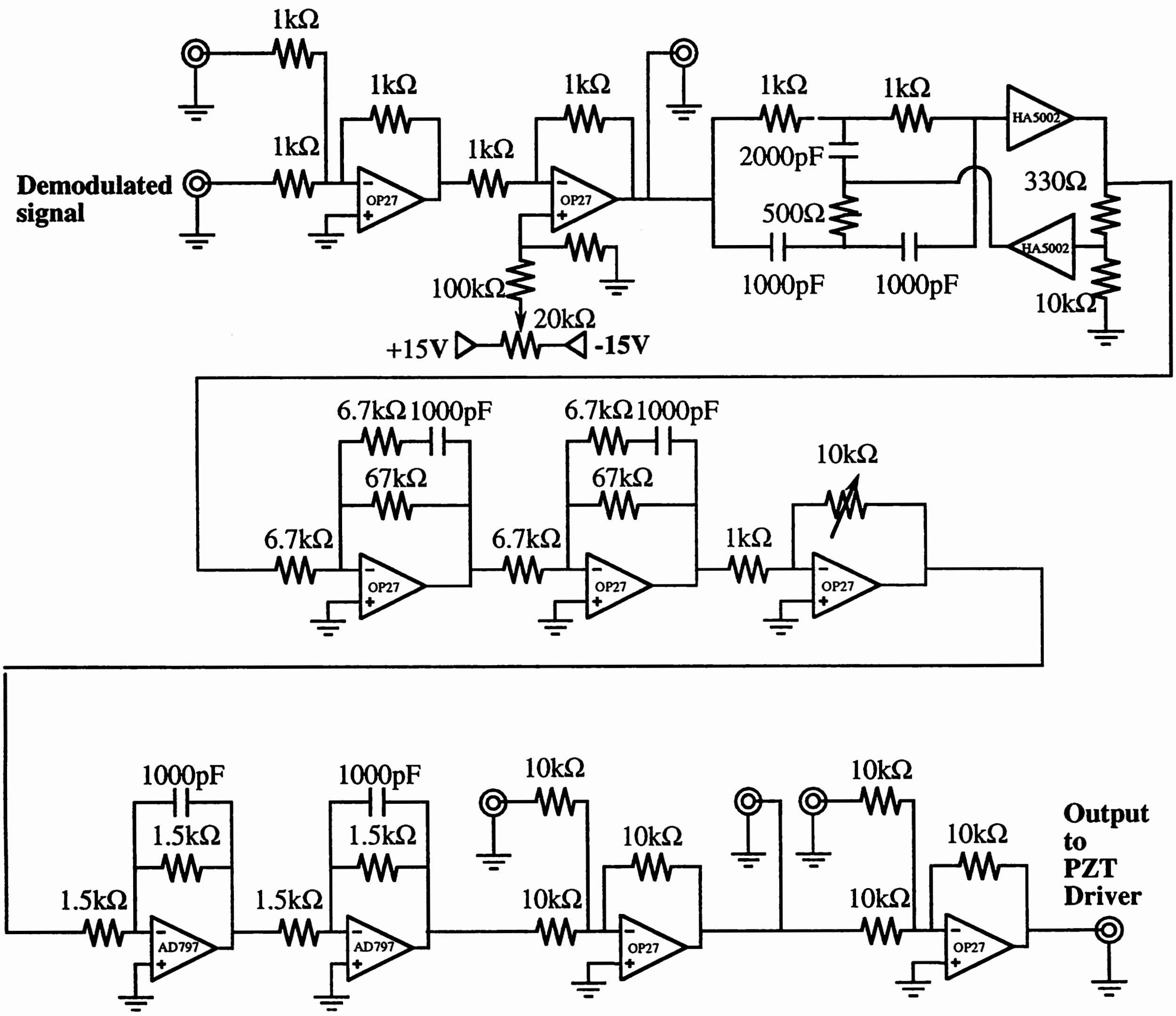

Figure A.5: Feedback servo for the frequency stabilization

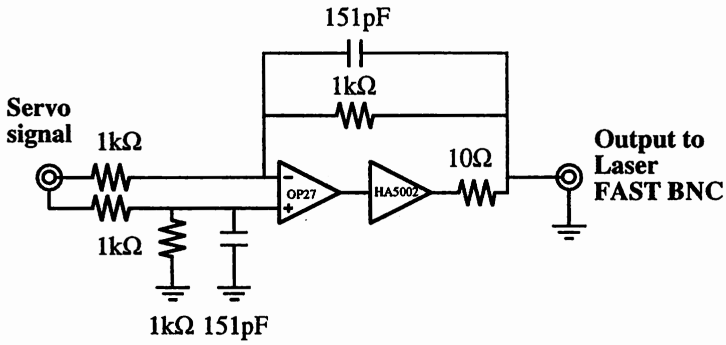

Figure A.6: FAST frequency control driver of the laser

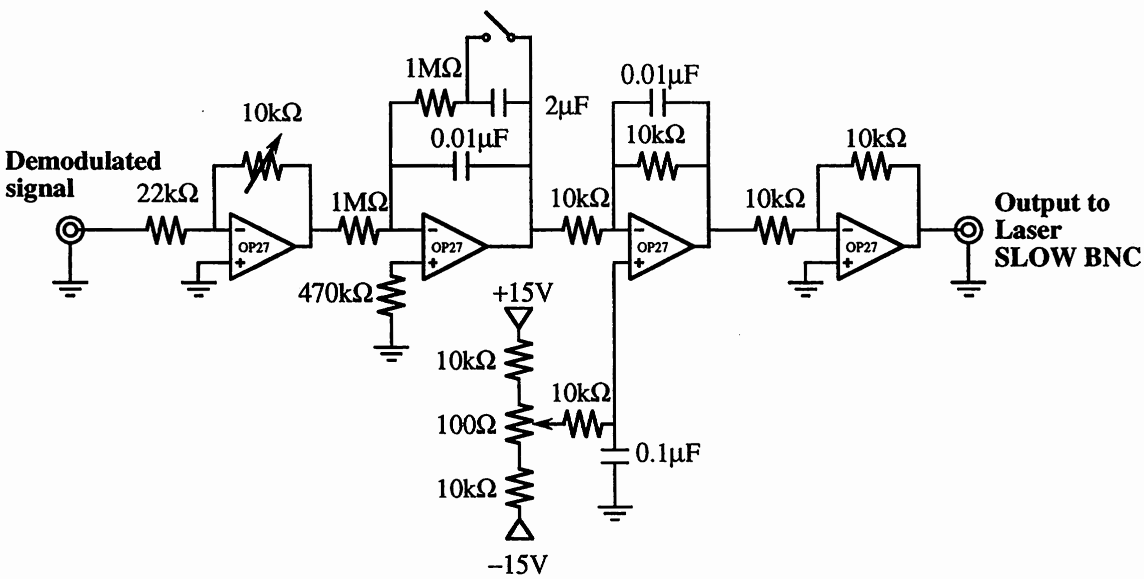

Figure A.7: SLOW frequency control servo of the laser

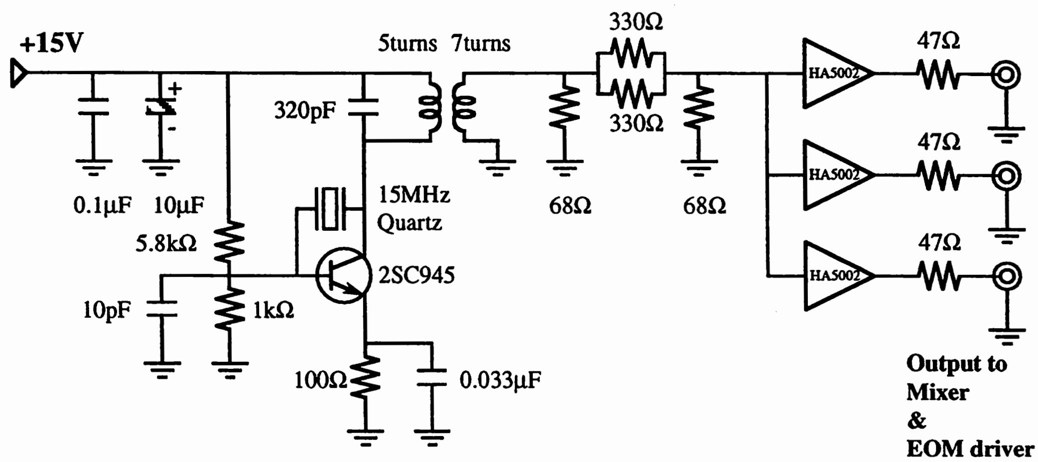

Figure A.8: 15 MHz oscillator

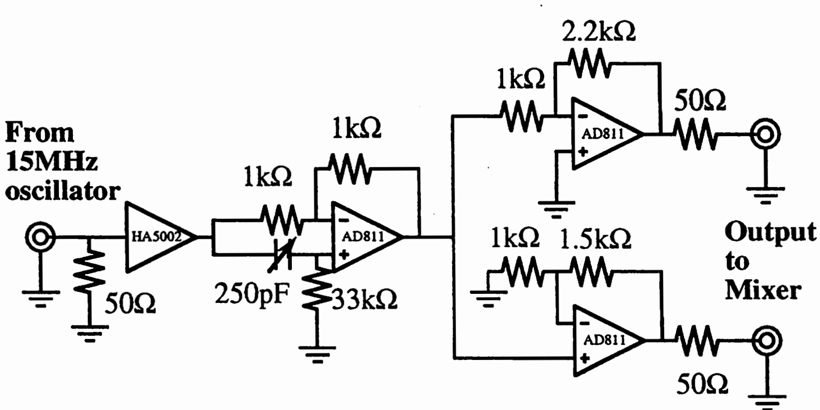

Figure A.9: Phase shifter

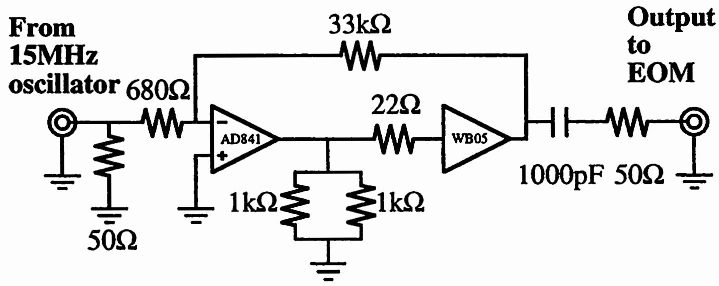

Figure A.10: EOM driver

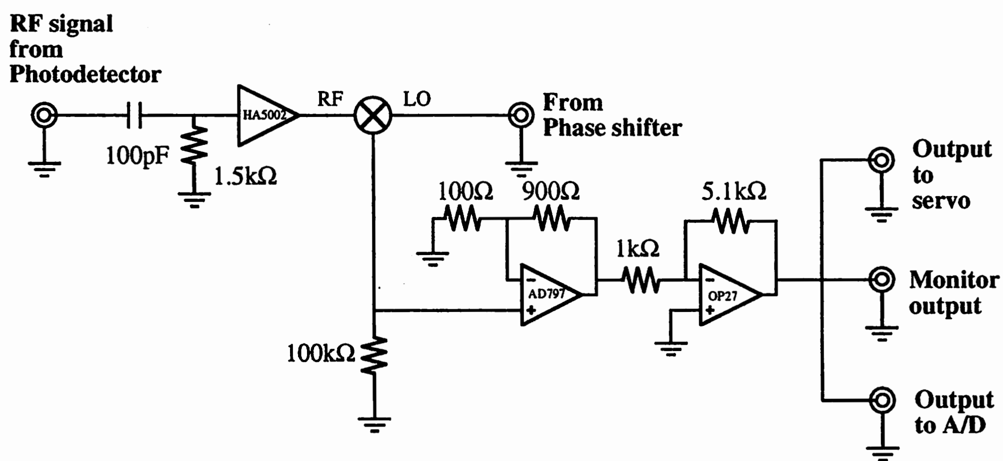

Figure A.11: 15 MHz demodulator

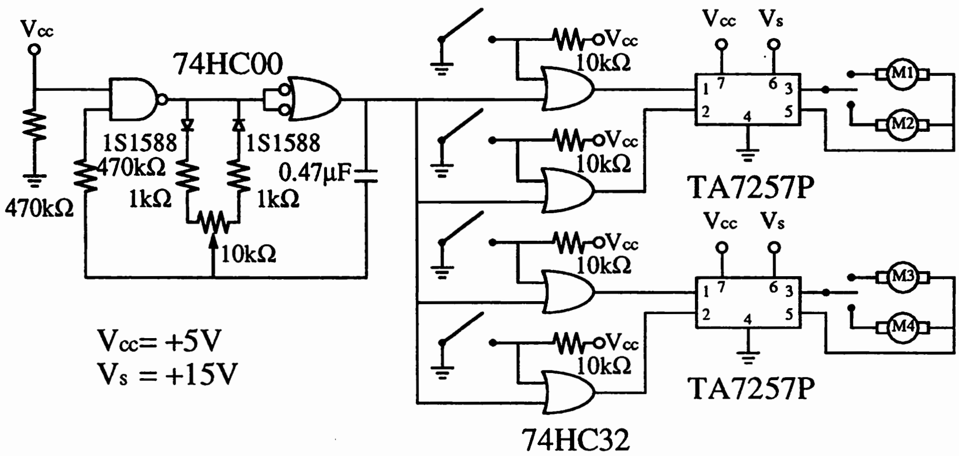

Figure A.12: Motor driver

Bibliography

[1] C.W. Misner, K.S. Thorne, and J.A. Wheeler, *Gravitation* (Freeman and Co., San Francisco, 1973).

[2] P.R. Saulson, *Fundamentals of Interferometric Gravitational Wave Detectors* (World Scientific, Singapore, 1994).

[3] B.F. Schutz, *A First Course in General Relativity* (Cambridge University Press, Cambridge, 1985).

[4] K.S. Thorne, *Gravitational Radiation*, in: S.W. Hawking and W. Israel, eds., *300 Years of Gravitation* (Cambridge University Press, Cambridge, 1987).

[5] H. Hirakawa, *Theory of Relativity*, 2nd edition (Kyoritsu Press, 1986).

[6] J.H. Taylor and J.M. Weisberg, Astrophys. J. Lett. **253** (1982) 908; *id.* **345** (1989)434.

[7] R.A. Hulse and J.H. Taylor, Astrophys. J. Lett. **195** (1975) L51.

[8] A. Abramovici *et al.*, Science **256** (1992) 325.

[9] *VIRGO Final Design 1, 2.*

[10] *Proposal for a 600 m Laser-interferometric Gravitational Wave Antenna*, Max-Planck-Institut für Quantenoptik, 1994.

[11] *TAMA Project Design Report* (TAMA integration group, 1996).

[12] J. Weber, Phys. Rev. **117** (1960) 306.

[13] P. Astone it et al., Phys. Rev. D **47** (1993) 362; F. Ricci, in *Gravitational Wave Experiments*, edited by E. Coccia, G. Pizzella and F. Ronga (World Scientific, Singapore, 1994), p.128.

[14] P. Astone *et al.*, Europhys. Lett. **16** (1991) 231; P. Astone *et al.*, in *Gravitational Wave Experiments*, p.161.

[15] M. Cerdonio *et al.*, in *Gravitational Wave Experiments*, p.176.

[16] Z.K. Geng *et al.*, in *Gravitational Wave Experiments*, p.128; E. Mauceli *et al.*, Phys. Rev. D **54** (1996) 1264.

[17] P.F. Michelson *et al.*, in *Gravitational Astoronomy: Instrument Design and Astrophysical Prospects*, edited by D.E. McCelland and H.A. Bachor (World Scientific, Singapore, 1991), p.14; P.F. Michelson *et al.*, in *Gravitational Wave Experiments*, p.195.

[18] D.G. Blair *et al.*, in *Gravitational Wave Experiments*, p.144; D.G. Blair *et al*, Phys. Rev. Lett. **74** (1995) 1908; I.S. Heng *et al*, Phys. Lett. A **218** (1996) 190.

[19] N. Solomonson *et al.*, Phys. Rev. D**46** (1992) 2299.

[20] J.P. Richard, J. Appl. Phys. **64** (1988) 2202.

[21] J.P. Richard and J.J. Hamilton, Appl. Opt. **30** (1991) 3560.

[22] J.P. Richard, Phys. Rev. D **46** (1992) 2309.

[23] Y. Pang and J.P. Richard, Appl. Opt. **34** (1995) 4982.

[24] R. Monchmeyer *et al.*, Astron. Astrophys. **246** (1991) 417.

[25] P.C. Peters and J. Mathews, Phys. Rev. **131** (1963) 435.

[26] R.V. Wagoner and C.M. Will, Astrophys. J. **210** (1976) 764.

[27] J.P.A. Clarke and D.M. Eardley, Astrophys. J. **215** (1977) 311.

[28] R. Narayan *et al.*, Astrophys. J. **379** (1991) L17.

[29] E.S. Phinney, Astrophys. J. **380** (1991) L17.

[30] *LISA Pre-Phase A Report* Max-Planck-Institut für Quantenoptik, 1996.

[31] F.A.E. Pirani, Acta Physica Polonica **15** (1956) 389.

[32] M.E. Gertsenshtein and V.I. Pustovoit, JETP **16** (1963) 433.

[33] R. Weiss, Quarterly Progress Report of the Research Laboratory of Electronics of MIT **105** (1972) 54.

[34] G.E. Moss, L.R. Miller, and R.L. Forward, Appl. Opt. **10** (1971) 2495.

[35] D. Shoemaker *et al.*, Phys. Rev. D **38** (1988) 423.

[36] K.Kawabe *et al.*, Appl. Phys. B **62** (1996) 135.

[37] *GRAIL: A Gravitational Radiation Antenna in The Netherlands* (G. Frossati *et al.* (1995)).

[38] W.W. Johnson and S.M. Merkowitz, Phys. Rev. Lett. **70** (1993) 2367.

[39] S.M. Merkowitz and W.W. Johnson, Phys. Rev. D **51** (1995) 2546.

[40] H. Hirakawa, *et al.*, J. Phys. Soc. Jpn. **41** (1976) 1093

[41] A.E.H. Love, *A Treatise on the Mathematical Theory of Elasticity*, 4th edition (Dover Publications, New York).

[42] G.E. Moss *et al.*, Appl. Opt. **10** (1971) 2495.

[43] M. Weksler *et al.*, Appl. Opt. **19** (1980) 2717.

[44] P.F. Michelson and R.C. Taber, J. Appl. Phys. **52** (1981) 4313.

[45] H.J. Paik, J. Appl. Phys. **47** (1976) 1168.

[46] H.B. Callen and R.F. Greene, Phys. Rev. **36** (1952) 702.

[47] P.R. Saulson, Phys. Rev. D **42** (1990) 2437.

[48] H. Hirakawa *et al.*, Jpn. J. Appl. Phys. **18** (1979) 177.

[49] V.B. Braginsky *et al.*, Science **209** (1980) 547.

[50] V.B. Braginsky, Sov. Phys. Usp. **31** (1988) 836.

[51] T. Suzuki *et al.*, Phys. Lett. A **67** (1978) 2.

[52] R.Del Fabbro *et. al.*, Rev. Sci. Instrum. **59** (1988) 292.

[53] *Gravitational Wave Antenna Technical Report*, edited by N. Mio and M. Ohashi, 1992, see Section 5.6.

[54] K. Kuroda and K. Shimizu, Rev. Sci. Instrum. **64** (1994) 1017.

[55] A. Mizutani, Ph.D thesis (1991).

[56] H.Hirakawa and K. Narihara, Phys. Rev. Lett. **35** (1975) 330.

[57] A. Yariv, *Introduction to Optical Electronics*, 3rd edition (Holt, Rinehart, and Winston, Inc., 1985).

[58] R.Drever *et al.*, Appl. Phys. B **31** (1983) 97.

[59] H. Kogelnik and T. Li, Proc. IEEE **54** (1960) 1312.

[60] D.Z. Anderson, Appl. Opt. **23** (1984) 2944.

[61] J.K. Blackburn, *The Laser Interferometer Gravitational Wave Observatory Project LIGO*, submitted to the Proc. of the Banach semester on *Mathematical Aspects of Gravitational Waves*, March 1996, Warsaw, Poland.

[62] Technical Staff of Newport Co., *Way to Use Optical Fiber and* , (The Optronics Co., Ltd., 1988).

[63] K. Okamoto, *Theory of Optical Waveguides*, (Corona Publishing Co., Ltd., 1992).

[64] K. Kawano, *Fundamentals and Application of Optical Combination system*, (Gendaikougaku-sya, 1991).

[65] K. Tsubono *et al.*, Rev Sci. Instrum., **64** (1993) 2237.

[66] P.J. Veitch, Rev. Sci. Instrum. **62** (1991) 140.

[67] A. Gillespie and F. Raab, Phys. Lett. A **178** (1993) 357.

[68] K. Tsubono *et al.*, Jpn. J. Appl. Phys. **30** (1991) 1326.

Acknowledgments

I would like to appreciate Prof. K. Tsubono, Prof. K. Kuroda, and Prof. Mio for advising throughout this experimnet. I wish to express my thanks to Tsubono group members, Mr. Kawabe, Mr. Ando, Mr. Totikubo, Mr. Arai, Ms. Ohishi, Mr. Yamamoto, Mr. Sasaki, Mr. Takamori, and Mr. Naito and ICRR group members, Dr. Kanda, Dr. Barton, Mr. Matsumura, Mr. Uchiyama, Mr. Kuwahara, Mr. Tomaru, and Mr. Miyakawa for their support on my experiment. I also thank Dr. M.A. Barton for checking the manuscript.